HALL EFFECTS IN TOPOLOGICAL INSULATORS

LE QUY DUONG
(B.Eng, South Russian State Technical University)

A THESIS SUBMITTED

FOR THE DEGREE OF DOCTOR OF PHILOSOPHY
DEPARTMENT OF PHYSICS
NATIONAL UNIVERSITY OF SINGAPORE

2016

This page was intentionally left blank.

Declaration

I hereby declare that this thesis is my original work and it has been written by me in its entirety. I have duly acknowledged all the sources of information which have been used in the thesis.

This thesis has also not been submitted for any degree in any university previously.

Le Quy Duong

27th October 2016

This page was intentionally left blank.

Acknowledgements

"Most important part of doing physics is the knowledge of approximation."

Lev Landau

My dream of using theory and computation to conduct experimental–driven research would not be realized without help and encouragement of many people. First and foremost, I would like to convey special regards to my supervisors: **Prof. Hsin Lin** and **Prof. Feng Yuan Ping**. I would like to thank Prof. Feng for admitting me to National University of Singapore and giving fundamental knowledge. Great gratitudes go to Prof. Hsin Lin who guides me throughout the years with a day–to–day basis. His motivation, knowledge, hard work and carrying manner motivate me to give energy for physics, spending sleepless night building the codes and understanding the theoretical basis. It is my honour to work with Prof. Hsin Lin – a physicist with a significant knowledge from both theoretical and experimental points of view. He has educated me as a responsible researcher and introduced me to great people in the field. I believe that their guidance, enthusiasm, and pedagogical skills will help me till the rest of my career.

Dr. Tanmoy Das has been always an available person for discussion. I would like to convey my special regard and gratefulness to him for his encouragement, and cheerful time working together. I would not be able to work hard without him as a great teacher and motivator. I also want to thank my friend Kapildev Dolui for useful critical discussions. My special regards go to Prof. Jens Martin for giving nice questions regarding experimental point of view in my project.

I would like to thank Dr. Shinming-Huang, Dr. Wei Feng Tsai for being sup-

portive, ideas, accuracy. I believe they will be great professors in the future. I want to especially thank to Baokai, Guoqing Chang, Chuang Han, Dr. Chi Cheng Lee, Dr. Bahadur Singh, Xiaoting Zhou for sharing knowledge, codes and data which are crucial for my thesis completion. A special group is not mentioned yet, my regards go to Dr. Minggang Zeng, Dr. Shen Lei for their helps in early time of my PhD. Many thanks to Fabio and ShuangLong for teaching me so much throughout the years.

This thesis is results of collective work, presenting the lesson learned by people who developed the theoretical/computational tools based on experimental data. Throughout the thesis work, I have learned that there are people who develop the tools and there are those who use them and I would like to apology those who I missed to acknowledge.

I also thank two organizations: Singapore International Graduate Award (SINGA) for financial support, Centre for Advanced 2D Materials (CA2DM) for providing facilities. Moreover, I would like to especially thank my friends for supports during the years and make my PhD more cheerful: Sandhya, Jun Zhou, Meini Zhang, Linghu Jiajun, Dr. Jeil Jung, Alexandra Carvanho, Dr. Paolo Emilio. I also thank to Prof. Dinh Tien Cuong for nice advice during coffee break.

Russia has been the first place where my love to computational physics arises, my best regards go to Prof. Knyazev Sergey Yurievich for teaching me math. physics and code development in a nutshell which are surprisingly helpful for my PhD works.

I finish with Vietnam, I would like to thank my parents giving me to explore my own potentials. I could have not been I am today without their supports, loves, and encouragement.

Contents

Summary

Topological Insulators (TIs) belong to a new phase of matter where the topological property is protected by Time Reversal Symmetry (TRS). TIs have long been question of great interest since they can provide a novel material platform where the surface states usually play an essential role to generate new topological phases, such as quantum anomalous Hall (QAH) effect after breaking TRS. This thesis reports on the Quantum Anomalous Hall (QAH) and Spin Hall Effect (SHE) of TI thin films and broken symmetry topological phases for different classes of topological materials. Our works fall in four categories: (1) Quantum Anomalous Hall (QAH) effect in TI thin film, (2) QAH effect with tunable Chern number near a Z_2 topological critical point. (3) Unconventional QAH effect of topological crystalline insulators. (4) Intrinsic SHE in TI thin film. In the first part of thesis, we comprehensively investigate the QAH effect in magnetically doped Bi_2Se_3 thin film with different magnetic structures. In the second and third parts of thesis, we propose a mechanism to realize QAH phase without the surface state involved. We take two material classes: Z_2 TI $TlBi(S_{1-\delta}Se_{\delta})_2$ and topological crystalline insulator $Pb_{1-x}Sn_xTe/Pb_{1-x}Sn_xSe$ as examples, where both of them are tunable from trivial to non-trivial phases via chemical composition. Specifically, we demonstrate that the magnetically doped materials near topological critical points are candidates for high Chern number QAH insulators. Our proposal successfully reduces the necessary exchange coupling strength for a targeted Chern number where the QAH phase occurs even in the trivial side of the material. Finally, the intrinsic SHE in Bi_2Se_3 thin film are also discussed.

This page was intentionally left blank.

List of Tables

This page was intentionally left blank.

List of Figures

List of Acronyms

1D One Dimensional

2D Two Dimensional

3D Three Dimensional

TI Topological Insulator

TCI Topological Crystalline Insulator

QHE Quantum Hal Effect

FQHE Fractional Quantum Hall Effect

QSHE Quantum Spin Hall Effect

QSH Quantum Spin Hall

QAHE Quantum Anomalous Hall Effect

QAH Quantum Anomalous Hall

QAHI Quantum Anomalous Hall Insulator

TRIM Time Reversal Invariance Momentum

SHE Spin Hall Effect

SHC Spin Hall Conductivity

TRS Time Reversal Symmetry

ARPES Angle Resolved Photo-emission Spectroscopy

MBE Molecular Beam Epitaxy

2DEG Two Dimensional Electron Gas

QL Quintuple Layer

FM Ferromagnet

FM-TI Ferromagnet–Topological Insulator

FM-TI-FM Ferromagnet–Topological Insulator–Ferromagnet

SOC Spin–Orbit Coupling

TKNN Thouless-Kohmoto-Nightigale-Nijs

VHs Van Hove singularity

TPT Topological Phase Transition

TSS Topological Surface State

QPI Quasi-particle Interference

SBC Spin Berry Curvature

Chapter 1

Introduction

1.1 Topology in a nutshell

Recently, there has been renewed interest in the application of topology in physics. Topology is a concept in mathematics about the continuity in space [1]. An early example is the Möbius strip which can be made by connecting two ends a long rectangle original strip with twists which are not possible to destroy without destroying the object [2]. Figure 1.1.a shows a simplest form of Möbius strip while figure 1.1.b shows how to connect a strip with two edges so that the arrows matched. Another example is the mug and doughnut with equal number of holes in figure 1.1.c-d, respectively. In addition, it is not possible to distinguish these two objects in the language of topology where one can transform to another. In fact, topology introduces many concepts which are applicable for physics and engineering [1] like surface, topological order, etc.. The topology of surface also can be characterized by Euler characteristic:

$$\chi = \frac{1}{2\pi}\int_S KdA = 2 - 2g \tag{1.1}$$

The value of this ingegral is quantized by Gauss-Bonnet theorem [3, 4]. Here, $\int_S KdA$ is the curvature integra, K – Gaussan curvature, A – element of the area, g – the genus of the surface. In addition, a topological order is also extended and

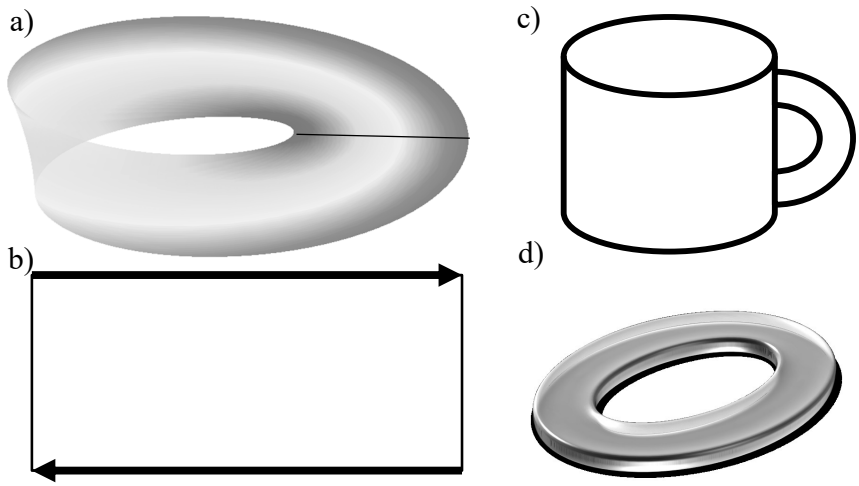

Figure 1.1: Topology in geometry (a) A Möbius strip with one boundary and one surface. (b) By connecting two edges of a rectangle so that the arrows matched, a Möbius strip with fixed topology is made. (c) A coffee mug with one hole, being equal to the number of holes in doughnut presented in (d)

utilized to explain fractional quantum Hall states [5]. Moreover, it was shown that the Z_2 topological order can characterize the well known quantum spin Hall state in Two Dimensional (2D) topological insulator [6, 7]. Thus, defining topological property of materials is of particular interest.

1.2 Review of Hall effects

The traditional Hall effect is fundamental to many application in eletronics like Gaussmeter probe using Hall sensor. The basics physics come from the Lorentz force experienced by electronic charge under longitudinal voltage applied on metallic or semiconductor films. Besides the traditional Hall effect where the electron motions are classical, recent transport theory and experiments have confirmed the existence of Hall effects where the description of quantum mechanics is required, they are, namely, Quantum Hal Effect (QHE) [8], Fractional Quantum Hall Effect (FQHE) [5], Spin Hall Effect (SHE) [9], Quantum Spin Hall Effect (QSHE), and Quantum Anomalous Hall Effect (QAHE). The quantum Hall effect emerges when applying magnetic field in direction perpendicular to Two Dimensional Electron Gas (2DEG) in which the most popular system is thin

film GaAs , graphene [10–12]. Under the magnetic field, electrons move in cyclotron trajectory and jump along the edge. Theoretically, the QHE arises under strong magnetic field, when electron motion can be separated in single-particle motion with Landau level, thus the Hall conductance is quantized. The FQHE is more complex when electron orbital interaction are strong and the physics is still under active scrutiny [5, 13, 14]. The intrinsic spin Hall effect, however, carries another story without the magnetic field applied. It is also observed in 2D electronic system when electron spin can flip under weak electric field. Thus, the spin up and down electrons move in two opposite directions, causing a spin Hall voltage [15] in 2D system. Generally, the spin orbit coupling is a essential ingredient for anomalous Hall effect, quantum Hall effect and spin Hall effect. These effects can be detected in transition metals, 2DEG and more recently in Topological Insulator (TI) system. The QAHE carries another fascinating story when internal magnetization combined with spin orbit coupling can drive TI thin film to quantized Hall conductivity without Landau level, instead it is almost dissipationless with the resistance highly attenuated with a large band gap.

1.3 Topological phases – materials and experimental realization

This sub-section provides an overview of recently investiated TI materials and related topological phases. When the concept of topology and Chern number in mathematic is well known [9], its application in physics is developing rapidly with topological band theory [16]. The concept of Chern number in physics is the number of edge states of two dimentional systems. Here, we note that one should differentiate between One Dimensional (1D) edge of a 2D system and 2D surface of a 3D system. In the presence of spin-orbit coupling and certain crystal group symmetry, TI's bandstructure can be signified by a topological invari-

ance. Meanwhile, wave function in the bulk TI in the Hibert space expanding in a nontrivial topology [17]. According to the topological band theory, there should be a non-trivial surface state of the material. The TI surface state is of particular interest for spintronics study and experiments, since it hosts various interesting properties with spin polarized currents in real space. Here, we aim at reviewing the existing topological phases of condensed matter system which are apparently experimentally realized. We start with a QSHE system or 2D topological insulator, followed by of 3D topological insulator with a Dirac surface state. We also introduced a new class of material with topological crystalline surface states.

The two dimensional TI state is also called Quantum Spin Hall (QSH) state which has been observed experimentally in 2D HgTe-CdTe quantum wells [18], InAs/GaSb/AlSb quantum wells [18]. QSH systems are 2D insulating materials in the bulk but conductive on the edge. In the existence of time-reversal symmetry QSH edge states exhibit a 1D Dirac cone at the edge. Generally, the main difference between the QHE and QSHE is that the QHE requires a magnetic field to break the time reversal symmetry and obtains a discrete set of Hall conductivity [19]. On the other hand, the QSHE has time reversal invariance and does not require an external magnetic field. The first QSH effect was proposed in (Hg,Cd)Te quantum well which can be explained theoretically by the 4-band BHZ model based on k·p perturbation theory for bulk material [**bernevig_quantum_2006**]. Experimentally, the 2D structure CdTe/HgTe/CdTe grown by molecular beam epitaxy shows the discrete spin Hall conductance in the absence of applied magnetic field when the thickness of HgTe layer is larger than a critical parameter of 6.5nm [20].

The topological insulator field has been extended in 3D systems where gapless surface states of Bi/Sb alloys and the Dirac cone of Bi_2X_3 (X=Se,Te) multilayer materials were detected. By contrast with graphene, this Dirac cone is spin polarized with strong spin-orbit coupling of Bi and Se atoms [16]. The

physics around the Dirac cone is of interest with tunable properties under external fields. Particularly, the three dimensional magnetic TI characterized by magnetic impurities (Fe,Cr,Mn) [21] on the surface of Bi_2X_3 (X=Se,Te). This may lead to another topological phase–Quantum Anomalous Hall (QAH) phase. In the existence of ferromagnetic ordering, the magnetic field breaks time reversal symmetry and a band gap is opened at the Dirac cone. Thus, the Dirac surface state becomes massive and TI is insulating if the Fermi level lies inside the band gap. The ferromagnetic (FM) ordering and Spin–Orbit Coupling (SOC) are sufficiently strong to transform the topological phase to non-trivial one with a finite Chern number. Besides, several systems have been predicted to be QAH systems namely: $GdBiTe_3$ thin films [22], ferromagnetic CdO/EuO quantum well [23]. In addition, there have been some predictions of large Chern number QAHE in magnetic topological crystalline insulators. For example, Cr-doped $Bi_2(Se,Te)_3$ is a potential candidate for the C=2 Quantum Anomalous Hall Insulator (QAHI) [23, 24]. When theory and experiments were reported to demonstrate the quantum Hall effect [8], anomalous Hall Effect [25] and QSHE [6, 20], the QAHE is more difficult to observe. This is because it is not straightforward to detect ferromagnetic ordering on the surface of magnetically doped TIs and it requires extremely low temperature to reach QAH [6, 20, 26, 27]. The first QAH experiment successfully demonstrates the quantized Hall conductance on the surface of compound Cr-doped $(Bi,Sb)_2Te_3$ with the Chern number 1.

More recently, a new concept of surface state of IV-VI narrow gap semiconductors was proposed based on the extension of topological classification of strongly spin-orbit coupled materials [28]. The Topological Crystalline Insulator (TCI) is a novel material platform where the surface state exists due to a non-trivial bulk band topology and the crystalline mirror symmetry [28, 29]. Apparently, the change in chemical composition of $Pb_xSn_{1-x}Te/Pb_xSn_{1-x}Se$ can drive the bulk band from trivial to a non-trivial state [29, 30]. Additionally, the TCI phase transition appeared across a critical composition Sn may have inter-

esting behaviour due to the gapless bulk state. The material class is exotic with the presence of C_{4v} symmetry, TRS combined with a mirror symmetry. Moreover, the mirror Chern number is a new topological invariance for this material class. The electronic properties of TCI in both trivial and non-trivial sides are investigated in a number of experiments [30]. Interestingly, the material exhibits exotic properties with the presence of unconventional quasi-particle interference signal, or the theoretical prediction of the quantum spin Hall effect in TCI [31]. While the surface magnetism has been confirmed in Z_2 magnetically doped TI, the surface magnetism in TCI has not been found. Recently, a prediction of high Chern number QAHE in TCI in thin film limit [32]. It is expected to drive the TCI to new topological phases by various symmetry breaking perturbations (time reversal symmetry breaking, crystal symmetry breaking, inversion breaking). However, there is still a room for the research for magnetic IV-VI narrow gap semiconductors. By doping, the material could host magnetism with certain direction with respect to the 2D crystal thin film. Recently, theoretical investigations have been carried out to predict the high Chern number QAHE in magnetic thin film TCI.

This thesis is organized as follow: In chapter 2 we investigate the Z_2 topological insulator through a layered k·p model, imposing magnetizations with three different configurations. In chapter 3 we present the physics of multiple quantum anomalous Hall phase transition near Z_2 topological critical point when the band inversion is generated without surface state. In chapter 4, through a realistic tight-binding model of thin film of narrow gap semiconductor $Pb_{1-x}Sn_xSe$ or $Pb_{1-x}Sn_xTe$, we found an unconventional touching point when the magnetization can drive low energy spectra of the materials to a new Van Hove singularity (VHs). Finally, inspired by experimental works of the intrinsic SHE in TIs, we predict a layer-dependent spin Hall conductivity of TI.

Chapter 2

Quantum anomalous Hall effect in Topological Insulators

Bi based structures play a critical role in the field of Z_2 Topological Insulator (TI) and novel topological phases. Starting with Bi_xSb_{1-x} [33], followed by bismuth chalcogenides [16, 34], these materials are one of the most widely used groups for Hall transport measurements. While the bulk electronic structure of rhombohedral 3D TI Bi_2Se_3 carries unconventional properties with a direct band gap at the Γ point. The band inversion in which the swapping of orbital character of p orbitals at Γ point happens and a bulk band gap opens by spin orbit coupling. When cutting the Bi_2Se_3 crystal along [111] direction, a surface state arises connecting bulk valence and conduction bands. For systems with spin orbit coupling, TRS and inversion symmetry are survived, the degeneracy in band-structure guarantees a zero net anomalous Hall current. The surface states exhibit a single Dirac cone on each surface with opposite spin chiralities due to the inversion symmetry.

While the surface states of TIs are robust against weak external perturbations [35], a magnetic field perpendicular to the surface of TIs breaks TRS and open up a magnetic gap through a Zeeman field. Under a magnetic perturbation the spin-up and spin-down states split and a hedgehog-like spintexture is

captured both in first-principles calculation and ARPES [36]. Theoretical model suggests that the magnetization can be generated by doping with ferromagnetic elements (proximity induced ferromagnetism). For example, theory predicted that when doping Bi_2Se_3 with ferromagnetic elements like Fe,Cr the ferromagnetic ordering is more favourable compared to antiferromagnetic one. Thus, the calculated energy of the ferromagnetic state is lower (or more stable) than that of the antiferromagnetic state [37, 38].

In a quantum Hall state [8], the edge electrons can "jump" around the boundary of 2D slab - vacuum, the Hall conductivity shows plateaus at exact values of magnetic field. After that, the quantum spin Hall state [20] (2D TIs) was discovered in quantum well structure CdTe–HgTe–CdTe with the notion of "spin current". In the edge of QSH the spin currents are spatially separated: the spin up and spin down electrons move in opposite directions. The total Chern number of the system is zero but the system can be signified by a topological invariance, the spin Chern number [39] of 2D TIs is zero but their substraction is nonzero. Thus, the Hall conductivity of the system is quantized in unit of $\frac{e^2}{h}$. The quantum anomalous Hall state [26], however exhibits non-trivial state without Landau levels. The nonzero Hall conductance can be observed even in zero magnetic field. However, less study was conducted to investigate the critical exchange field driven by magnetic dopant to obtain nonzero Hall conductivity. In addition, one challenge of experiments is generating supra-high exchange field to either get a large magnetic gap or higher Chern number. In the absence of exchange field we have edge state but due to the finite size effect when the thickness of the film is reduced to be comparable with decay length of surface states, the energy gap opened as a result of quantum tunnelling between top and bottom surfaces states to avoid the crossing of bands with same quantum numbers. Hence, the system has a small gap at the Dirac point and ultra-thin TI film is adiabatically connected to trivial insulating phase.

In magnetic TIs [26], the non zero Hall conductivity is due to Berry curva-

ture originating from out of plane ferromagnetism, and spin orbit coupling. By increasing the magnetic doping in a TI thin films, in case the gap closes and reopens, the initial state and final state cannot be adiabatically connected. Consequently, they belong to different topological phases and undergo a topological quantum phase transition [27]. However, little study has been conducted to understand the relation of bandstructure topology, thickness, spintexture and Hall conductivity for ultra-thin magnetic TI films. Hence, we consider three possible magnetic configurations (one substrate-induced ferromagnetic ordering, two substrate induced ferromagnetic ordering, bulk doping). It turns out that TIs doped with ferromagnetic elements in the bulk requires the less exchange energy to get non-zero quantized Hall conductivity. In the two last configurations we indicated another critical exchange energy that can get more than two topological phases (multiple topological phase transition).

The conventional model of 3D TIs is simplified to describe only the surface states without the quantum well states or too complicated to be implemented as an insightful model for QAHE for TIs [40]. We adapted a realistic k·p model of three dimensional TI based on one quintuple layer Bi_2Se_3 Hamiltonian through layer by layer approaches in which a grown bilayer of Rashba-type spin-orbit coupled 2DEG is placed on adjacent planes of bilayers. The model can be used to explore topological bandstructure for Bi_2Se_3 slab with arbitrary thickness. The critical spontaneous exchange field to break TRS and open a band gap is calculated and explained by considering ultra-thin magnetic films model. Except for studying electronics properties of Bi_2Se_3, the model is also flexible to study a wide range of 3D TIs materials like Bi_2Te_3. The Chern number characterising the bandstructure topology is computed based on Kubo formalism [41]. Moreover, the effect of non-zero temperature on the Hall conductivity is also considered. In addition, we applied electric field to the slab model with the assumption that the potential in each quintuple layer of Bi_2Se_3 varies linearly, making the energy separation between the top and bottom surface Dirac cones.

This chapter presents the work published in [42]

2.1 Formalism for k.p model

Crystalline Bi_2Se_3 is layers of Se–Bi–Se–Bi–Se atoms in one Quintuple Layer (QL), spatially separated with other QLs by Van Der Waals gap. Figure 2.1.a shows an unicell of 6QLs Bi_2Se_3 slab with the Se atoms (yellow circles) and Bi atoms (brown circles). From theoretical point of view, each "perfect" QL has the same energy and structure, coupled with its neighbours, except for surface QLs which are exposed to the vacuum, as presented in Figure 2.1.b. In real experiment, the material is grown on substrate and under measurement there is a potential difference between top and bottom surfaces. This breaks inversion symmetry of the system when an effective electric field can introduce a potential gradient along crystal grow c-axis (see Figure 2.1.c, where the arrow is the direction of the applied field). We implemented a model being presented by k_x

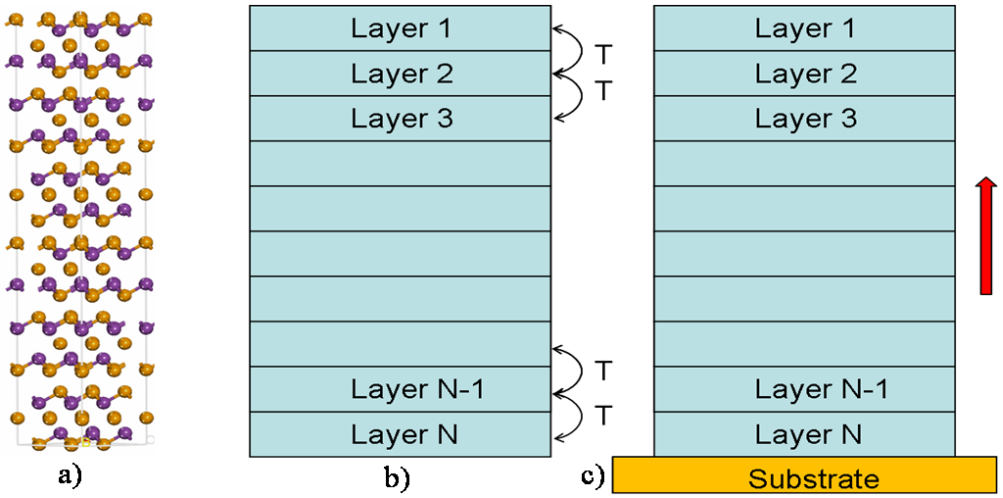

Figure 2.1: Crystalline structure of Bi_2Se_3 and simplified model (a) Material structure of Bi_2Se_3 for a 6QLs slab under hexagonal presentation. The yellow circle–Se atoms, brown circle–Bi atoms (b) The interactive model for three dimensional topological insulators. (c) Realistic material grown on substrate with potential gradient.

and k_y coupled with Pauli spin matrices σ_x and σ_y respectively. This basically

reproduces a spin orbit coupling with kinetic energy.

$$H_{sp} = \begin{pmatrix} k^2/m & vk_x + ivk_y \\ vk_x - ivk_y & k^2/m \end{pmatrix} \tag{2.1}$$

The diagonal element $\frac{k^2}{m}$ is the kinetic term with m being orbital mass, the Hamiltonian acts in spin space. The surface states Hamiltonian H_{sp} is originated from Rashba spin-orbit coupling:The surface state of Bi_2Se_3 around the Γ point is mainly contributed by Se p_z orbitals. Neglecting the contribution of three other atoms within one QL, we consider only p_z orbitals of two Se atoms with the basis

$$|1, p_z, \uparrow\rangle; |2, p_z, \uparrow\rangle; |1, p_z, \downarrow\rangle; |2, p_z, \downarrow\rangle,$$

where the index 1,2 are atomic orders, $\uparrow$ and $\downarrow$ are spin up and spin down. We hence adapt a model Hamiltonian with real space hoping parameters for the [111] surface of Bi_2Se_3. The system is symmetric around the Γ point with TRS. The effective Hamiltonian H_p of one quintuple layer captures both spin degeneracy and tunnelling term:

$$H_p = \begin{pmatrix} k^2/m_1 & d + k^2/m_2 & vk_x + ivk_y & 0 \\ d + k^2/m_2 & k^2/m_1 & 0 & -vk_x - ivk_y \\ vk_x - ivk_y & 0 & k^2/m_1 & d + k^2/m_2 \\ 0 & -vk_x + ivk_y & d + k^2/m_2 & k^2/m_1 \end{pmatrix} \tag{2.2}$$

where m_1 is mass term. d and m_2 specify the hopping energy between two orbitals with the same spin (d, m_2<0). For stacked structure of Bi_2Se_3, the system can be expressed as each quintuple layer having two nearest neighbours (except

for two surface quintuple layers having only one neighbour).

$$T = \begin{pmatrix} t & 0 & 0 & 0 \\ t_z & t & 0 & 0 \\ 0 & 0 & t & 0 \\ 0 & 0 & t_z & t \end{pmatrix} \tag{2.3}$$

Semi-infinite model of [111] surface 3D TIs is written as:

$$H = \begin{pmatrix} H_1 & T_1 & \cdots & \cdots & 0 \\ T_1^\dagger & H_2 & T_2 & \cdots & 0 \\ 0 & T_2^\dagger & H_3 & \cdots & 0 \\ \vdots & \vdots & \vdots & \ddots & \vdots \\ 0 & \vdots & \vdots & \vdots & \vdots \end{pmatrix} \tag{2.4}$$

where $H_i = H_p$ and $T_i = T$ for any integer i which denotes the index of quintuple layers, T is hoping matrix between two neighbouring QLs (4x4 matrix). The electronic structures capture salient features of the Z_2 TI and gives the topological phase transitions and surface gap opening with finite film thickness due to the finite size effect. A realistic parameter set is obtained by fitting the band structure to the experimental dispersion [43].

We have $m = 0.125\text{eV}^{-1}\text{Å}^{-2}$; m_2=-0.04eV^{-1}Å^{-2}; d=0.22eV, $v = 2.5\text{eVÅ}$; $t_z = 0.37\text{eV}$; and $t = -0.045\text{eV}$.

Values of these parameters yield a semiconducting bulk gap 300 meV and the single-Dirac-cone topological surface states on each side of the surface. The expected in-plane spin-polarization of the surface state are obtained. In addition, we find that the surface gap decreases dramatically with increasing film thickness, and above 6QLs, practically a "tiny-gap" remains which all agree with experimental data [43].

The theory of Hall effect in spin-orbit coupling material has long history. The calculation was firstly initialized by Karplus and Luttinger to solve conduc-

tivity problem based on perturbation theory (We give a brief derivation in Appendix A). Later, Kubo proposed a model based on transport coefficient, summarizing the proof by Luttinger when a system in equilibrium and slowly tuned by in-plane electric field (see Appendix B). The theory can be also extended by Green's function approach, computing conductivity under interaction and impurities (see Appendix C). We adapt Kubo formula to compute the Chern number:

$$C = \frac{1}{2\pi} \sum_{m,n,k} \frac{Im[\langle nk|\frac{\partial H}{\partial k_x}|mk\rangle\langle mk|\frac{\partial H}{\partial k_y}|nk\rangle]}{(E_{nk} - E_{mk})^2}(n_f(E_{nk}) - n_f(E_{mk})) \tag{2.5}$$

$n_f(E)$ is the Fermi-Dirac distribution function. In equation 2.5 The topological phases are mainly defined by the contribution of the Dirac bands. The procedure of Chern number is as follow: Firstly, for each k-point, one should do exact diagonalization to get the eigenvalues and wavefunction. Secondly, the Berry curvature at each k-point is computed using the velocity operators and wavefunction. One should be careful when the energy gap between two states is two small and can cause problem of division by zero. Later, the integration is done while a sufficient number of k-points is taken into accounts. We note again, the Chern number is associated with the number of 1D edge states. For a 2x2 band model spin matrices are conventional Pauli matrices:

$$\sigma_x = \begin{pmatrix} 0 & 1 \\ 1 & 0 \end{pmatrix}; \sigma_y = \begin{pmatrix} 0 & -i \\ i & 0 \end{pmatrix}; \sigma_z = \begin{pmatrix} 1 & 0 \\ 0 & -1 \end{pmatrix} \tag{2.6}$$

Under exchange energy, the four band model which consists of two p_z orbitals of Se atom. Since the basis was chosen as two spins up and two spins down, the spin matrices are defined as:

$$\sigma_x = \begin{pmatrix} 0 & 0 & 1 & 0 \\ 0 & 0 & 0 & 1 \\ 1 & 0 & 0 & 0 \\ 0 & 1 & 0 & 0 \end{pmatrix}; \sigma_y = \begin{pmatrix} 0 & 0 & -i & 0 \\ 0 & 0 & 0 & -i \\ i & 0 & 0 & 0 \\ 0 & i & 0 & 0 \end{pmatrix}; \sigma_z = \begin{pmatrix} 1 & 0 & 0 & 0 \\ 0 & 1 & 0 & 0 \\ 0 & 0 & -1 & 0 \\ 0 & 0 & 0 & -1 \end{pmatrix} \tag{2.7}$$

if the exchange field is out of plane, the bands with spin up and spin down are splitted in opposite directions by an energy proportional to the exchange energy. Hence, the new Hamiltonian under exchange energy is two interacting topological insulators model with Zeeman energy:

$$H_p = \begin{pmatrix} k^2/m_1 + M_z & d + k^2/m_2 & vk_x + ivk_y & 0 \\ d + k^2/m_2 & k^2/m_1 + M_z & 0 & -vk_x - ivk_y \\ vk_x - ivk_y & 0 & k^2/m_1 - M_z & d + k^2/m_2 \\ 0 & -vk_x + ivk_y & d + k^2/m_2 & k^2/m_1 - M_z \end{pmatrix} \tag{2.8}$$

where M_z specifies the exchange energy driven by proximity ferromagnetism. The eigensystems of the Hamiltonian are:

$$E_{1\mp}(k) = \frac{k^2}{m_1} \mp \sqrt{(\frac{k^2}{m_2} - M_z + d)^2 + v^2k^2} \tag{2.9}$$

$$E_{2\mp}(k) = \frac{k^2}{m_1} \mp \sqrt{(\frac{k^2}{m_2} + M_z + d)^2 + v^2k^2} \tag{2.10}$$

$$\Psi_{1-}(k) = \frac{1}{|\Phi_{1-}|}\{\frac{-1}{vk_-}(\frac{k^2}{m_2} - M_z + d + \sqrt{(\frac{k^2}{m_2} - M_z + d)^2 + v^2k^2}), \\ \frac{-1}{vk_-}(\frac{k^2}{m_2} - M_z + d + \sqrt{(\frac{k^2}{m_2} - M_z + d)^2 + v^2k^2}), 1, 1\}$$

$$\Psi_{1+}(k) = \frac{1}{|\Phi_{1+}|}\{\frac{1}{vk_-}(-\frac{k^2}{m_2} + M_z - d + \sqrt{(\frac{k^2}{m_2} - M_z + d)^2 + v^2k^2}), \\ \frac{1}{vk_-}(\frac{k^2}{m_2} - M_z + d - \sqrt{(\frac{k^2}{m_2} - M_z + d)^2 + v^2k^2}), 1, 1\}$$

$$\Psi_{2-}(k) = \frac{1}{|\Phi_{2-}|}\{\frac{-1}{vk_-}(\frac{k^2}{m_2} + M_z + d - \sqrt{(\frac{k^2}{m_2} + M_z + d)^2 + v^2k^2}),$$
$$\frac{-1}{vk_-}(\frac{k^2}{m_2} + M_z + d - \sqrt{(\frac{k^2}{m_2} + M_z + d)^2 + v^2k^2}), -1, 1\}$$

$$\Psi_{2+}(k) = \frac{1}{|\Phi_{2+}|}\{\frac{-1}{vk_-}(\frac{k^2}{m_2} + M_z + d + \sqrt{(\frac{k^2}{m_2} + M_z + d)^2 + v^2k^2}),$$
$$\frac{-1}{vk_-}(\frac{k^2}{m_2} + M_z + d + \sqrt{(\frac{k^2}{m_2} + M_z + d)^2 + v^2k^2}), -1, 1\}$$

The eigenvalues are doubly degenerate at zero magnetization, the $m_2 < 0$ which makes valence bands separated from conduction bands for layered model. Φ_i are normalization constants.

At zero exchange field, one can detect the degeneracy between $E_{1\pm}(k)$ and $E_{2\pm}(k)$. However, the wavefunctions expanding the Hilbert space carry different characteristics. When $k = 0$ the Hamiltonian at the Γ point:

$$H_0 = \begin{pmatrix} M_z & d & 0 & 0 \\ d & M_z & 0 & 0 \\ 0 & 0 & -M_z & d \\ 0 & 0 & d & -M_z \end{pmatrix} \tag{2.11}$$

having the energy states $E_{1\mp}(\Gamma) = \mp(M_z - d)$,$E_{2\mp}(\Gamma) = \pm(M_z + d)$, with the wavevectors: $\Psi_{1-}(\Gamma) = \frac{1}{\sqrt{2}}\{0, 0, 1, 1\}$ contributed by two orbitals with the same spin $\Psi_{1+}(\Gamma) = \frac{1}{\sqrt{2}}\{-1, 1, 0, 0\}$ $\Psi_{2-}(\Gamma) = \frac{1}{\sqrt{2}}\{1, 1, 0, 0\}$ $\Psi_{2+}(\Gamma) = \frac{1}{\sqrt{2}}\{0, 0, -1, 1\}$

Looking at the basis chosen to build the effective Hamiltonian, one notes that the degeneracy at zero exchange field is due to the combination of the wavefunctions in the vicinity of the Dirac cone. Consequently, the exchange field breaks band degeneracy in two opposite ways: The spin up states are lifted up, whereas spin down states are pulled down. The energy gap at the Γ point is calculated as the difference between E_{2+} and E_{2-} for $k = 0$ $\Delta E = -2(M_z + d)$ under small

magnetization $M_z < -d$ (d specifies hopping energy of the same spin type for different electrons, hence d is negative). At critical exchange field $M_c = -d$ a gapless Dirac cone is obtained. For large exchange field, the band inversion results in the change in energy gap definition at the Γ point: i.e., $\Delta E = 2(M_z + d)$. Hence, the evolution of bandstructure is as follow: Small exchange field applied in four band effective Hamiltonian for one QL narrows down the band gap. When the exchange field reaches a critical value comparable to hopping energy of two electrons with the same spin, the model exhibits a gapless Dirac cone at high symmetry point. Hence, the band gap increases linearly as a function of exchange field. Assume the Fermi energy lies in the middle of the band gap. The energy gap between lowest conduction band and highest valence band E_{2+} and E_{2-} for different wavevectors and exchange energy:

$$\Delta E(k) = 2\sqrt{(\frac{k^2}{m_2} + M_z + d)^2 + v^2k^2} \tag{2.12}$$

For small exchange field the highest valence energy and lowest conduction energy are located at the Γ point. The spin polarization at zero momentum:

$$\langle\sigma_{z1+}\rangle(\Gamma) = \langle\Psi_{1+}(\Gamma)|\sigma_z|\Psi_{1+}(\Gamma)\rangle = -1$$
$$\langle\sigma_{z1-}\rangle(\Gamma) = \langle\Psi_{1-}(\Gamma)|\sigma_z|\Psi_{1-}(\Gamma)\rangle = 1$$
$$\langle\sigma_{z2+}\rangle(\Gamma) = \langle\Psi_{2+}(\Gamma)|\sigma_z|\Psi_{2+}(\Gamma)\rangle = 1$$
$$\langle\sigma_{z2-}\rangle(\Gamma) = \langle\Psi_{2-}(\Gamma)|\sigma_z|\Psi_{2-}(\Gamma)\rangle = -1$$

Justifying our initial proposal of the band shift by Zeeman energy due to the spin at vicinity of the Γ point. We calculate the out of plane spin component as a function of the exchange field M_z, wave vector k for all different 4 bands.

$$\langle\sigma_{z1\pm}(k)\rangle = \langle\Psi_{1\pm}|\sigma_z|\Psi_{1\pm}\rangle;\langle\sigma_{z2\pm}(k)\rangle = \langle\Psi_{2\pm}|\sigma_z|\Psi_{2\pm}\rangle$$

$$\langle\sigma_{z2-}\rangle(k) = \langle\Psi_{2-}(k)|\sigma_z|\Psi_{2-}(k)\rangle = \frac{\alpha - 1}{\alpha + 1}$$

$$\alpha = \frac{1}{v^2k^2}(\frac{k^2}{m_2} + d + M_z - \sqrt{(\frac{k^2}{m_2} + d + M_z)^2 + v^2k^2})^2$$

$$\alpha = [-x + \sqrt{x^2 + 1}]^2 \text{ with } x = \frac{1}{vk}(\frac{k^2}{m_2} + d + M_z)$$

We look for the lower Dirac cone spintexture with serveral possibilities for exchange field and wave vector. The out of plane spintexture is circular around the Γ point which depends only on the parameter k in the first Brillouin zone.

For the case $M_z + d < 0$ the exchange energy is not sufficient to close the quantum tunnelling gap. The wavefunctions of upper and lower Dirac cone states follow a trivial topology with a hedgehog spintexture in which the total out of plane spin component is positive for upper Dirac band and negative for lower Dirac band ($\langle\sigma_{z2-}\rangle > 0$ and $\langle\sigma_{z2+}\rangle < 0$, exhibiting a trivial topological spintexture of the gapped Dirac cone). Since $\frac{k^2}{m_2} + d$ is the wave vector dependence hopping energy between orbitals with the same spin defining the initial tunnelling gap, small exchange field is not able to compensate the band gap. $x = \frac{k}{vm_2} < 0$ since $m_2 < 0$; $\langle\sigma_{z2-}\rangle(k) = \frac{\alpha-1}{\alpha+1}$ approaches zero when $k \to \Gamma$ and $\alpha \to 1$

$\langle\sigma_{z2-}\rangle(k) = \frac{\alpha-1}{\alpha+1}$ approaches 1 when $-\frac{k^2}{m_2} > vk$(the hopping energy between orbitals of the same spin is greater than spin-orbit coupling term) and $\alpha \to \infty$

Under large exchange field $M_z + d > 0$, the band gap opens linearly as a function of exchange energy and it indicates that the two topological phases can not adiabatically connected. For the wave vector at vicinity of the Dirac cone $\alpha \to 0$ and $\langle\sigma_{z2-}\rangle(k \to \Gamma) = -1$. When

$$k \to k_c = \sqrt{-m_2(M_z + d)}, \alpha \to 1 \tag{2.13}$$

the total z spin component reaches zero $\langle\sigma_{z2-}\rangle(k \to k_c) = 0$. One notes that the critical k-point $k_c$which defines the band inversion region increases as function of exchange field.

The out of plane spin components after phase transition follow a non-trivial topology signifying by the band inversion at vicinity of the Dirac cone $k \ll k_c$,

i.e., the spin experiences an inversion from negative to positive at critical momentum $k_c = \sqrt{-m_2(M_z + d)}$. This is a function of exchange field and hopping energy and becomes positive at large momentum. [1]

Figure 2.2 demonstrates the evolution of Topological Surface State (TSS) under exchange field based on the four band effective Hamiltonian for ultra-thin TI film with the unconventional spin-texture which has been proposed analytically above. The arrows indicate the spin polarization. A gapped TSS with zero net magnetization, in which all the degeneracies are survived is presented in Figure 2.2.a. As a result of a small magnetization with efficiency being smaller than the tunnelling gap (or the critical exchange field), i.e., $M_z < M_c$ (see Figure 2.2.b). Figure 2.2.c shows a perfect spin polarized Dirac cone at critical exchange energy. The total out of plane spin component at the vicinity of the Dirac cone is zero. When the exchange field overcomes the critical value $M_z > M_c$ the band inversion is followed by a spintexture inversion which leads to the change in topological band structure. The size of inversion region is dependent on the magnetic exchange energy. The Dirac energy dispersions with magnetic gap demonstrates a non-trivial spin-texture. The bands experience a change in direction of the spin from negative to positive out of plane spin for lower magnetic gapped Dirac band, and vice versa for upper Dirac band (see Figure 2.2.d).

The Berry curvature tuned by magnetization contributes to the total topological Chern number characterising the quantum Hall effect. The effective four-band Hamiltonian explains the gapped topological surface state for one quintuple layer 3D TI in finite size limit. Moreover, the Berry curvature in time reversal broken topological phase exhibits a peak at the Γ point, contributed majority to the total Chern number. To understand the Berry curvature we analyse the partial Berry curvature of the lowest conduction band and highest valence band as a function of spintexture and momentum. Based on Kubo formula which involves particle-hole scattering process, the Berry curvature of the gapped Dirac

[1] For four band model, the out of plane spintexture of upper and lower Dirac bands reversed $\langle \sigma_{z2+} \rangle(k) = -\langle \sigma_{z2-} \rangle(k)$

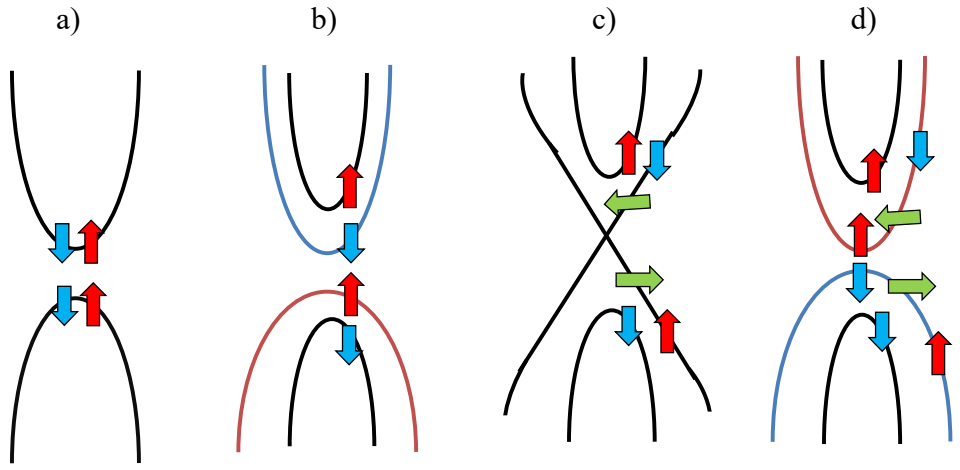

Figure 2.2: Evolution of sub-band structure under exchange field for ultrathin topological insulator film. (a) Gapped Dirac cone under zero exchange field with the bands doubly spin degenerated. (b) Energy level splitting due to the small exchange energy $M_z < M_c$. (c) A perfect spin polarized Dirac cone at critical exchange energy. The total out of plane spin component at the vicinity of the Dirac cone is zero. (d) $M_z > M_c$ the band inversion is followed by a spintexture inversion which leads to the change in topological band structure.

state with quadratic dispersion can be expressed (see eq. 2.5). We note that there should be doubling in the Ω_2:

$$\Omega_2(k) = \frac{Im[\langle\Phi_{2-}|\frac{\partial H}{\partial k_x}|\Phi_{2+}\rangle\langle\Phi_{2+}|\frac{\partial H}{\partial k_y}|\Phi_{2-}\rangle]}{(E_{2-}-E_{2+})^2}(n_f(E_{2-})-n_f(E_{2+})), \tag{2.14}$$

$$\frac{\partial H}{\partial k_x} = \begin{pmatrix} 2k_x/m_1 & 2k_x/m_2 & v & 0 \\ 2k_x/m_2 & 2k_x/m_1 & 0 & -v \\ v & 0 & 2k_x/m_1 & 2k_x/m_2 \\ 0 & -v & 2k_x/m_2 & 2k_x/m_1, \end{pmatrix} \tag{2.15}$$

$$\frac{\partial H}{\partial k_y} = \begin{pmatrix} 2k_y/m_1 & 2k_y/m_2 & i.v & 0 \\ 2k_y/m_2 & 2k_y/m_1 & 0 & -i.v \\ -i.v & 0 & 2k_y/m_1 & 2k_y/m_2 \\ 0 & i.v & 2k_y/m_2 & 2k_y/m_1, \end{pmatrix} \tag{2.16}$$

$$\Omega_2(k) = \frac{16}{\Delta E(k)^2\Phi_{2+}^2\Phi_{2-}^2.k^2}\cdot\sqrt{(\frac{k^2}{m_2}+d+M_z)^2+v^2k^2}.(M_z+d-\frac{k^2}{m_2}), \tag{2.17}$$

When $M_z < -d$, the momentum dependence Berry curvature is negative for $k < k_0 = \sqrt{m_2(M_z + d)}$ and positive for large momentum $k > k_0$. One possible explanation for trivial insulating phase is the cancellation of the topological Chern numbers for top and bottom surface for ultra-thin TI films ($\pm\frac{1}{2}$), hence the total Chern number for tunnelling TI is 0.

When $M_z > -d$, the Berry curvature is always positive due to the spin inversion, the exchange field is sufficiently strong to close the tunnelling gap and transform the Chern number of one surface with negative Chern number to a positive value. Thus, the total Chern number under large magnetization is non-zero, indicating a non-adiabatic topological phase transition from trivial insulating phase to non-trivial QAH one. The integration for Chern number consists of two part: a part with one half Chern number $k \leq k_c = \sqrt{-m_2(M_z + d)}$ with a non-trivial inverted spintexture, the other half is conventional trivial contribution.

2.2 Layer dependence bandstructure and spintexture

Pristine Bi_2Se_3

Figure 2.3.(a-d) shows calculated bandstructure for layer thickness of 1, 4, 8, 16 QLs, respectively. It is interesting to note that when the number of QLs increases and is larger than tunnelling length (above 6QLs) of top and bottom surface wave-functions, the surface state exhibits a perfect gapless Dirac cone. When the slab thickness increases, the bulk bands become closer together and become continuous for infinite thick slab, whereas the bands are discrete for a small number of layers. At very large thickness, the spin up and spin down states of top surface have weak interaction with spin up and spin down of bottom surface. Moreover, when the thickness of the film is reduced to only several nano-meter, overlapping between the surface state wavefunctions from the two

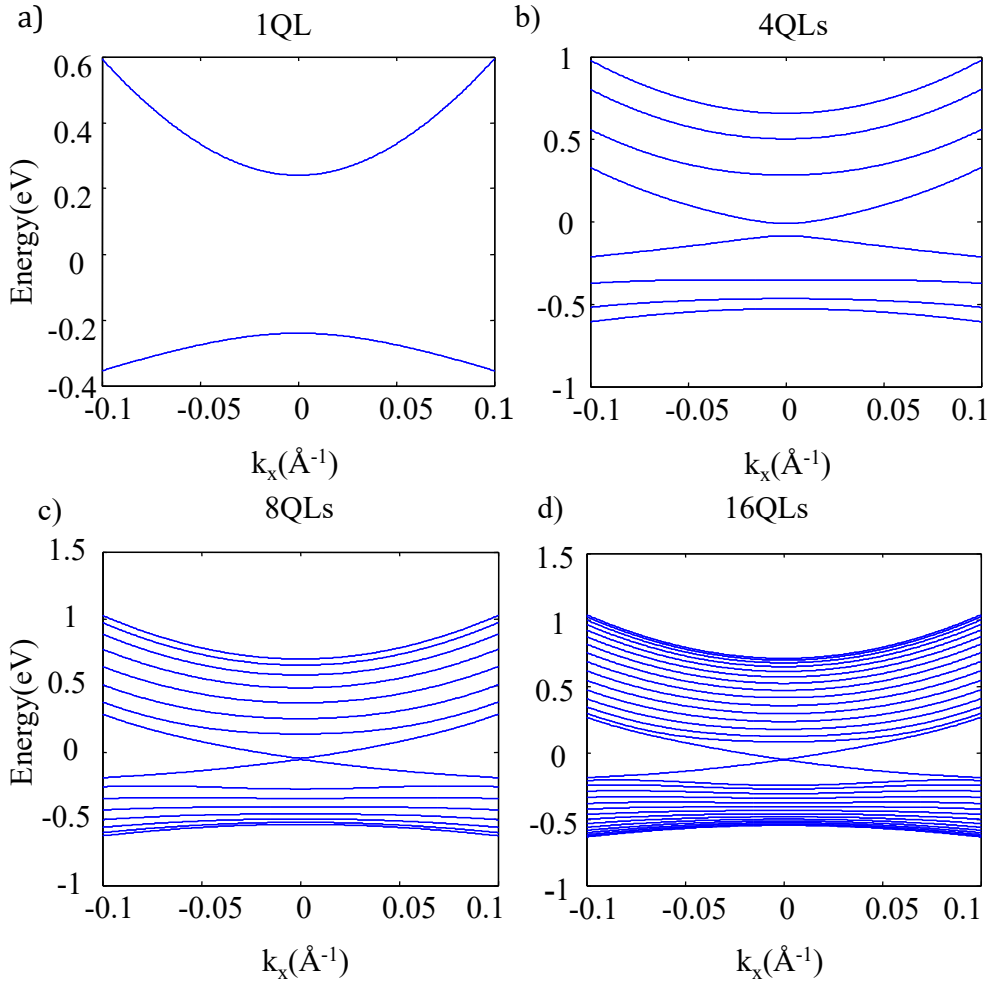

Figure 2.3: Thickness dependence bandstructure of Bi_2Se_3 which captures main features of low energy spectra (a) 1QL, (b) 4QLs, (c) 8QLs, (d) 16QLs slabs.

surface states of the film becomes non-negligible, and hybridization between them has to be taken into account [44]. As a result, a small band gap opens at the Γ point. The tunnelling effect can be simply demonstrated by a Hamiltonian: $H = \begin{pmatrix} T & \Delta \\ \Delta^\dagger & B \end{pmatrix}$ where T,B indicate the Hamiltonian for top and bottom surfaces, Δ is the interaction term. In the ultrathin film model for one QL described above, the tunnelling term shows a parabolic like dispersion. The topology of band structure can not be distinguished with original insulator phases. However, as thickness of TI slab is enough, the band gap drops for 16QLs, approaching 0.

For Bi_2Se_3 the parameters are controlled to show a bulk gap of 0.3eV. In addition, the states contributed by p_x and p_y orbitals of Bi and Se are negligible near

the Fermi level. In the thick slab limit, the band gap closes, showing linear energy dispersion around the Dirac cone. The quantum well states separate from surface state due to the interlayer hopping energy when the interlayer tunnelling term T is large enough.

Magnetically doped Bi_2Se_3 We look for three possible magnetic configurations: one substrate induced ferromagnetism (Ferromagnet–Topological Insulator (FM-TI)), two substrate induced ferromagnetism (FM-TI-FM), whole slab doping (see Figure 2.4.(a–c), respectively). While the conventional model are based on low energy spectra and captures only surface state, our model is more flexible in term of magnetic configurations. Realistically, if capping the TI thin film in the middle while the magnetization can acts on separate surfaces of TI thin film, and having the same magnetic direction (Figure 2.4.(b)). It is possible that the magnetization can have different directions and a gap can simply open without signal of phase transition. As can be seen from the figure 2.4.(a–c), the spontaneous magnetization is directed perpendicular to the surface of TI, breaking the time reversal symmetry.[2] The magnetic direction can be controlled by a small magnetic field in the opposite direction. Presumably the magnetic substrates are coupled with only surface QLs, while in the whole slab doping configuration the magnetic exchange energy has effect on all layers. We simulate the effect of the proposed proximity induced ferromagnetism by including the exchange field to the spin matrix of the last QL for the first case, two surface spin matrices for the second structure, and total spin matrix for the whole slab doping case. The TI model with magnetic impurities on one surface is adapted for various exchange energy scales, the results are presented in Figure 2.5.(a–d) for $M_z = 0$eV, $M_z = 0.1$eV, $M_z = 0.24$eV, $M_z = 0.375$eV, respectively. As presented in the schematic model and previous band structure, the ultra-thin TI

[2]Note that if magnetization is applied parallel to the surface, the Dirac cones are only shifted away from the Γ point.

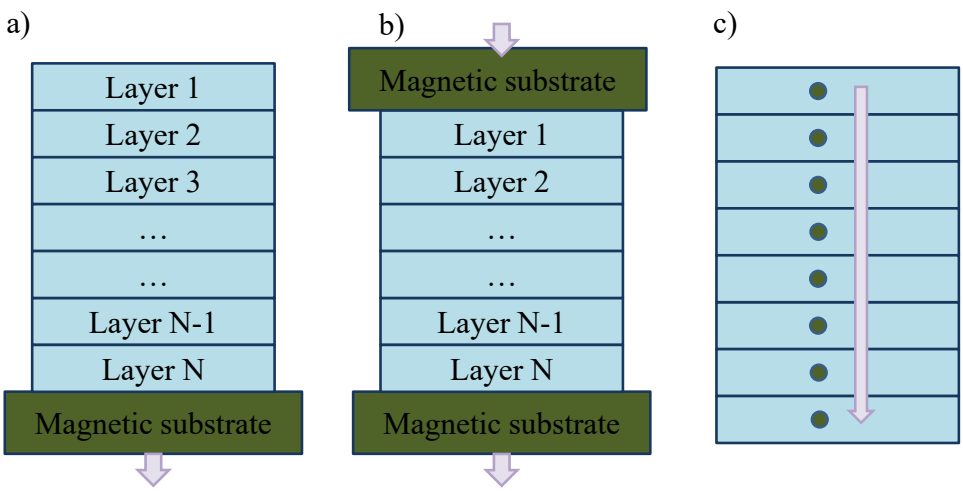

Figure 2.4: Simplified material structure with different magnetic configurations, the arrows indicate direction of magnetization: (a) one substrate induced magnetic ordering, (b) two substrate induced magnetic ordering, (b) whole slab doping.

film of 4QLs shows a band gap due to the tunnelling effect as mentioned above instead of a perfect Dirac cone. When a small exchange energy is applied on one surface, the two surface states lose twofold spin degeneracy (see Figure 2.5.a). The quantum well states show the same behaviour i.e., they split upon magnetization. As can be seen in Figure 2.5.b, when the exchange ferromagnetic energy is small, there are two states moving in opposite directions with respect to the Fermi level, leading to a decrease in band gap. Afterwards, a linear touch is also presented in critical TPT point (see Figure 2.5.c). When the exchange energy is larger than a critical value (see Figure 2.5.d), the band gap gradually increases as a function of M_z in contrast to the small magnetization.

From Figure 2.6, the band gap at Γ point is presented as a function of thickness and for different magnetic structure. The critical exchange field M_z at which the direct band gap at Γ point closes and reopens can also be seen. This indicates a phase transition which motivates our further study of Chern number characterizing the band structure topology. For FM-TI structure, the critical exchange energy is almost identical for all thickness, varying around $0.24eV$, depending on parameter d in Eq.2.2. The critical exchange field for multiple QLs model is slightly larger than for one QL with a negligible difference. Hence, the crit-

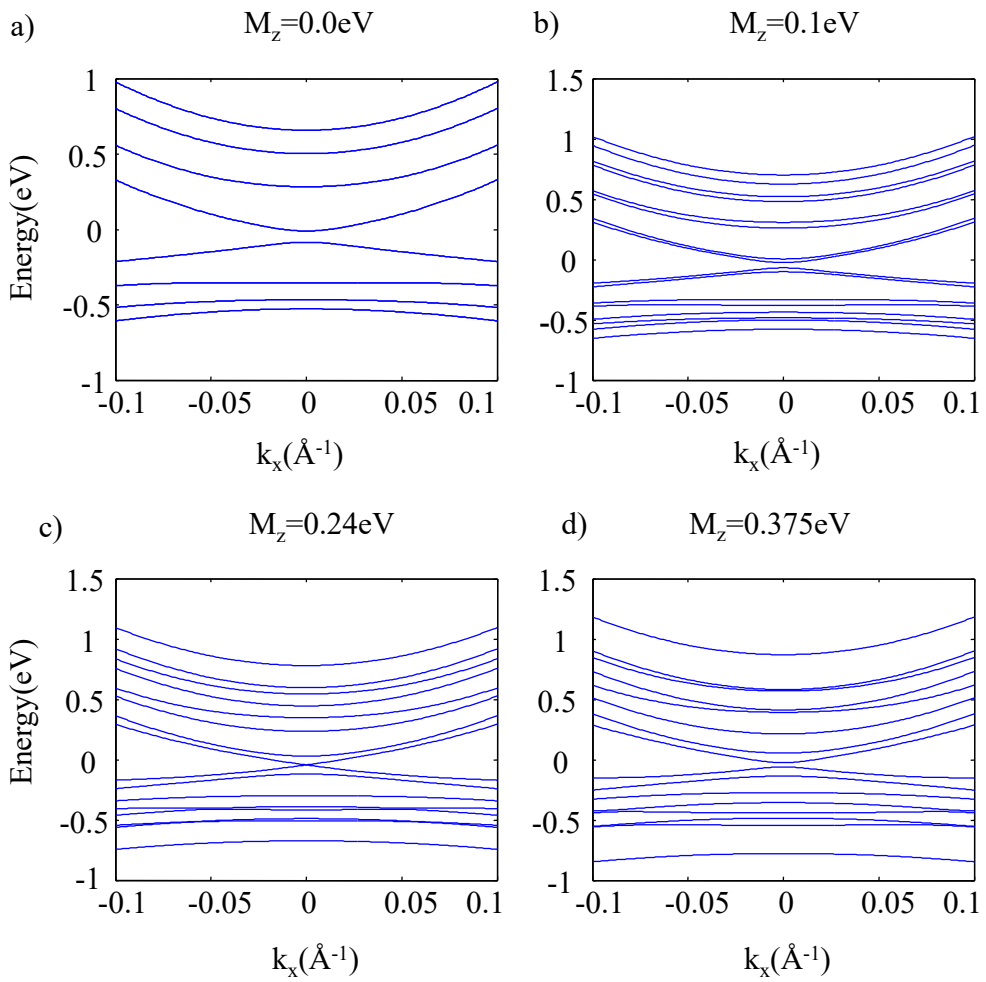

Figure 2.5: Realistic band-structure calculated of 4QLs under magnetic doping for different exchange fields. (a) $M_z = 0$eV, (b) $M_z = 0.15$eV, (c) $M_z = 0.25$eV, (d)$M_z = 0.35$eV

ical exchange energy should be confirmed experimentally in term of sufficient magnetic dopant's concentration to trigger dissipasionless Hall current.[3]

We look for a simplified effective model of topological insulator with arbitrary thickness.

$$H_{FM-TI} = \begin{pmatrix} T & \Delta_L \\ \Delta_L^{\dagger} & B + \sigma_z M_z \end{pmatrix}$$

The initial gap value is proportional to the interaction between the two Dirac cones. At critical exchange energy, the gap at the Γ point closes when the field is sufficient to compensate the tunnelling gap. In the FM-TI case, the effective mag-

[3]Note that a perfect Dirac cone of pristine Bi_2Se_3 can not obtained for finite thickness since the tunnelling effect of the two opposite surfaces always exists, in the ARPES study for thick slab limit the gap is not present due to the small scale of a band gap.

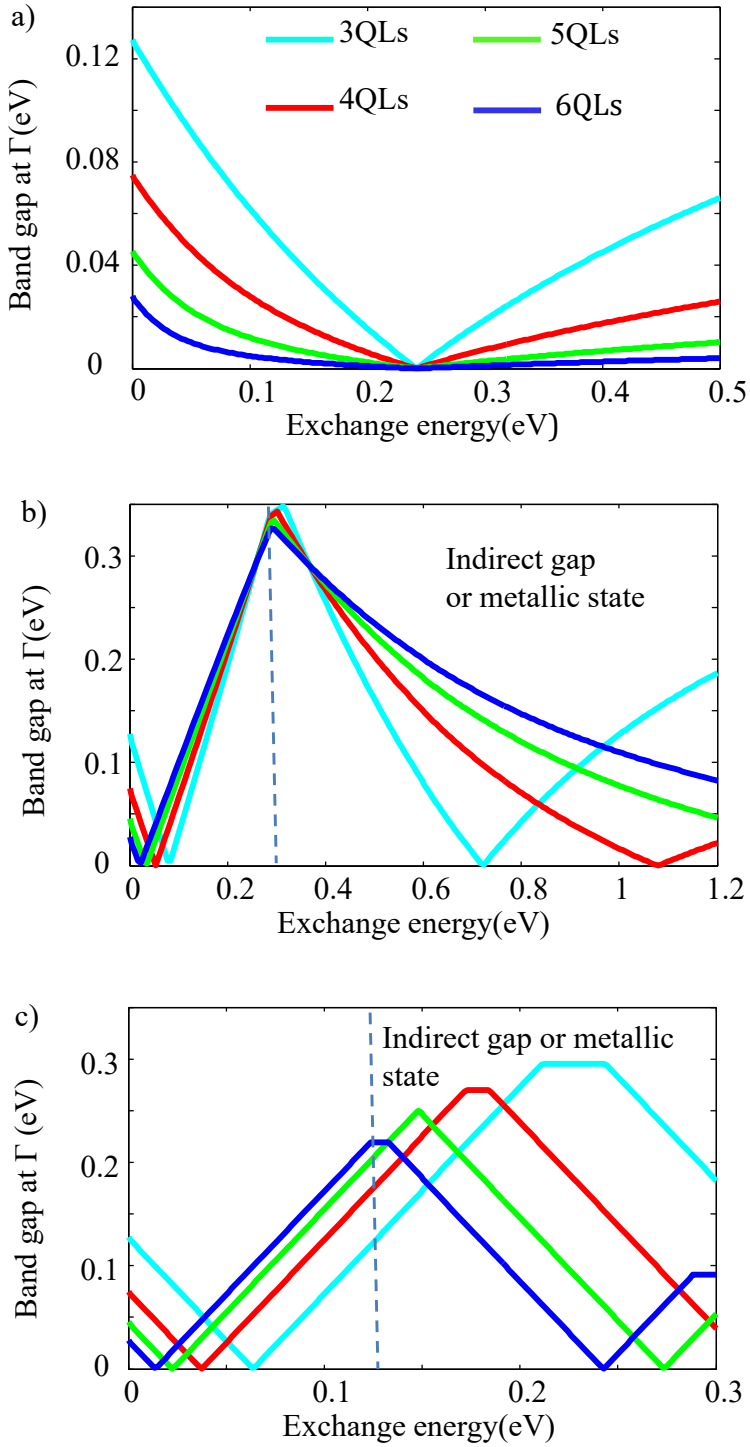

Figure 2.6: Evolution of the band gap at the Γ point as function of M_z and film thickness, critical M_z dependence on number of QLs. (a) One substrate induced ferromagnetism. (b) Sandwitching TI slab between two magnetic layer i.e., FM-TI-FM (c) Whole slab doping gap evolution

netization is less effective compared to the exchange field generated from the 4x4 model. Here, we note that the tunnelling gap and the inter-layer coupling de-

cide the critical exchange field needed to drive the system to QAH phase. We consider a simplified effective model of TI with arbitrary thickness, considering the tunnelling term as a function of thickness. At critical exchange energy, the gap at the Γ point closes when the field is sufficient to close the tunnelling gap in opposite surface (we still have some intermediate contribution from the bulk layers) and reopen it. The effective critical exchange field needed to tunnel through bulk QLs to take effect on top QL with a smaller initial tunnelling gap. Curiously, the similarity in tendency of tunnelling gap, effective interlayer hoping energy as well as the effective exchange energy for FM-TI structure gives us almost unchanged realistic critical magnetization (see Figure 2.6.a). However, the parameters are material specific, one has to confirm that the numerical study performed depends largely on the energy scale of the specific band-structure and from the experimental point of view the change in critical exchange field for FM-TI structure is negligible.

As can be seen from Figure 2.6.a, the band gap closes and reopens only once for FM-TI structure. Such robust layer-independent QAH effect is, however, not present in the cases of FM-TI-FM structure and the homogeneous doping. In the latter cases, while M_c decreases with increasing number of QLs, the QAH gap grows linearly with respect to the exchange energy. The drop in critical exchange field with respect to the slab thickness is a result of the decrease in inter-surface interaction. Comparing three different magnetic configurations, we confirm that the critical exchange energy at which the Chern number becomes 1 is smallest for the whole slab doping case showing the most significant expansion in magnetic gap as a function of magnetization, followed by FM-TI-FM structure. Thus, homogeneous magnetic doping is the most promising candidate to the real low power-consumption electronic devices. On the contrary, the FM-TI structure is predicted to open smallest magnetic gap. The second and third magnetic structures can demonstrate multiple gap closing in which the band gap at the Γ point closes and reopens more than once at the Γ point only, indicating

two TPT (see Figure 2.6.(b–c)). We will demonstrate the band-structure in the next sub-section.

To further show the proof of multiple gap closing and in-direct band gap transition at high exchange field limit for the FM-TI-FM and homogeneous doping proposed in Figure 2.6.(b–c), we demonstrate the bandstructure evolution under strong exchange field of 4QLs slab for FM-TI-FM in Figure 2.7 and Figure 2.8. The TPT mechanism has no significant difference compared to FM-TI structure except for the indirect band gap at high exchange fields (see Figure 2.8.a). In addition, more complicated bands can involve in low energy spectra and the material becomes metallic (see Figure 2.8.(c–d)). The calculation of second TPT point will be presented in next chapter for another class of tunable TI.

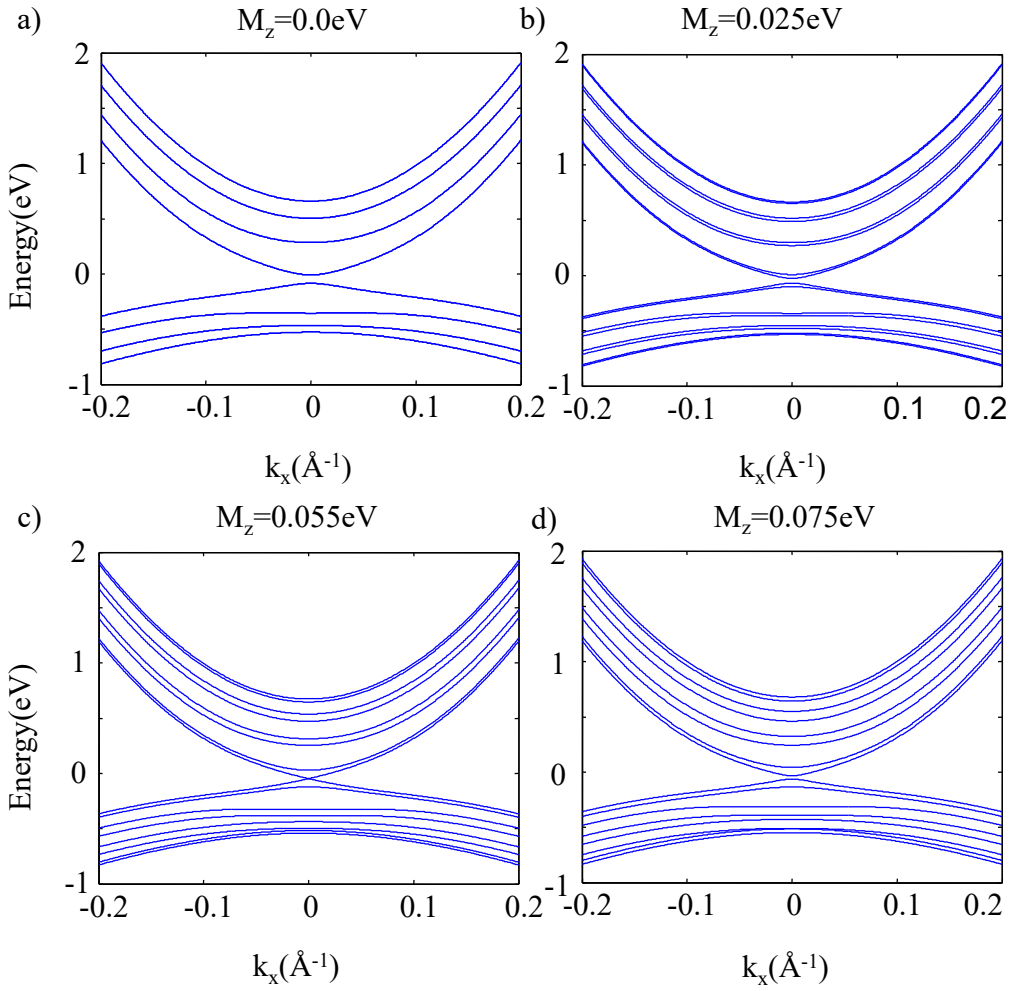

Figure 2.7: Bandstructure evolution under strong exchange field for FM-TI-FM structure, first TPT. (a) $M_z = 0$eV, (b) $M_z = 0.025$eV, (c) $M_z = 0.055$eV, (d) $M_z = 0.075$eV.

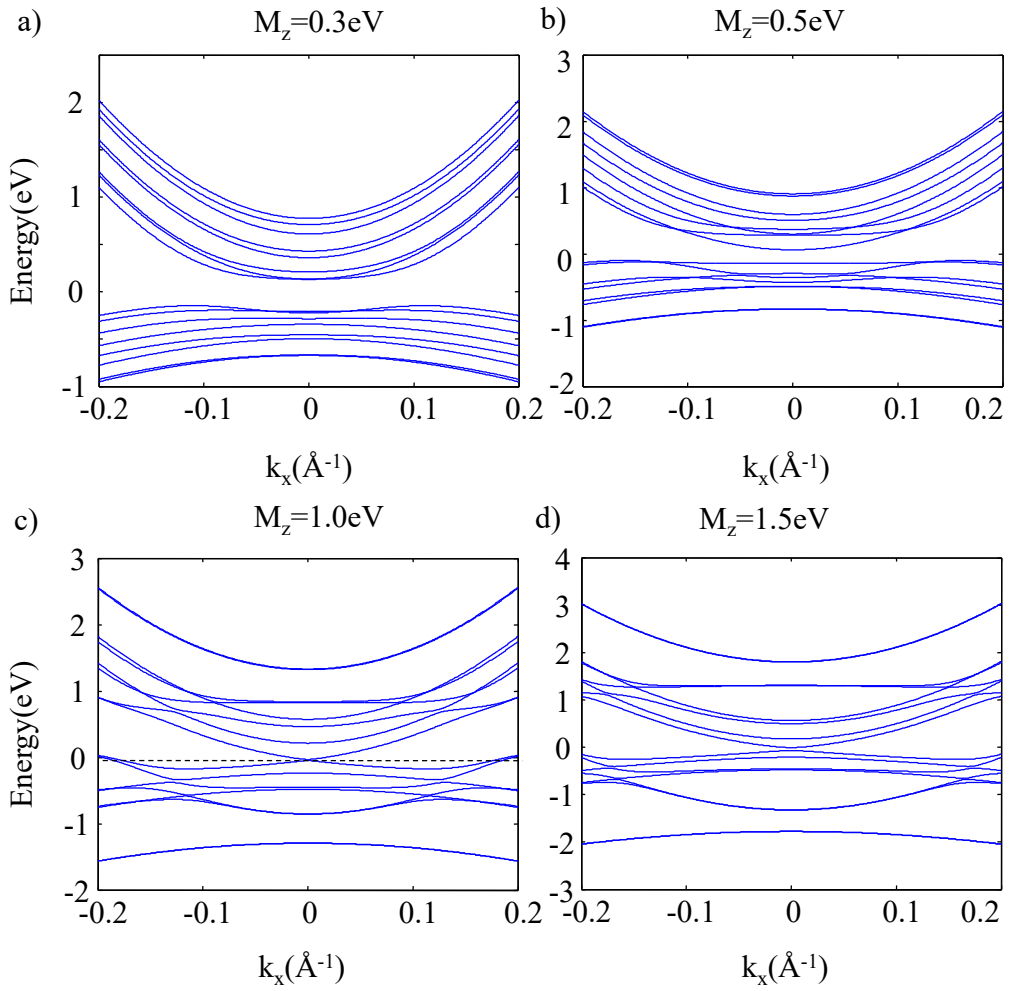

Figure 2.8: Second TPT at the Γ point, the material could not maintain insulating state under high exchange field. (a) $M_z = 0.3$eV, (b) $M_z = 0.5$eV, (c) $M_z = 1.0$eV, (d) $M_z = 1.5$eV

Spintexture of Dirac bands

As can be seen from the Figure 2.9 the out of plane spin component expressed in term of the density at vicinity of the upper and lower Dirac cones has a perfect circular shape i.e., symmetric around the Γ point in consistency with the effective four band Hamiltonian studied analytically above. The total z spin component at the Γ point is always ± 1 unpon applying the magnetic exchange energy indicating that the total inplane spin components of the system are zero at the Γ point. Assuming that under exchange energy not large enough to cause a band

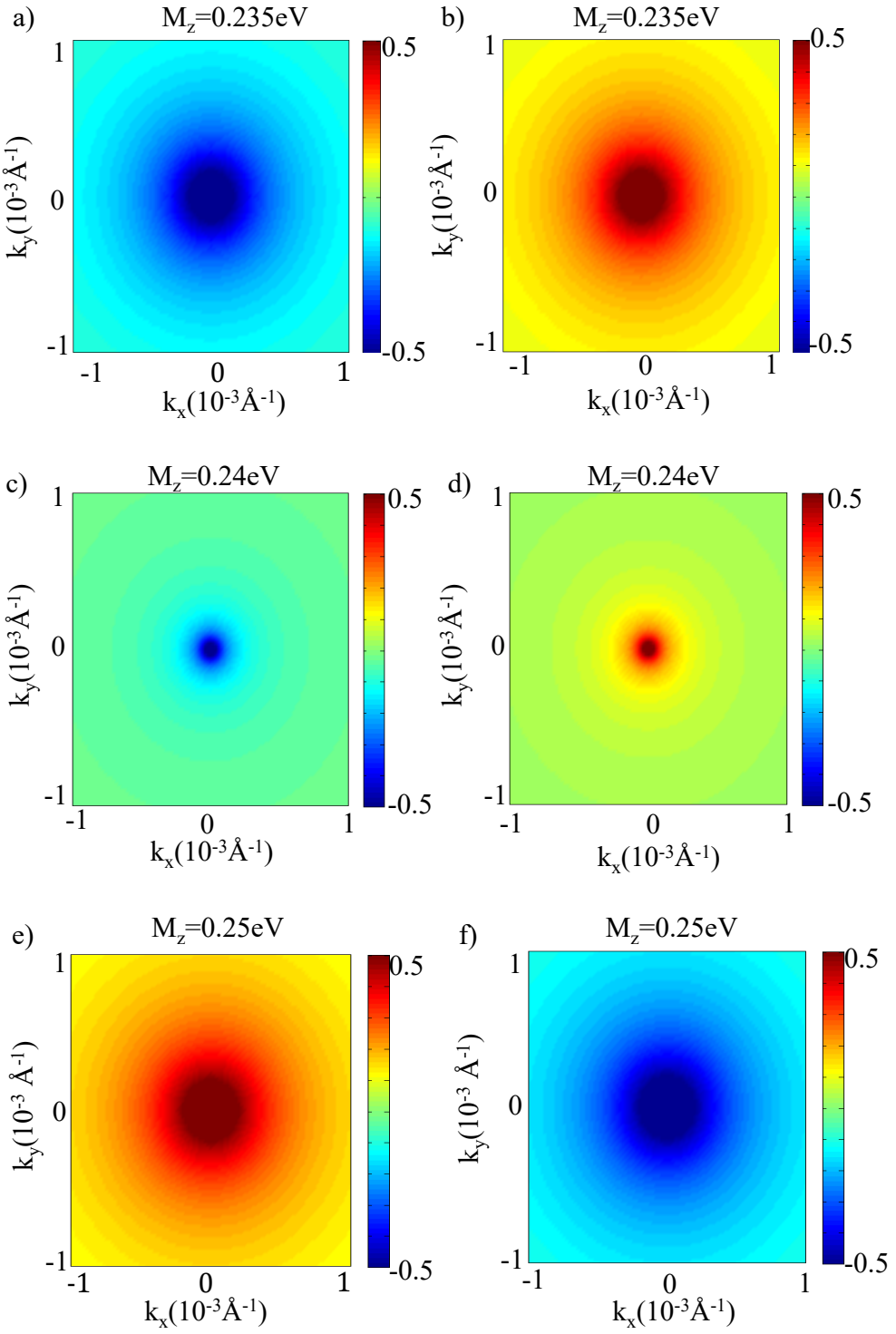

Figure 2.9: Evolution of z-spin density around the Dirac cones before and after phase transition, the left-side figures stand for the upper Dirac state, the right-side: lower Dirac cones. (a–b) $M_z = 0.235$eV, (c–d) $M_z = 0.24$eV, close to M_c, (e–f) $M_z = 0.25eV$

mixing between bulk QLs and surface QLs, the valence band maximum and conduction band minimum are always located at lower and upper Dirac cones,

respectively. In consistent with our initial proposal in Figure 2.2 we observed two distinctive spin textures before and after gap closing. Before gap closing at $M_z = 0.235$eV and $M_z = 0.24$eV, z-spin component of the top surface is positive for upper Dirac cone and negative for lower Dirac cone at small momentum. After gap closing at $M_z = 0.25$eV the direction of z-spin reversed, indicating a topological phase transition. The z-spin is positive for upper Dirac cone, and negative for lower Dirac cone for all surfaces at TPT. The top surface z-spin component contributed the most to the total spin, indicating strong spin polarized behavior at around the Γ point. We note that applied exchange field is at bottom layer, and the spin density is computed at topmost surface layer. From Figure 2.9 it can be seen that the behaviour of z-spin component of different QLs at the vicinity of Dirac cone is the same although their polarization strength is different. One possible explanation is that for FM-TI structure where the inversion symmetry is broken, the low energy wave-function come mainly from top QL. For QAHE with $M_z = 0.3$eV, the layer dependence spintexture shows that the z-spin of the top QL at small momentum is the main contribution to the whole system, whereas the negative spin polarization at large momentum mainly comes from bottom surface where the magnetization is applied (see Figure 2.10.b).

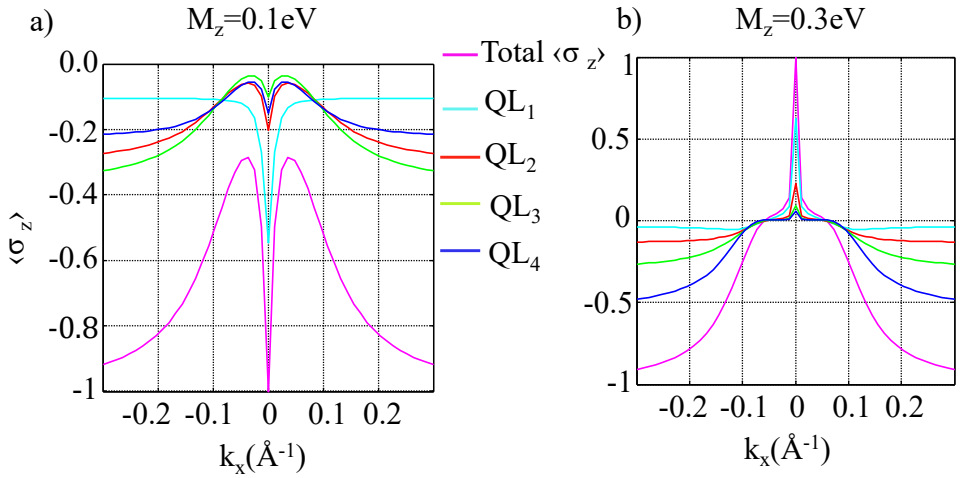

Figure 2.10: Layer dependence out of plane spin polarization of upper Dirac cones before and after phase transition along k_x direction for FM-TI structure for (a) $M_z = 0.1$eV: trivial (b) $M_z = 0.3$eV: QAH.

Chirality of the spintexture

The spin components are computed within one first surface quintuple layer in Figure 2.11(a–b) in trivial and QAH side, respectively. The colour indicates the out of plane spin polarization. One notes that a chiral spintexture (left handed or right handed) for surface bands is specific property for Z_2 TI. The total spin components are expected to be nonzero due to the band splitting and broken inversion symmetry in FM-TI, in contrast with zero total inplane spin for FM-TI-FM and homogeneous doping (we have proved analytically the zero inplane spintexture of single layer Hamiltonian under magnetization in the previous section). While the topmost surface shows left-handed spintexture for upper Dirac cone, the bottom surface shows right-handed spintexture for lower Dirac cone with the inversion symmetry. Due to SOC interaction, the spin-momentum are locked for TI phase. In a perfect TI, the spin texture gives rise to a non-trivial Berry phase for the topological surface states and suppresses the backscatterings under TRS, leading to possible device applications in spintronics [17]. One should note that although for the FM-TI-FM and homogeneous doping cases, the exchange field does not break inversion symmetry but if considering only in-plane spin of top surface, the spintexture is helical. Figure 2.11(c–d) shows that the spin polarization at bottom QL is weak at vicinity of the Γ point, and the helicity also changes at large momentum. By contrast, the chiral spintexture of top surface tend to be more conservative upon the TPT (see Figure 2.11(a–d)).

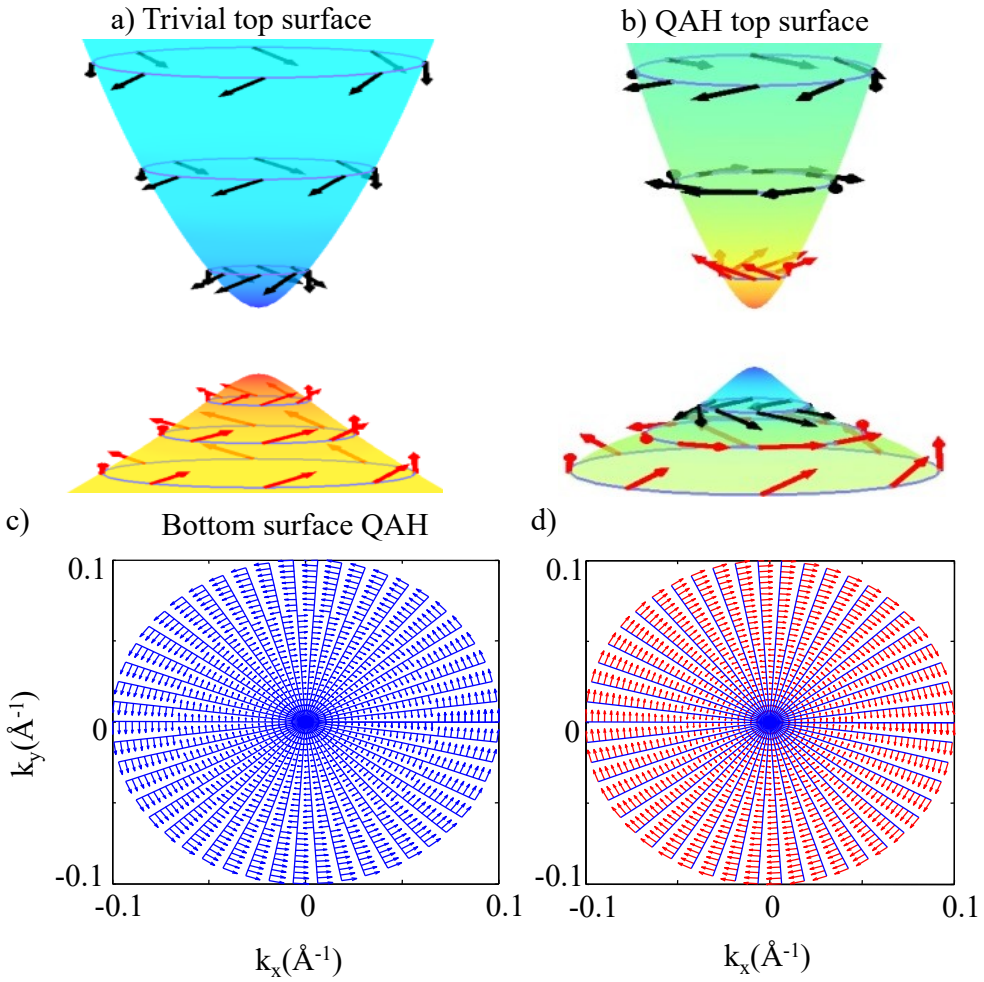

Figure 2.11: Evolution of surface inplane spin components of the two Dirac cones under magnetic perturbation. (a) The surface spin-textures for FM-TI structure for trivial side, (b) The skyrmion spin-textures for surface QL in QAH phase. (c) The inplane spintexture of bottom QL in QAH state. Blue-upper Dirac cone, (d) Red–lower Dirac cone in the.

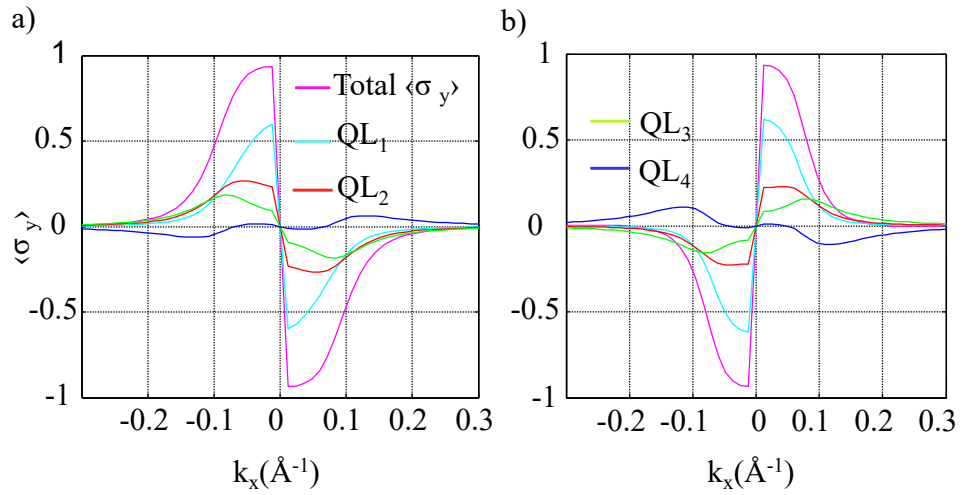

Figure 2.12: Layer dependence inplane spin polarization of Dirac cones after phase transition along k_x direction for 4QLs. (a) Upper Dirac cone, (b) Lower Dirac cone

Figure 2.12 demonstrates the layer-dependence $\langle\sigma\rangle_y$ of the two Dirac cones in QAH state. Due to the interlayer tunnelling effect, $\langle\sigma\rangle_y$ carries the same sign for all slab except for last QL. The in-plane spin crosses zero value three times. Figure 2.12 further revealed the complexity of chiral character in quantum tunnelling tunnelling limit: At large momentum the TR broken spin chirality at bottom surface is: right handed for large momentum, transforming to left-handed at small momentum k.

The surface state of TI

To investigate the band evolution of nearly perfect TSS with Dirac cone, we computed the surface band by tuning magnetic exchange field for FM-TI structure. We use thick slab limit to avoid tunnelling effect without interlayer tunnelling. The weight of a band is computed by a proportion of surface wave component with respect to the wavefunction normalization factor. For example, the topmost surface band components of lower Dirac cone state is $\Psi_{1,k}$, $\Psi_{2,k}$ for spin up, with

$$\Psi_k = (\Psi_{1,k}, \Psi_{2,k}, ..., \Psi_{4N-1,k}, \Psi_{4N,k}) \tag{2.18}$$

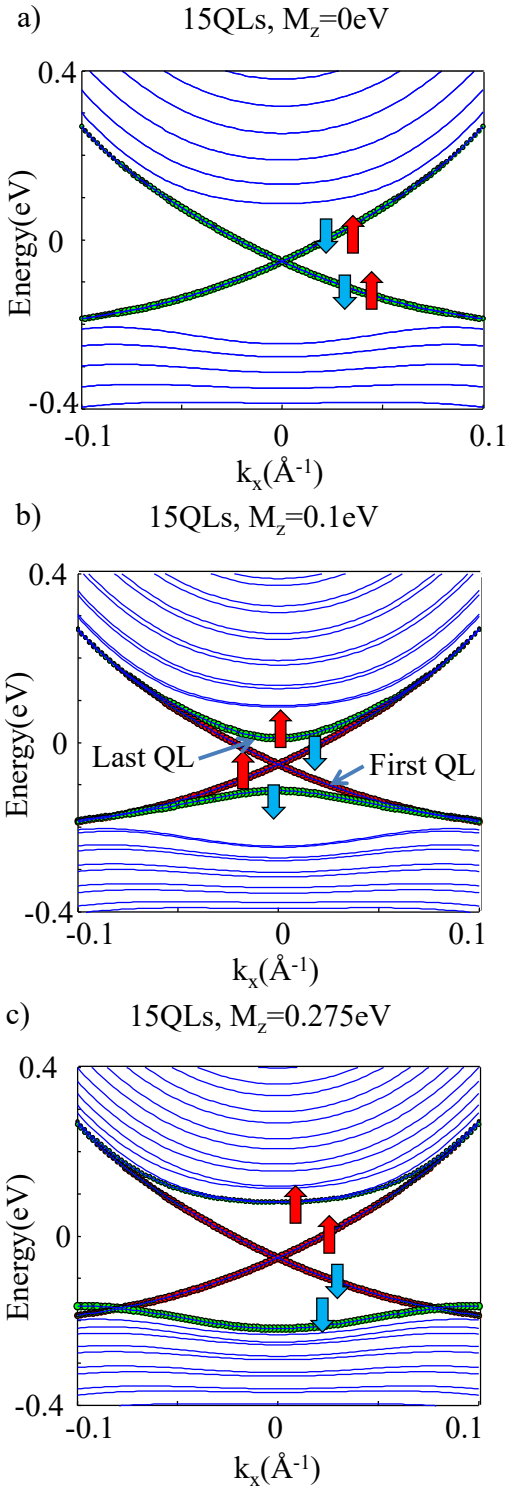

Figure 2.13: Surface band of 15QLs slab under magnetic perturbation. (a) $M_z = 0$eV, (b) $M_z = 0.1$eV, (c) $M_z = 0.275$eV

being the lower Dirac cone surface state for a kpoint. Hence, the weight of top-most surface spin-up component can be expressed as:

$$W^2_{\uparrow,k} = \frac{|\Psi_{1,k}|^2 + |\Psi_{2,k}|^2}{||\Psi_k||^2} \tag{2.19}$$

The tunnelling effect is non-negligible in thick film limit, thus for a slab of 15QLs its direct gap is some percentage of meV. At zero exchange energy, the surface state comes from both spin up and spin down components. Upon applying small exchange energy, the twofold degenerated band separates into spin up and spin down state: Spin up bands move up and spin down bands move down with respect to the Fermi level [45]. However, the gap closing at thick slab limit is quite difficult to observe, and the gap opened is small as mentioned in previous section. Figure 2.13 demonstrate that at very thick film limit, the FM-TI is not a potential structure for QAH experiment. The arrows indicate the spin polarization direction, whereas the green and red colour indicate the surface states of bottom and the top QLs, respectively. The FM layer, which acts on last QL can straightforwardly open the gap on bottom, however, could not open a considerable gap for top QL. Finally, at large exchange field a single spin polarized Dirac cone still survives (see fig 2.13.(b–c)).

2.3 Electric field effect

If electric field is applied in z direction, there is a potential gradient which breaks the reflection symmetry of the Hamiltonian. The two surface states are no longer degenerated due to potential difference. While a electric field is applied perpendicular to one slab surface, the potential difference does not break TRS. However, there is a shift at the Dirac point for upper and lower surfaces. The splitting of two surface states is more prominent at larger wave vectors but disappears at the Γ point. This is a Rashba-type splitting, in which the two sub-bands with different spin shift along the $k_{//}$ axis in opposite directions and degenerate at the Γ point [44].

Figure 2.14.a shows that we invoke thick slab limit to compute the surface

[4]We assume Fermi level is located in the middle of the two Dirac cones

[5]We applied magnetic exchange energy in -z direction, if the field is in +z direction the spin z components are reversed

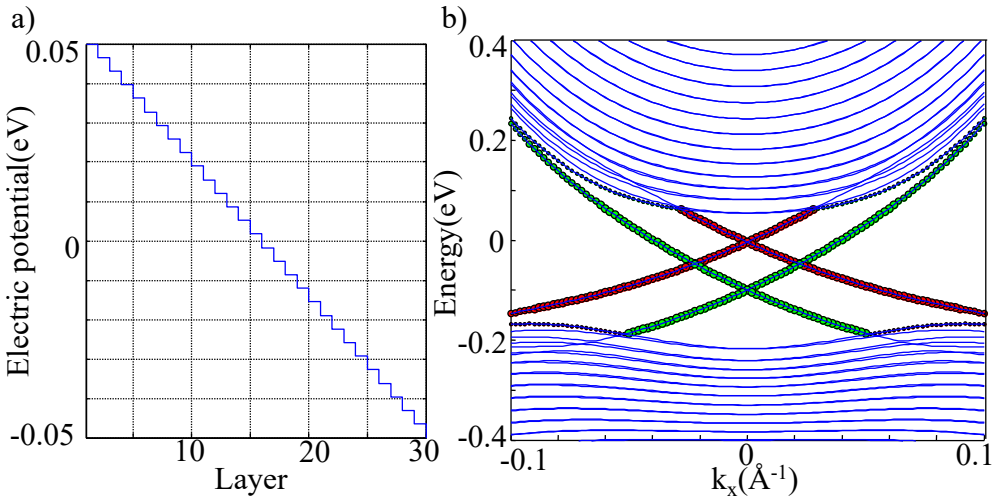

Figure 2.14: Effect of electric field, red color: surface band of top QL, green color: surface band of bottom QL. (a) Linear potential profile of 15QLs. (b) Calculated bandstructure for 15QLs with electric field.

state, assuming that the potential difference within one QL is negligible. Significantly, the top surface state is lifted up for the first QL with higher potential, whereas the surface state of bottom QL is pulled down with the weight indicated by red and green circles, respectively. Hence, the surface states also demonstrate Rashba-type spin-orbit splitting because the dielectric substrate-induced potential difference and more bulk bands emerge. The larger the potential difference applied, the larger the separation between two Dirac cones obtained. Moreover, the splitting is more prominent at thicker model due to highly asymmetric potential. There are two other Dirac cones formed by band crossing of top and bottom surfaces. Although we adapted the model to a thick slab, the tunnelling effect still exists between the two surfaces. In the two symmetric Dirac cones which are shifted away from the Γ points, two band gaps opened as a result of inter-surface quantum tunnelling.

In addition, the substrate effect was also modelled by implying effective potential along the film normal direction $V(z)$, the dispersions are obtained, the energy separation ΔE becomes proportional to $V(z)$. A simple model Hamiltonian can refer back to two interacting Dirac cone model for arbitrary thickness in

which the on-site energy of the two TIs are different: $H_{Efield} = \begin{pmatrix} TI_1 - V(z) & \Delta \\ \Delta^\dagger & TI_2 + V(z) \end{pmatrix}$. The spintexture of two Dirac cones are opposite: Upper Dirac cone–left handed, lower Dirac cone-right handed and vice versa for bottom surface.

2.4 Quantum Anomalous Hall effect

Figure 2.15 demonstrates the experimental setup of Hall effects. For quantum Hall effect, the perpendicular magnetic field applying to 2DEG system leads to a Hall current around the edge of 2D slab. The Hall conductance is quantized due to Landau levels formation, thus increasing the magnetic field will cause plateaus of Hall conductance at exact value of magnetic field. In the Quantum Spin Hall Effect (QSHE), the two spins up and down are spatially separated and form a so called "spin current", without a magnetic field. The spontaneous magnetization of QAH automatically breaks TRS and opens a magnetic gap and dissipationless spin current is non spin dependence. [6]. The QAH experimental setup is similar to classical Hall effect where the voltage is applied in longitudinal direction with a current flows in perpendicular direction. The only difference is that in QAH experiment is required to align the magnetic ordering in desired direction.

Quantized Hall conductivity

We computed the Chern number to determine the band structure topology for different exchange energy and three magnetic configurations. Since the sum in Eq.2.5 is over the first Brillouin zone, we choose an effective Brillouin zone for k·p model in a rectangle centred at the Γ with a cut off k-point . The main contribution of Berry curvature in the Kubo formula is at the vicinity of the Γ

[6] We have to distinguish "magnetic gap" and "tunnelling gap" which is caused by two surface coupling

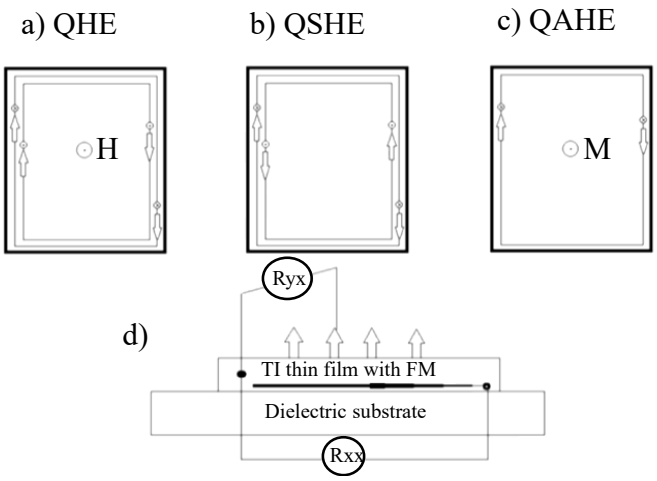

Figure 2.15: Currents flow with spin directions in Hall effects. (a) Quantum Hall effect, (b) Quantum spin Hall effect, (c) Quantum Anomalous Hall effect, (d) Basic experimental setup of QAHE

point. Thus, Berry curvature shows a peak at the Γ point at TPT. As can be seen from 2.16, the Chern number is exactly quantized when varying the exchange energy for all three magnetic configurations at T=0K. Before phase transition, the exchange energy is not sufficient to close the band gap, the Chern number is zero. The Berry curvature drops to a negative minimum value at the Γ point ($k < k_0 = \sqrt{m_2(M_z + d)}$), positive value of the Berry curvature around the first Brillouin zone border makes the total Chern number zero. [7] If the exchange energy is strong enough to close the band gap and reopen it, the phase transformed to non-trivial QAH phase with Chern number 1 at T=0K. Interestingly, the TPT happens at exact critical point where the band gap reached minimum value. Comparing three different magnetic configurations, we confirmed that the critical exchange energy at which the Chern number becomes 1 is smallest for the whole slab doping case, followed by sandwiching the slab between two ferromagnetic layers. Thus, in the whole slab doping the critical exchange energy is smallest compared to the two other cases. This fact may help to define the critical ferromagnetic doping concentration, and make a reliable experimental structure for QAH. The temperature dependence Hall conductivity is also

[7] Although the band gap is small but it is still exists, so the TI phase is still connected to trivial insulating phase

considered when varying the exchange field.

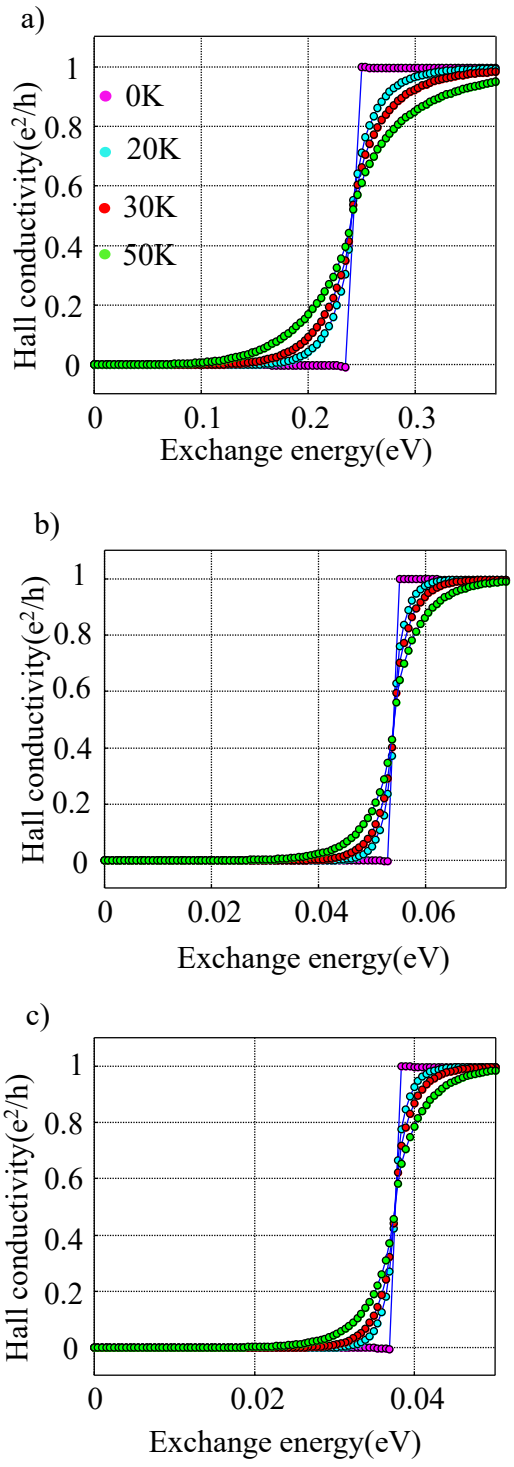

Figure 2.16: Hall conductivity as a function of exchange energy, temperature 0K, 20K, 30K, 50K for different doping possibilities. The quantization is survived under zero temperature only: (a) one substrate induced magnetic ordering, (b) two substrate induced magnetic ordering, (c) whole slab doping

Hence, we have presented our main results of topological phase transition

of topological insulator in the proximity to the ferromagnetism effect. By taking into the consideration the exchange coupling, our model with Rashba based spin-orbit coupling and interlayer tunnelling have shown exact quantized anomalous Hall states for three magnetic structure. However, the effect of thermal fluctuation or chemical potential variation can change the Hall quantization. In the next sub-section, we will give more insightful discussion of temperature dependence Hall conductivity. We note that the Hall conductivity becomes negative at -0.25eV, but there is no phase transition occurs.

Temperature-dependence Hall Conductivity

The QAH under non-zero temperature and chemical potential gating-modulated is considered when the exchange energy is sufficient for QAH. As can be seen from the Figure 2.17, the Hall conductivity inside the magnetic gap at zero temperature is quantized in unit of $\frac{e^2}{h}$ due to the Chern number quantization for all three magnetic cases. The drop in Hall conductivity is also obtained before phase transition indicating that total Berry curvature falls down due to the change in occupation number of highest valence band at Dirac cone region. The "jump" of Hall conductance under non-zero temperature is smooth, not showing a quantized behaviour. Under large exchange field and zero temperature, the Fermi-Dirac distribution function is either 0 or 1 for the states below and above Fermi level (The Fermi level is in the middle of the band gap). When the temperature increase to 20, 30K the Hall conductivity decreases as an effect of Fermi-Dirac distribution function. We note that Molecular Beam Epitaxy (MBE)-grown Bi_2Se_3 may contain a few impurities, or the experimental condition is under Fermi-level being gating-modulated. Thus, the Hall conductivity: decreases to 0 when the Fermi level is below the two Dirac cones (conductor), jumps to 1 when the Fermi level is inside the band gap, drops to 0 when the Fermi level is above the two Dirac cones (insulating phase). When the temperature increase,

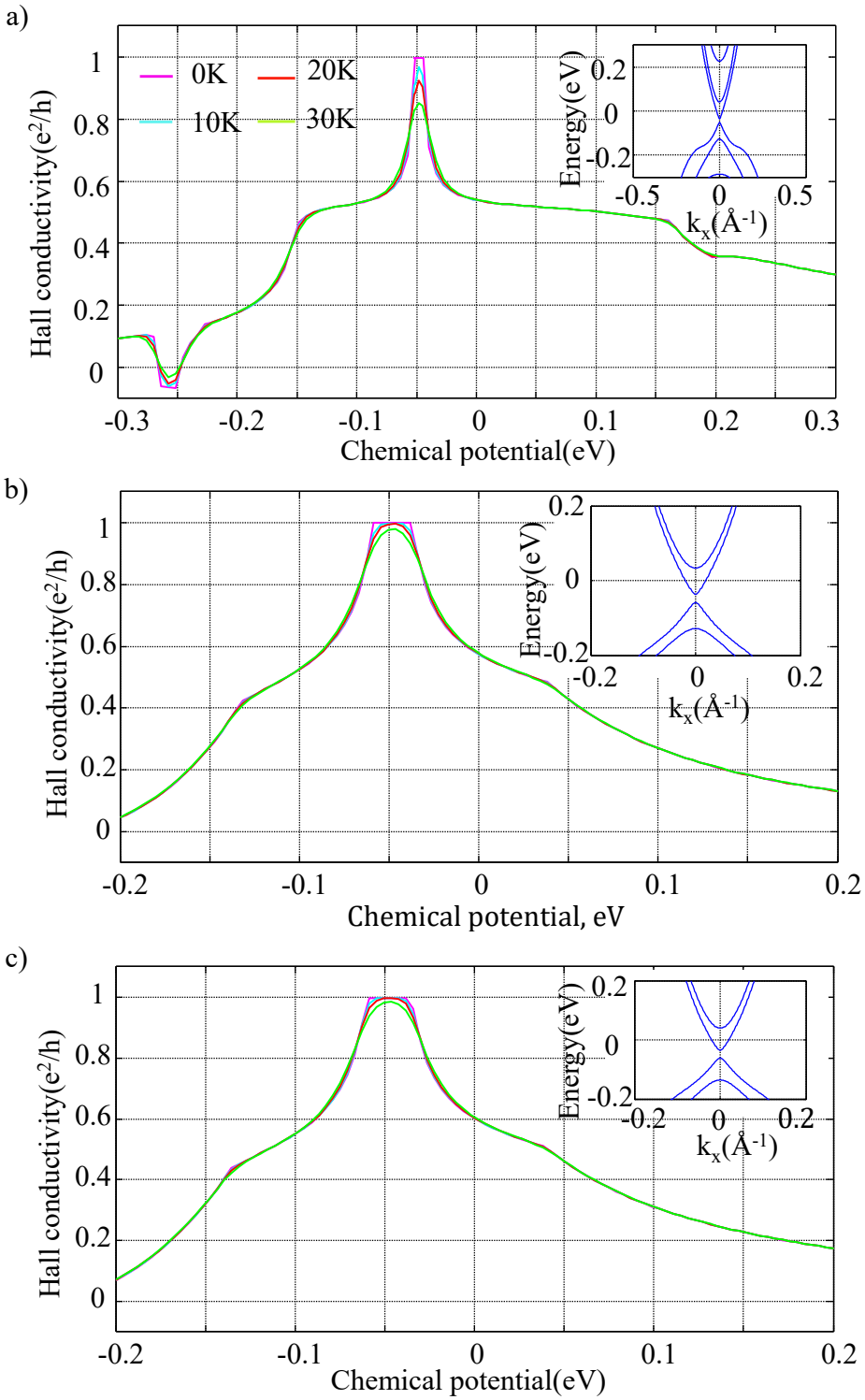

Figure 2.17: Temperature dependence Hall conductivity 0K, 10K, 20K, 30K for: (a) one substrate induced magnetism, (b) two substrate induced magnetism, (c) whole slab doping

the electrons with kinetics energy are able to move along the edge of TI material. Thus, we observed slightly above nonzero Hall conductivity in conducting and insulating phases. In QAH phase (the Fermi level is in the band gap), the electrons transverse in perpendicular direction with respect to the voltage applied experienced collision with other electrons. Hence, the Hall conductance is less than $\frac{e^2}{h}$ for the QAH phase. When sandwiching TI material with two ferromagnetic layers and doping the Ferromagnet (FM) on all layer, the Hall conductivity shows less dependence on temperature i.e., σ_{xy} decreases insignificantly when temperature slightly increases. σ_{xy} is more consistent for the whole slab doping case where the magnetic gap is large i.e., when T=10K the Hall conductivity is almost the same compared to the zero temperature case.

2.5 Conclusion

We provided an overview of realistic model for ultra-thin topological insulator films. From two dimensional spin-orbit coupled electron gas model we developed the magnetic multi-band k·p model which involves both spin degeneracy and surface interaction. The work has confirmed that the stacked quintuple model successfully captures the electronic properties of magnetic TI compared to first principle calculation and ARPES measurement. Remarkably, the main theoretical finding of this chapter is the TPT mechanism driven by magnetic impurities for three experimental realizable magnetic structure mentioned above (FM-TI, FM-TI-FM, magnetically doped TI). The key issue is that the interaction between two surfaces of TI never vanishes unless the slab is infinite. Moreover, the critical phase transition exchange field is found to balance the intersurfaces tunnelling energy. The topological phase transition is a result of band exchange and confirmed by the Thouless-Kohmoto-Nightigale-Nijs (TKNN)) invariance or the first Chern number. Hence, the Hall conductivity is nonzero under suf-

ficient out-of plane exchange field, enabling dissipationless charge current in spintronics devices. One key contribution of the study is that the skyrmion spin flip pattern is predicted for FM-TI structure when the inversion symmetry is broken. The previous experimental work has confirmed a hedgehodge spin pattern of the valence bands of magnetically doped TI. As an extension of this field, our study suggests that the spin-ARPES measurement can examine higher energy bands to observe the spin-flip pattern in momentum space. However, in experimental condition the Hall conductivity is no longer quantized in unit of $\frac{e^2}{h}$ due to the effect of temperature fluctuation. Moreover, the non-quantized Hall conductivity with Fermi level being gating modulated. Our proposal simplified the computational complexity of magnetically doped crystal Bi_2Se_3, thus novel broken symmetry topological phases can be tuned on more straightforwardly. For example, Chern number 2 is expected under super-high exchange energy if we maintain the system to be insulating.

We investigated ultra-thin TI slab with various thicknesses which requires a computational approach, complemented by an analytical result. Hence, the analytical work which was done for a four-band model with magnetic exchange field nicely explains all the calculation results of momentum dependence Berry curvature evolution, spin-flip pattern and critical momentum. A higher order analytical calculation for thin film of higher thickness could be a possible way to explain the transition mechanism of Z_2 TI. However, the analytical results could not be performed for larger Hamiltonian. We expect that the topological phase transition point is almost identical for other QLs with different thicknesses since the phase transition is mainly on the two surfaces.

This page was intentionally left blank.

Chapter 3

Multiple topological phase transition $BiTl(S_{1-\delta}Se_{\delta})_2$

3.1 $BiTl(S_{1-\delta}Se_{\delta})_2$ as a topological insulator

There is a growing body of literature that recognises the importance of $TlBi(S_{1-\delta}Se_{\delta})_2$ (δ–doping level) as a first tunable analoque of Bi_2Se_3 [45]. Different composition of sulfur gives rise to a topological surface state like in Bi_2Se_3 or a simple insulating thin film. As presented in experiments, the Dirac cone starts appearing in Angle Resolved Photo-emission Spectroscopy (ARPES) at the critical concentration $\delta = 0.4$ [45], whereas lower doping only gives a normal insulator. The emergence of the surface state is also confirmed by the enhancement of the spectral weight in ARPES measurement, i.e the signal comes from surface is dominant in the Dirac cone region. Figure 3.1 demonstrates experimental measurement of energy momentum dispersion in $BiTl(S_{1-\delta}Se_{\delta})_2$, showing a phase transition from trivial insulator to TI with spintexture as a function of doping.

The proposal of high Chern number in TI is for the Bi_2Se_3 class using extended Haldane model [27]. As mentioned in the last chapter, the high Chern number Quantum Anomalous Hall (QAH) in Bi_2Se_3 is hard to realize when the high exchange field can envole more bands at low energy spectra and difficult to

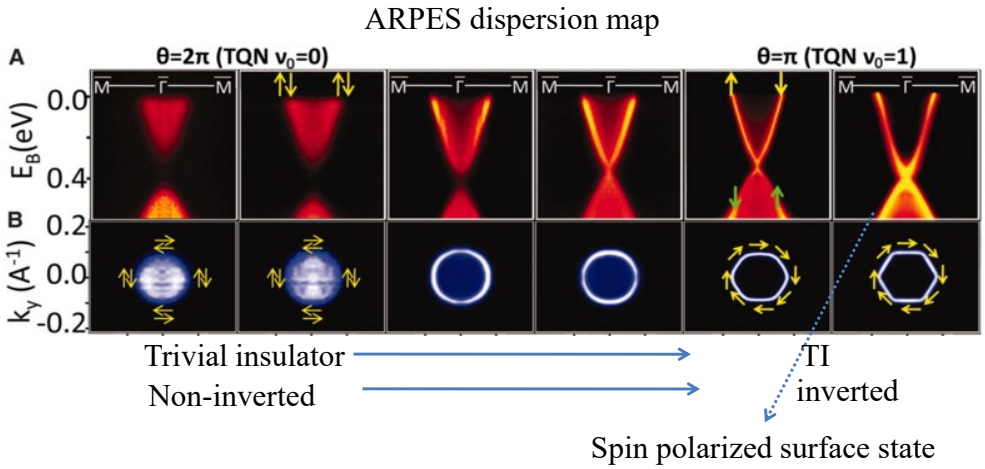

Figure 3.1: First rows: ARPES dispersion map of tunable $BiTl(S_{1-\delta}Se_{\delta})_2$ as a function of doping level δ. Second rows: constant energy contour with the spin directions defined (labels). Experimental data taken from Ref. [45]

maintain insulating state. The basics physics is multiple band inversion when the magnetic exchange field overcomes the bulk band gap, generating second bulk band inversion [24, 27, 46]. However, for Bi_2X_3 the bulk band gap is fixed and it is quite difficult to control the necessary exchange field to a large value. Up to now, the QAH experiment can detect the Hall conductivity with Chern number up to 1 [27, 47]. This is because the limitation of the band gap, and the magnetization in the system. A small shift in the Fermi level can even change the Hall conductivity and loose the quantization. Hence, a new material class with more tunable properties is needed to achieve more roburst Quantum Anomalous Hall (QAH) insulating state. Several questions have appeared since the QAH has been realized experimentally. What is the best way to get high ferromagnetic ordering? What materials to looks at to get a stable QAHI? And what are the additional parameters can be tuned except for the out of plane exchange field? This chapter also presents the work published in [48].

In order to answer the aforementioned questions, we study the practicability of achieving Quantum Anomalous Hall Effect (QAHE) with field-tunable Chern number in a magnetically doped, topologically trivial insulating thin film. We demonstrate that the QAH phases with different Chern numbers can

be achieved for $TlBi(S_{1-\delta}Se_{\delta})_2$, by means of tuning the exchange field strength or the sample thickness near the Z_2 topological critical point. Our physics scenario successfully reduces the necessary exchange coupling strength for a targeted Chern number. This QAH mechanism differs from the traditional QAH picture with a magnetic topological insulating thin film, where the "surface" states must involve and sometimes complicate the realization issue. Furthermore, we find that a given Chern number can also be tuned by a perpendicular electric field, which naturally occurs when a substrate is present.

This chapter provides an alternative route to achieve QAHI, compared to the previous studies [24, 27, 49], to achieve a high Chern number QAHI. We show the feasibility of exhibiting QAHE with field-tunable Chern number in a magnetically doped, topologically trivial insulating thin film, in proximity to the Z_2 topological critical point [50]. Specifically, we will focus on a candidate compound, $TlBi(S_{1-\delta}Se_{\delta})_2$, for its tunable property from a trivial insulator to an non-trivial one by changing the chemical composition [51]. Although the microscopic mechanism to realize the QAH phases is still the same as the magnetically doped TIs, our scenario further offers a few attractive features to achieve a higher Chern number: (1) Making the system close to the Z_2 critical point lowers the threshold value of the exchange field to induce the high order spin-polarized band inversion; This feature is distinguished from the high Chern number in thin film of magnetic TIs, where the first Chern number could be achieved when the exchange fields compensate the tunnelling band gap. Meanwhile, the higher Chern number QAH effect is more difficult to achieve when the exchange field should overcome the bulk band gap [50]. (2) we start with a trivially insulating thin film, in sharp contrast to previous studies. As a result, all 2D-like subbands have bulk nature and it has advantages to avoid the treatment for the sample surfaces, usually exposed to complex environment; (3) we also suggest an implementation of the potential gradient or the dielectric substrate to reduce the critical value of the exchange field. This has not yet been explored in previous

related studies. Therefore, in brief, our work strongly suggests that the trivial insulating thin film with sufficiently large SOC can provide a unique platform to exhibit QAHE with high Chern number.

The parameter specific model for $TlBi(S_{1-\delta}Se_{\delta})_2$ in the trivial side is close to the Z_2 phase transition critical points. We have m=0.0625eV^{-1}Å^{-2}; m_2=-0.04eV^{-1}Å^{-2}; $d = -0.22$ eV, $v = 2.5$ eV·Å; $t_z = 0.2$eV. [52] By increasing t_z, we can obtain a nontrivial Z_2 topological insulator phase. This model has been used to describe the Topological Phase Transition (TPT) in $TlBi(S_{1-\delta}Se_{\delta})_2$ and delivered the spin-polarized surface related states both in the trivial and the nontrivial region in good agreement with recent spin- and angle-resolved photoemission measurements. [52]

3.2 Topological phase transition: From trivial to non-trivial insulators

It would be helpful to begin with a warm-up example to demonstrate how the effective model can be driven into a non-trivial Z_2 insulators by tuning the parameter t_z which is related to the lattice constants and the size of atomic orbitals in general. For concreteness, we adapt the parameters mentioned above which are fitted to band structures of $TlBi(S_{1-\delta}Se_{\delta})_2$ [52]. However, it is worth mentioning that this model is also applicable for the other Bi_2X_3 compounds. [43]

The typical energy spectra around Γ point for Z_2 trivial and non-trivial thin films are shown in Figs. 3.2(a) and (b), respectively. Without breaking both TRS and IS, each band in the spectra is obviously spin degenerated and thus has a zero expectation value for the net spin polarization. By defining E_g as the energy gap between the lowest conduction band and the highest valence band at Γ point in the thin film, and Δ_i as the gap between ith lowest conduction band and $i+1$th lowest one, on the trivial insulator side, we find that E_g is typically

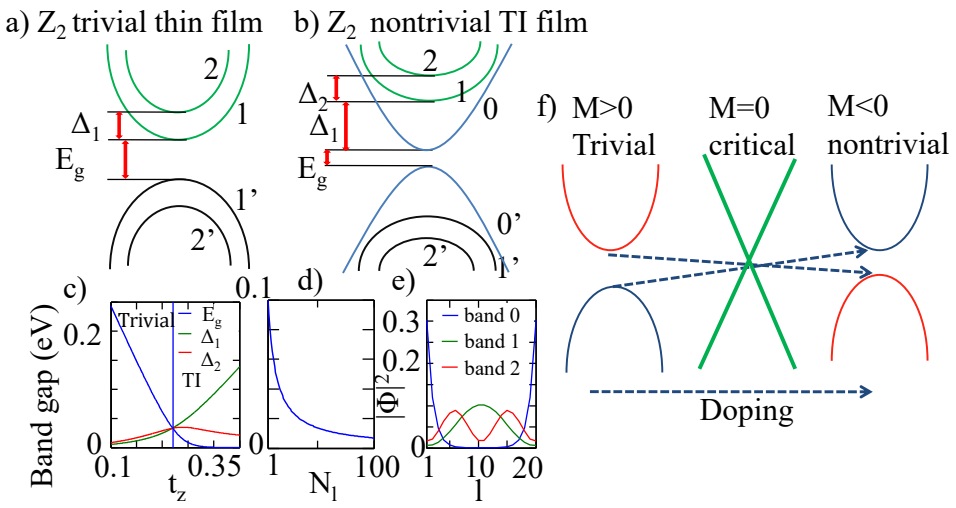

Figure 3.2: The schematic energy spectra of the thin film model around Γ point from a trivial insulator (a) to a Z_2 TI (b) with two types of energy scales: the system band gap E_g and the energy difference between neighboring bandstructure. The positive integer numbers without (with) prime denote conduction (valence) bands. "0" and "0′" denote bands with surface nature. (c) The calculated E_g and i as a function of t_z. t_{zc} is found to be 0.22 eV here. (d) The band gap E_g of the thin film at $t_z = t_{zc}$ as a function of the number of layers N_l. (e) The wave function distribution $|\Phi|^2$ at Γ point as a function of l for the lowest three conduction bands in an $N_l = 20$, Z_2 TI thin film with $t_z = 0.23$ eV (l is the layer index). Other numerical parameters are given in the main text. (f) Z_2 topological phase transition of the bulk band, M is the mass term. M>0 – trivial band gap. M=0 – critical, gap closing. M<0 – non-trivial, band gap inverted.

larger than Δ_i, while among Δ_i they are comparable, as a result of all quantum well states.

The aforementioned feature can be changed via chemical (Se) doping, or effectively, increase the tunnelling energy t_z. Close to a "critical" value of t_z (called t_{zc}, at which the 3D bulk band gap closes, independent of the thickness of the thin films), E_g becomes comparable to Δ_1 and turns into a smaller value rapidly after passing t_{zc}, as can be seen in Figs. 3.2(b) and (c). This crossover phenomenon between the values of E_g and Δ_1 marks a TPT: From a thin film of trivial insulator to a thin film of a Z_2 topological insulator. The latter phase is sharply identified by the presence of the surface states, a consequence of the band inversion, with Dirac-like energy dispersion [see the band labelled by "0" and "0′" in Figure 3.2(b)]. Note that the surface states are distinct from the usual quantum well (bulk) states, because their wave functions would be almost lo-

calized at either the top or the bottom layer, as compared in Figure 3.2(e) by showing wave function distribution $|\Phi|^2$ as a function of the layer index l. A phase diagram which tunable parameter t_z (doping) is presented in Figure 3.2(c) with corresponding band gap E_g, quantum well gaps Δ_1, Δ_2. The Z_2 TPT occurs when the bulk band gap closes. Hence, the band gap of thin film is comparable with the gap of quantum well states, contributed totally by the interlayer tunnelling term. With doping, we can flexibly control the thin film band gap and the quantum well gaps. There are a few things in the TI regime worth mentioning here. Firstly, when $t_z > t_{zc}$, it is understood that the massiveness of the Dirac spectrum for the surface states is due to the tunneling barrier (or inevitable wave function overlapping between boundaries), that is, with a relatively small t_z (but still $> t_{zc}$), in thin films. Secondly, similar to the usual case for growing Bi_2Se_3 thin films [44], the Dirac mass can be reduced to zero by increasing the number of layers N_l to a t_z-dependent threshold value N_{lc}. For instance, as t_z approaches to t_{zc} from above, the energy gap is closed only when N_{lc} goes to infinity in the true 3D limit [see Figure 3.2(d)]. Finally, it is quite important to notice that typically $E_g < \Delta_2 < \Delta_1$ for TIs, while near $t_z \sim t_{zc}$ even on the trivial insulating side, these energy scales are all comparable with each other. Figure 3.2(f) shows a schematic bulk band as function of doping where the Z_2 phase transition is captured. There a three regimes with mass term: M>0 trivial, M=0 critical, and M>0 non-trivial. This is the key observation of our proposed scenario for realizing QAHE with field-tunable Chern number, as we will explain below.

3.3 Quantum Anomalous Hall Effect from trivial insulating thin films

In this section, we demonstrate how the QAHE with field-tunable Chern number can be achieved theoretically through our scenario. As shown schematically

in Figure 3.3(a), the TlBi($S_{1-\delta}Se_\delta$)$_2$ thin film, growing on a substrate, on the trivial insulating side with $t_z \sim t_{zc}$ (doping-tunable) is taken to be our prototype sample. During the process toward QAHE, we also assume that certain magnetic dopant can be distributed homogeneously over the whole sample and are ferromagnetically ordered to provide the necessary exchange field. In the presence of the exchange field, the core concept to exhibit QAHE is simply from the band inversion phenomenon occurred between pairs of the conduction and valence bands with different spin polarizations. Figs. 3.3(b) and (c) schematically show one pair of the bands inverted (thus with Chern number $C = 1$) and two pairs inverted (with Chern number $C = 2$), respectively. After band inversion, each band forms a skyrmion-like spin texture around Γ point in momentum space, leading to non-vanishing Chern number. In addition, in order to achieve the QAH phase with even higher Chern number, more pairs of the band inversions are needed. According to the comparison among various energy scales in the previous section, with a given strength of the exchange field M_z, our focus on the trivial side near t_{zc} would more likely arrive at a phase with high C.

3.4 Exchange field tunable Quantum Anomalous Hall Effect

We now show the band structure evolution around Γ point as a function of M_z for a TlBi($S_{1-\delta}Se_\delta$)$_2$ thin film with $N_l = 6$ in Figure 3.4. When the warping effect is relatively small, such as in TlBi($S_{1-\delta}Se_\delta$)$_2$, applying M_z is the only effective way to make bands magnetically inverted; when the warping effect is large, such as in Bi_2Te_3, one may also apply in-plane magnetization along certain direction to induce QAH phase. Fermi level E_F is always set at zero energy and the labels $i = 1, 2$ ($i = 1', 2'$) denote the ith lowest (highest) conduction (valence) bands, in the absence of M_z, with spin-up and spin-down shown in different colors.

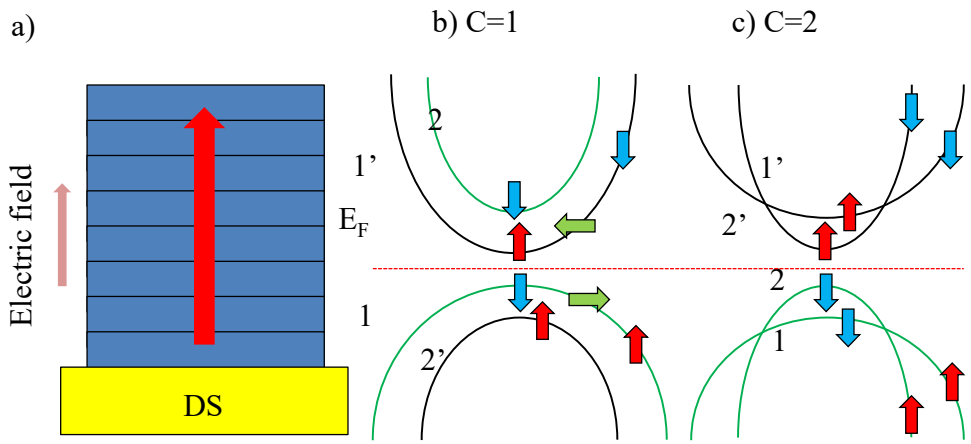

Figure 3.3: The left panel (a) schematically shows our proposed scenario to achieve the field-tunable QAHE: Let layered $TlBi(S_{1-\delta}Se_{\delta})_2$ thin film with ferromagnetic order be grown on a substrate, which provides an electric potential along z direction. The right panel, (b) and (c), shows schematic band structures, spin-texture ("skyrmion"-like), and band-inversion with suitable band labels for $C = 1$ and $C = 2$ QAH phases, respectively, at $t_z < t_{zc}$. (a) Proposed $TlBi(S_{1-\delta}Se_{\delta})_2$ grown on substrate with spontaneous magnetization combined with electric potential along c-axis. (b)-(c) Reflection symmetric (E = 0 eV) band structure as a function of exchange field (four bands model). (a) QAH phase with $C = 1$ of magnetic trivial thin film with "skyrmion" spin pattern (b) The band-structure folding number $C = 2$ when two other quantum well states change the particle hole characteristic. The $U(1)$ charge symmetry still conserves.

Starting with $M_z = 0$, each band is spin-degenerate and the system is in the $C = 0$ (trivial) phase (The model we use here is different from the one in previous chapter with another interlayer tunneling terms). Increasing M_z causes spin splitting, which shifts the bands with spin-up and spin-down polarizations in opposite directions with respect to E_F, and hence reduces E_g [Figure 3.4(b)]. As M_z reaches M_{c1}, the energy gap is closing with vanishing out-of-plane spin moment at the touching point [Figure 3.4(c)]. Further increasing M_z reopens the gap again, forms skyrmion-like spin texture, and indicates a TPT due to band inversion from $C = 0$ trivial phase to $C = 1$ QAHE [Figure 3.4(d)]. We note that now the band labeled "1" and "1′" are switched. As $M_z = M_{x1}$, the band "2" ("2′") meets with "1′" ("1") [Figure 3.2(e)] and the band "2" with spin-down and "2′" with spin-up become prominent near E_F if M_z continues increasing until

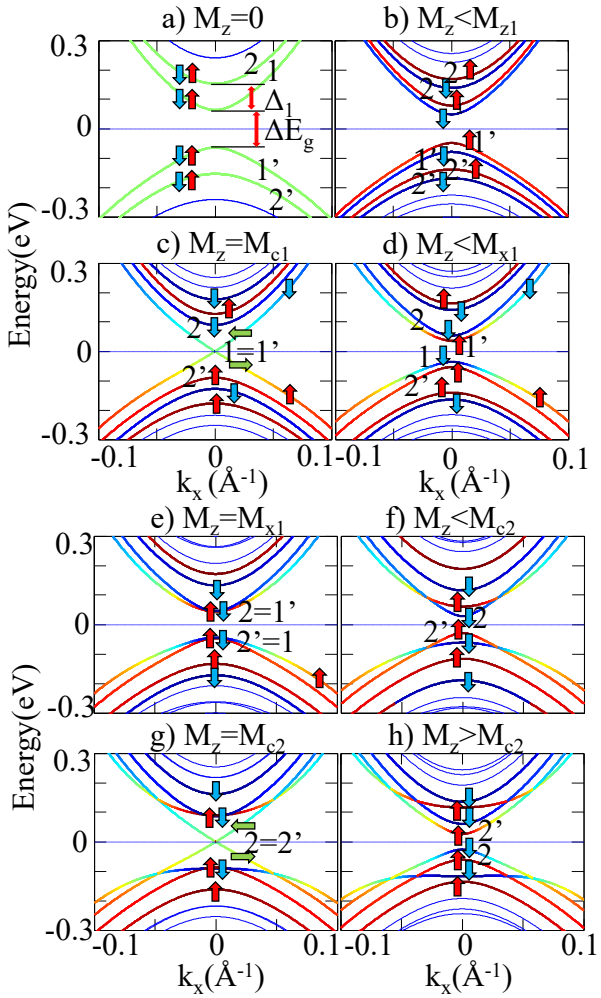

Figure 3.4: Evolution of the sub-band structure at $t_z = 0.2$ eV and $N_l = 6$ around Γ point upon increasing exchange field M_z. The band labels are used as usual. Additionally, the color dressing in each band represents the momentum-dependent, out-of-the-plane spin polarization with arrows indicating the main spin-polarized component. (a) $M_z = 0$; (b) $0 < M_z < M_{c1}$ before first TPT; (c) $M_z = M_{c1}$, where the gap closes at the first time; (d) $M_{c1} < M_z < M_{x1}$ in the QAH phase with $C = 1$; (e) $M_z = M_{x1}$, where two lowest conduction bands meet; (f) $M_{x1} < M_z < M_{c2}$ and the system approaches second band inversion; (g) $M_z = M_{c2}$ at another critical point; (f) $M_z > M_{c2}$, where the second TPT occurs, and the system enters QAH state with $C = 2$.

$M_z = M_{c2}$ [Figure 3.4(f)]. At $M_z = M_{c2}$, the gap is closing [Figure 3.4(g)] and implies a second TPT, which adds the Chern number by one and hence $C = 2$ after the gap-reopening as $M_z > M_{c2}$ [Figure 3.4(h)]. The fashion shown here is in fact quite similar to some previous proposals for getting the QAHE with high Chern number in the TI thin film regime. [24, 27, 49]

3.5 Toward higher Chern number

The model simulation and discussion in the previous subsection give us a clear physical picture of our mechanism to obtain high Chern number. Given sufficiently large exchange field, the band gap can close and reopen multiple times due to the presence of relatively intensive 2D subbands (quantum well states), which is a consequence of a trivial insulating sample with (nearly) critical Se-doping.

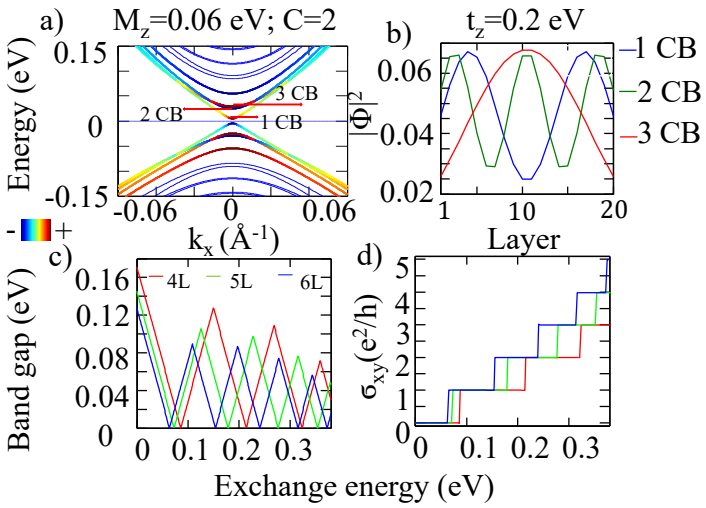

Figure 3.5: (a) Band structure of the QAH phase with $C = 2$ in the thick film limit, $N_l = 20$; ($M_z = 0.06$ eV) and the color dressing is used for spin polarizations. (b) The corresponding wave function distributions of the three lowest conduction bands at the Γ point as a function of layer index l. (c) and (d) show the band gap evolution and the quantized Hall conductivity, respectively, as a function of M_z for the given $N_l = 4, 5, 6$ cases. All plots here use $t_z = 0.2$ eV.

This mechanism is completely based on the "twist" of the spin-polarized bulk states in the quasi-2D system. Thus, it is distinctive from the original proposal, where the QAHE is achieved by gapping out the surface Dirac cones in 3D TIs [53, 54]. To see this, we first present energy spectrum around Γ point and the corresponding spin texture for $C = 2$ QAH state with $N_l = 20$, i.e., in the thick film limit [see Figure 3.5(a)]. The initially lowest, spin-down polarized conduction band now becomes the third highest valence band, indicating that the spin-polarized bands inverted twice. To explain the underlying physics, from the wave function distribution as a function of l in Figure 3.2(b), the first

three lowest conduction bands all have bulk nature. Similar properties are also found for the other bands. Such a feature results in a subtle but important difference from previous studies [24, 27, 49], because in our case no surface bands are involved in the whole process. As we will consider later, this might affect the real experiments in which each sample is usually grown on certain substrate.

To invert more spin-polarized bulk bands, our mechanism suggests at least two ways: 1) Apply large exchange field on the sample, and 2) increase the thickness of the sample. In Figs. 3.5(c) and (d), we explicitly calculate the band gap and the Hall conductivity as a function of M_z, respectively. The gap closes and reopens multiple times with the presence of the corresponding quantized plateaus in σ_{xy}, indicating a rich phase diagram of the QAH system. The Chern number increases in one integer step when M_z increases, a similar trend compared with the usual quantum Hall system. In addition, in the same figures by using different colors we also present both quantities with different number of layers. Clearly, for a thicker film with a given M_z, it is more likely to end up with a higher Chern number insulator due to the shrinking of Δ_i, which is inversely proportional to N_l.

From recent experiments in magnetic topological insulators such as Cr or Fe doped (Bi, Sb)$_2$Te$_3$, people observed that these magnetic dopants can be ferromagnetically ordered at temperature of order 100 K. The corresponding effective exchange field strength M_z can be estimated as large as 0.2eV with 10% doping [24, 55] and thus strongly indicates the feasibility of our scenario. To roughly estimate what the largest Chern number could be achieved, one can simply count how many quantum well states (subbands), labeled x, are able to be inverted by applying M_z. By noticing that $E_g \sim \Delta_i \sim 0.035$ eV in Figure 3.2(c) with $N_l = 20$, the number can be estimated through the following formula, $x = [(M_z - 0.0175)/0.035 + 1]$, where $[\cdots]$ denotes a floor function. Inserting the value of $M_z \approx 0.2$ into the formula yields $x = 6$, i.e., the largest $C = 6$ in this case. In addition, the energy range for this QAH phase to be stable

could be as large as 0.035 eV, above room temperature.

3.6 Electric field tunable QAHE

One of the practical issues, based on the mechanism we have mentioned above, is the presence of certain substrates when preparing the thin films epitaxially in the experiments (we have also mentioned in Chapter 2). It is equivalent to the presence of an effective electric field 'E_z' along z direction and this leads to a broken $z \to -z$ reflection symmetry for the thin films. Hence, we study systematically the effect of the electric field by adding a given linear potential term along z direction, with potentials $\mp E_z$ on the top and bottom surfaces of the sample, respectively, in Eq.(2.2) under various applied M_z. Note that the dispersion relation does not change if E_z changes sign.

We first consider the evolution of the energy spectrum near Γ point as a function of M_z with $E_z = -0.05$eV, as shown in Figs. 3.6(a)-(d). In the absence of any exchange field, the electric field simply introduces Rashba type interactions into the system and consequently each spin-degenerate band now splits with the originally band minimum shifted away from Γ point, while the spin degeneracy still keeps intact at Γ point [see Figure 3.6(a)] [44]. Assuming $N_l = 2N$, it is worth noting that the wave function distribution of these lowest (highest) conduction (valence) bands around Γ point is mainly from the contributions of Nth and $N+1$th layers in the middle. This is in sharp contrast with the usual TI thin films (i.e., $t_z > t_{zc}$) , in which the lowest conduction (highest valence) band has the largest weight from the top and the bottom layers.

Upon turning on the exchange field, as one can see in Figure 3.6(b), all the spin-degenerate points of Rashba-like bands at Γ point open up gaps and the band gap of the system reduces to zero as M_z reaches to a critical value M_c [see Figure 3.6(c)]. Further increasing M_z results in a spin-polarized band inversion

and reopens the band gap, leading again to the QAH phase [see Figure 3.6(d)]. It is interesting to notice a few subtle differences from the case without E_z: 1) When $M_z = 0$ the band gap is smaller due to the shift of the conduction band minimum; 2) at $M_z = M_c$, the energy dispersion is non-linear and the spin texture around Γ point is relatively simple. Importantly, the above observations show that the critical exchange field strength is lowered and one can possibly achieve QAHE with high Chern number by tuning the electric field, as we explain next.

Figure 3.6 illustrates the band gap evolution as a function of M_z with a given electric field E_z in an $N_l = 20$ thin film. The band gap repeatedly closes and reopens, indicating that the system undergoes TPTs several times up to the QAH phase with high Chern number ($C = 3$ in our plot). Significantly, after considering several different values of E_z, we find that the critical exchange energies to achieve $C = 1$ and $C = 2$ phases, respectively, are less than the cases in the absence of the electric potential. To examine it more carefully, we take two representative initial phases in our system at $E_z = 0$, as indicated by the arrows shown in Figure 3.6(e): 1) a trivial $C = 0$ phase with fixed M_z=0.025 eV and 2) a $C = 1$ QAH phase with fixed M_z=0.055eV. Purposely, they are chosen just prior to QAH phases with $C = 1$ and $C = 2$ separately. We then compute the corresponding band gap as a function of E_z for each of them. As one can see in Figure 3.6(f), it is feasible to apply an external electric field to drive our focused system, namely, $TlBi(S_{1-\delta}Se_{\delta})_2$ thin film from an originally Chern number C QAH phase to another QAH phase with Chern number $C + 1$. However, we would like to point out that this tuning approach is efficient to obtain QAH phase up to $C = 2$. For getting higher Chern numbers, it might become unstable because several sub-bands would come into play around E_F and the system may not maintain its insulating nature during the process.

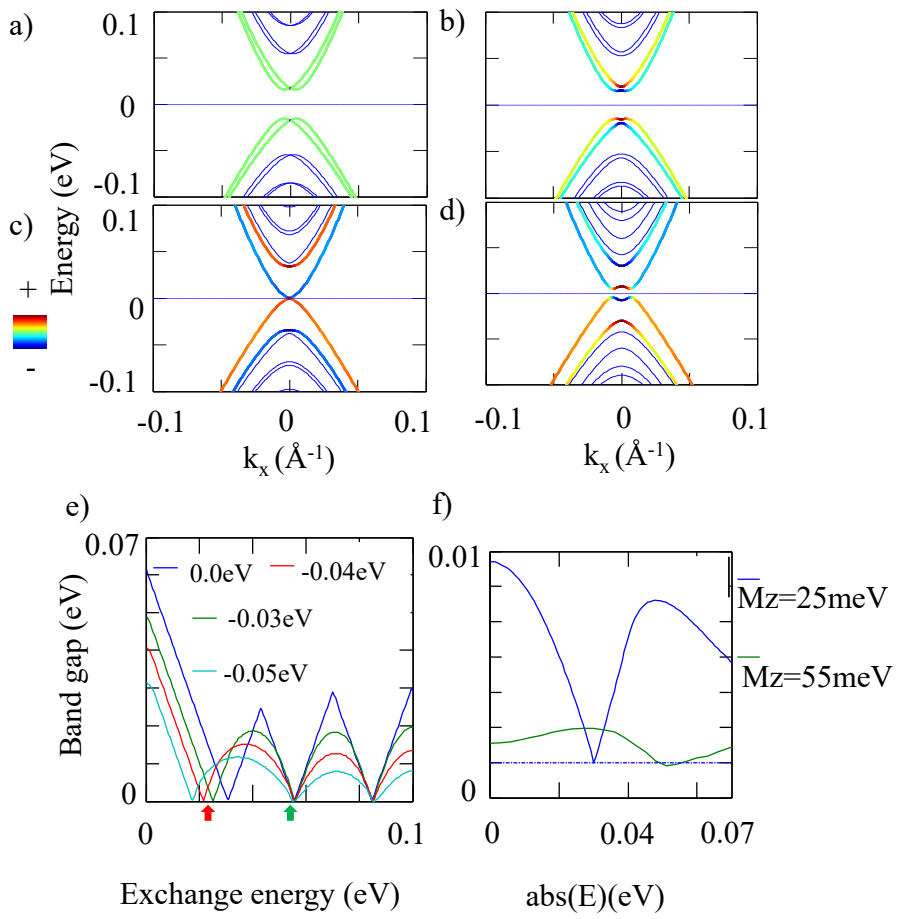

Figure 3.6: The evolution of the band structure upon increasing M_z with non-vanishing $E_z = -0.05$ eV: (a) $M_z = 0$; (b) $0 < M_z < M_c$; (c) $M_z = M_c$; (d) $M_z > M_c$, where the system turns to the $C = 1$ QAH phase. The degree of out-of-the-plane spin polarization is denoted by color. (e) The non-linear band gap evolution as a function of M_z with various electric field strength. Chern number C (starting from 0) is added by one each time when the gap closes. The arrows shown here are the chosen exchange field strength to be compared in (f). (f) Electric field tunable QAH phases for two given exchange field strength. The gap closing points separate the $C = 0$ and $C = 1$ phases (blue curve), and the $C = 1$ and $C = 2$ phases (green curve), respectively.

3.7 Conclusion

In summary, we have presented our scenario to achieve QAH effect with field-tunable Chern number via a model study. Remarkably, the model can describe topological phase transition from a Z_2 trivial to an non-trivial insulating thin film for realistic materials such as $TlBi(S_{1-\delta}Se_{\delta})_2$. By showing the band-structure evolution, spin-texture, and hence the spin polarized band inversion, we clearly

demonstrate the feasibility of our approach to tune the Chern numbers of the QAH phases through changing either the exchange field strength or the electric field strength in topologically trivial thin films near the Z_2 critical point (to TI phase). In particular, we stress that the necessary exchange field strength to exhibit high Chern number QAH effect can be reduced further when pushing the system closer to the critical point and combining with the benefit from the substrate.

This page was intentionally left blank.

Chapter 4

Quantum anomalous Hall effect in (001) thin films of topological crystalline insulators

4.1 Topological crystalline insulator

Recent trend in topological material field has lead to not only the Z_2 TI, but also to other classes of materials where crystall symmetry plays more important roles. In particular, the interests refer to tunable material class of previously known as spin Hall insulator PbTe [56] and similar structures like $Pb_{1-x}Sn_xTe$.

The rock-salt structure of semiconductors $Pb_{1-x}Sn_xX$ (X=Se/Te) are compounds of heavy atoms. Hence, the relativistic effect derived mainly from the spin-orbit coupling involves in the electronic properties of this material class. For example, the band gap of SnTe at L point is a result of relativistic effect, as well as mixing of states with different quasi-particle energies. It has been confirmed that the lowest conduction band and highest valence band derived mainly from 5p states on Sn and Te, respectively [57].

The crystal symmetry is special in the bulk Sn based structure like C_{4v} rotation symmetry and mirror symmetry. There would therefore seem to be definite

need for investigation of new phases. Hence, extending the symmetry classification of the crystal band-structure of SnTe/PbTe, the TCI has been discovered as a new phase of matter in which the combination of SOC, TRS and crystal symmetry give rise to new class of non–Time Reversal Invariance Momentum (TRIM) Dirac cones [28, 29]. The physics of band inversion in SnTe is similar to Bi_2Se_3 when each band carry orbital weight from p orbitals of different atoms that we mentioned above. By contrast, this feature is not presented in pristine PbTe where the bulk band gap is trivial. Figure 4.1.(a–b) (taken from Ref. [29]) represents difference in bulk band-structure properties at L point for SnTe (band inverted), and PbTe (trivial). The four Dirac cones at surface Brillouin zone are presented in Figure 4.1 with associating spin-texture. Moreover, TCI $Pb_{1-x}Sn_xX$ (X=Se/Te) [001] endows with many interesting properties like Quasi-particle Interference (QPI) map induced by four Fermi pockets of TCI surface state [32, 58], surface state spin texture [59], etc.

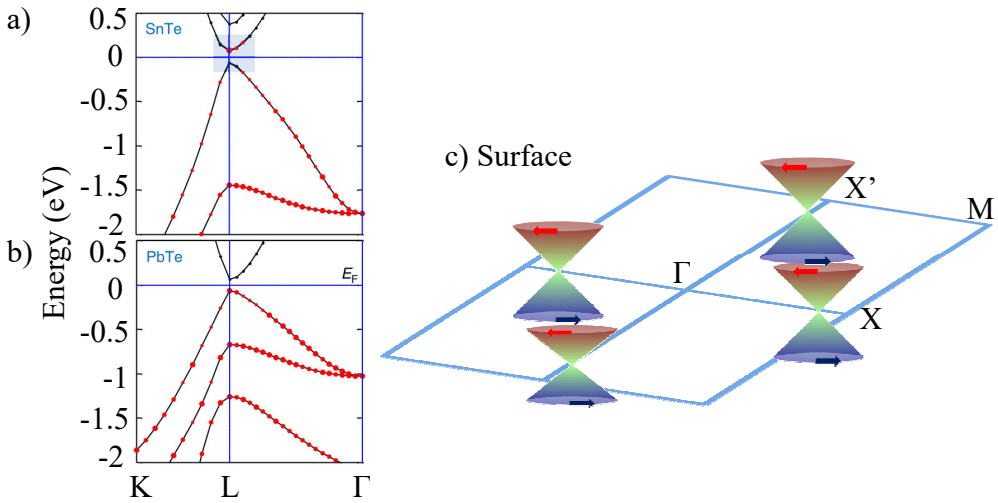

Figure 4.1: Figs. (a–b) taken from Ref. [29], red dots represent the orbital weight of Te atoms (a) Band inversion at L point for SnTe (b) Trivial gap at L point for PbTe (c) Four Dirac cones at surface Brillouin zone, the arrows indicate the spin directions.

Here, following the previous chapter we emphasize that there is active search for systems with a high Chern number ($C \geq 2$) due to both fundamental and application interests while the Chern number C is equal to the number of edge states. Especially, more dissipationless conducting channels may effectively re-

duce the contact resistence in the circuits, improving the performance of the low-power consumption devices. From this perspective, topological crystalline insulators (TCIs) that we mentioned above [32, 60] become a class of very promising materials with the following advantages: 1) Although a TCI, just like a 3D TI, has a bulk gap and topology-protected surface Dirac fermions, such a protection originates from crystalline symmetry (*e.g.*, mirror symmetry), instead of time-reversal symmetry [28, 29]. Consequently, a surface band gap can be made by applied strain or an electric field to break the crystalline symmetry without using an exchange field [61]. This not only endows the flexibility to control gap opening when designing electronic devices, but also enriches possible QAH physics in this material. 2) For a bulk TCI, the band inversion occurs even number of times in total, indicating that interest physics takes place in multiple low-energy regions in the Brillouin zone (*e.g.*, near four L points in SnTe). This gives way to achieve high Chern number QAH states via magnetic band inversion. Moreover, in $Pb_{1-x}Sn_x$(Se,Te), for instance, via chemical composition x it is possible to tune the system from trivial to non-trivial insulating state, or vice versa [62].

The magnetic TCI is predicted to exhibit QAH states with different Chern number levels [63]. Here, any Chern number between +4 and -4 can be obtained in TCI. Reference [63] only considered surface states which is located at non-time reversal invariance momentum. However, a problem with this approach is that a $\mathbf{k}\cdot\mathbf{p}$ model may not capture realistic electronic properties. Hence, this may fail to predict the exact topological phase diagram of TCI in film limit. By examining the evolution of the band structures upon increasing exchange field strength with associated orbital weight distribution and spin polarization, we find that various QAH states, in particular, with a high Chern number can be achieved. We emphasize that: (1) Our results strongly depend on the chemical composition, thickness, and certain symmetry breaking perturbations. Therefore, we suggest a best strategy to obtain an ultra-high Chern number ($C \geq 8$)

under TCI critical regime. (2) The key mechanism to QAH effect here is still a magnetic band inversion. However, it associates with certain unconventional process during band inversion, where the touching points are not located at time reversal invariance momenta. (3) We find the tunability between a trivial and a QAH phase via a rotated magnetization or an applied (or substrate-induced) perpendicular electric field, which has not yet been explored before. Therefore, our work would be a useful guideline for experiments to search for QAH physics on thin-film of magnetic TCI materials.

The chapter describes and discusses systematic methodology of tuning magnetic narrow gap IV-VI semiconductors from trivial and non-trivial to QAH phases with different chemical compositions. It begins with a description for a 3D tight-binding Hamiltonian of a face centred cubic lattice for the bulk and the thin film model of TCI [29]. We describe our method of introducing a small magnetic perturbation rotated in the real space and the potential gradient with an assumption that the potential within a slab of thin film is invariant. As convention, in the next session we propose a band-structure evolution as a function of the exchange field for odd and even number of layers, complemented with spin projection. Next, we present our numerical results of non-linear touching mechanism for thin film of IV-VI semiconductors near the TCI critical point. As a result of unconventional band inversion, new Van-Hove singularity emerges. We also show that the Berry curvature at the QAH phase is consistent with the VHs for $C = 4$ phase, whereas a second order band inversion also emerges at the TCI critical point. Finally, making use of the broken symmetry property of the substrate-induced electric field and magnetic rotation, we can tune the material to QAH phase with C=2. This chapter is also a summary of a paper [64].

4.2 Model and method

As mentioned in the introduction, rocksalt IV-VI semiconductor structures possess various kinds of symmetries including Time Reversal Symmetry (TRS), C_{4v} rotation symmetry and reflection symmetry. Figures 4.2(a–b) demonstrate cubic crystal structure of SnTe and surface Brillouin zone with associated high symmetry points, respectively. Moreover, the number of layers also decide the

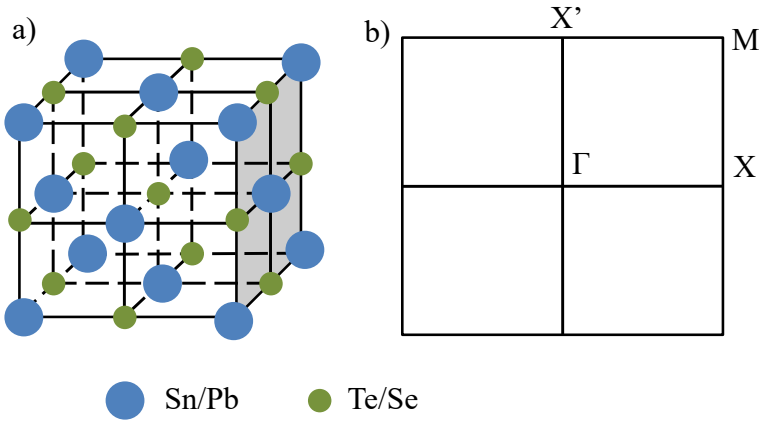

Figure 4.2: (a) Crystal structure of SnTe. (b) Surface Brillouin zone.

degeneracy at the high symmetry point X. These materials exhibit a special screw rotation symmetry (π-rotation plus a half Bravais lattice translation) along [110] or [$\bar{1}$10], *i.e.*, the direction of Pb–Pb bond) at the surface Brillouin zone for an even number of layers. Hence, each state at $(0, \pi)$ are fourfold degenerated by: time reversal symmetry and screw rotation symmetry [65]. The mirror eigenvalues are indistinguishable when the mirror operator commutes with the Hamiltonian: $[M, H] = 0$. However, the fourfold degeneracy at $(0, \pi)$ is broken for an odd number of layers with double TRS degenerated states. Here, we employed an unperturbed tight binding Hamiltonian for TCI thin film which was constructed from the bulk electronic structure of $Pb_{1-x}Sn_xX$ (X=Se,Te) based on p orbitals. The tight-binding model is constructed from the Wannier functions of the conduction and valence bands, which are p-orbitals of Sn and Te(Se) atoms.

This model was used to study the TCI with the mirror Chern number [29].

$$
\begin{aligned}
H_{tb} = & \, m \sum_{j} (-1)^{j} \sum_{\mathbf{r},\alpha} c^{\dagger}_{j\alpha}(\mathbf{r}) c_{j\alpha}(\mathbf{r}) \\
& + \sum_{j,j'} t_{jj'} \sum_{(\mathbf{r},\mathbf{r}'),\alpha} c^{\dagger}_{j\alpha}(\mathbf{r}) . \hat{d}_{\mathbf{r}\mathbf{r}'} \hat{d}_{\mathbf{r}\mathbf{r}'} . c_{j'\alpha}(\mathbf{r}') \\
& + h.c. + \sum_{j} i\lambda_{j} \sum_{\mathbf{r},\alpha,\beta} c^{\dagger}_{j\alpha}(\mathbf{r}) \times c_{j\beta}(\mathbf{r}) . s_{\alpha\beta} + \cdots ,
\end{aligned}
\tag{4.1}
$$

where the operator $c^{\dagger}_{j\alpha}(\mathbf{r})$ is a column vector with three components representing p_x, p_y, p_z orbitals, respectively, and creates either Sn ($j = 1$) or Te/Se ($j = 2$) fermion at site $\mathbf{r}$ of the rocksalt lattice [See Fig. 4.2(a)] with spin polarization α ($\uparrow, \downarrow$). m is the on-site potential difference between Sn and Te/Se. The second term of Eq. (4.2) represents σ-bond hoppings between the p-orbitals; denoting $\hat{d}_{\mathbf{r}\mathbf{r}'}$ the unit vector connecting sites $\mathbf{r}$ to $\mathbf{r}'$, $t_{12} = t_{21}$ represent the nearest-neighbour (NN) hoppings between Sn and Te/Se while t_{11} and t_{22} represent the next NN hoppings within separate sub-lattices. The third term includes atomic $\mathbf{L} \cdot \mathbf{s}$ spin-orbit coupling with coupling strength λ_j, where $\mathbf{L}$ is the angular momentum for p-orbitals and $\mathbf{s}$ are Pauli matrices for spin-1/2.

Taking periodic boundary conditions (BCs) along x and y directions and open BC along z ([001]) direction, the bulk and surface bands of above tight-binding model are now all projected onto a square (surface) first Brillouin zone (BZ). We note that the model parameters are chosen to best represent the first-principles calculation results. Depending on which material we study, additional terms such as π-bond hopping of the p-orbitals and the higher order neighbour hopping are added, as "$\cdots$" in Eq. (4.2) stands for. For the other Sn-substitution compounds ($0 < x < x_{max}$), the model parameters are obtained from the virtual crystal approximation, which usually provides an accurate description of the band inversion.

In parallel with our previous k·p model, we adapt a similar semi-infinite slab

model, except for higher order interlayer coupling term.

$$H = \sum_{p} \hat{H}_p C_p^{\dagger} C_p + \sum_{p,L} \hat{T}_L C_p^{\dagger} C_{p+L} + \sum_{p,L} \hat{T}_L{}^{\dagger} C_p C_{p+L}^{\dagger} \tag{4.2}$$

Where p represents the layer index, L is the distance index between two neighbouring layers. Considering the boundary conditions for layered materials, we adapt a semi-infinite slab model for [001] surface, except for higher order interlayer coupling term.

$$H = \begin{pmatrix} H_1 & T_1 & T_2 & \cdots & 0 \\ T_1^{\dagger} & H_2 & T_1 & \cdots & 0 \\ T_2^{\dagger} & T_1^{\dagger} & H_3 & \cdots & 0 \\ \vdots & \vdots & \vdots & \ddots & \vdots \\ 0 & \vdots & \vdots & \vdots & \vdots, \end{pmatrix} \tag{4.3}$$

The orbital basis is:

$$|Pb, p_{x,y,z}, \uparrow\rangle; |Te(Se), p_{x,y,z}, \uparrow\rangle; |Pb, p_{x,y,z}, \downarrow\rangle; |Te(Se), p_{x,y,z}, \downarrow\rangle,$$

Thus, each single layer of material is represented by a 12x12 Hamiltonian $H_i = H_p$,T_i are the i-th order nearest neighbour interlayer hoping matrices. The number of bands are linearly increased within the number of layers. Since we only consider the homogeneous magnetic doping, the magnetization takes effect over all layers and orbitals. When doping a thin film by magnetic elements, we assume the moments are homogeneous-ferromagnetically ordered, having a uniform exchange field $\mathbf{M} = (M_x, M_y, M_z)$ applied to the system. Thus, such an effect can be described by adding a Zeeman term to Eq. (4.2):

$$H_M = \sum_{\mathbf{r},j,\alpha\beta} \mathbf{M} \cdot \mathbf{s}_{\alpha\beta} c_{j\alpha}^{\dagger}(\mathbf{r}) c_{j\beta}(\mathbf{r}), \tag{4.4}$$

This term is the main driving force for our system to enter into QAH regime. $M = (M_x, M_y, M_z)$ are three components of the exchange field. In the case of

rotating a given magnetization $M = |\mathbf{M}|$ of the exchange field, it is usually more convenient to rewrite M in terms of spherical coordinates:

$$\mathbf{M} = M(\sin\theta\cos(\frac{\pi}{4}-\phi), \sin\theta\sin(\frac{\pi}{4}-\phi), \cos\theta),$$

The presence of $\frac{\pi}{4}$ phase difference in ϕ is due to the fact that the corresponding 'x' and 'y' directions from **k**-space are along [110] and [$\bar{1}$10], respectively. For later use, we also consider a perpendicular electric field applied to a thin film. Such effect can be described by adding a potential gradient along [001] direction with the assumption that in-plane potential in each layer is equal:

$$H_E = \sum_{\mathbf{r},j,\alpha} E(z) c^{\dagger}_{j\alpha}(\mathbf{r}) c_{j\alpha}(\mathbf{r}), \tag{4.5}$$

where the spatial coordinate z is viewed as the layer index and the potential $E(z)$ is proportional to z. This model gives four non-time reversal invariance Dirac cone along $\Gamma - X$ for the surface Brillouin zone of non-trivial TCI surface state.

4.3 Unconventional band touching

The following is a brief report on the possible QAH phase transition for trivial thin film and non-trivial TCI films. From a wide range of possible doping and structure combination, only some prominent features are presented. Starting from unperturbed Hamiltonian for trivial thin film, we slowly tune the parameter M_z, assuming that no in-plane magnetic components exist. In all the band-structure presented below, we compute the out-of-plane spin polarization for total slabs with the strength presented by colour map. Specifically, we show that when magnetically doping a trivial ($x < 0.2$) $Pb_{1-x}Sn_xSe$ insulating thin film, a QAH phase can be induced due to a simple mechanism: the magnetic

band inversion. Our scenario is in sharp constrast to the one proposed by Fang *et al.* [63], where only topology-protected surface states of a TCI are essential. Since the thin films with odd and even number of layers possess different symmetries which result in distinct behaviors, we discuss them separately below.

Figure 4.3 clearly distinguishes the sub-band evolution as a function of the out of plane exchange field for odd and even number of layers of a trivial thin films of pristine PbSe. In all two cases the broken TRS results in spin splitting inside the Brillouin zone. With different exchange energy scale, we first look at the

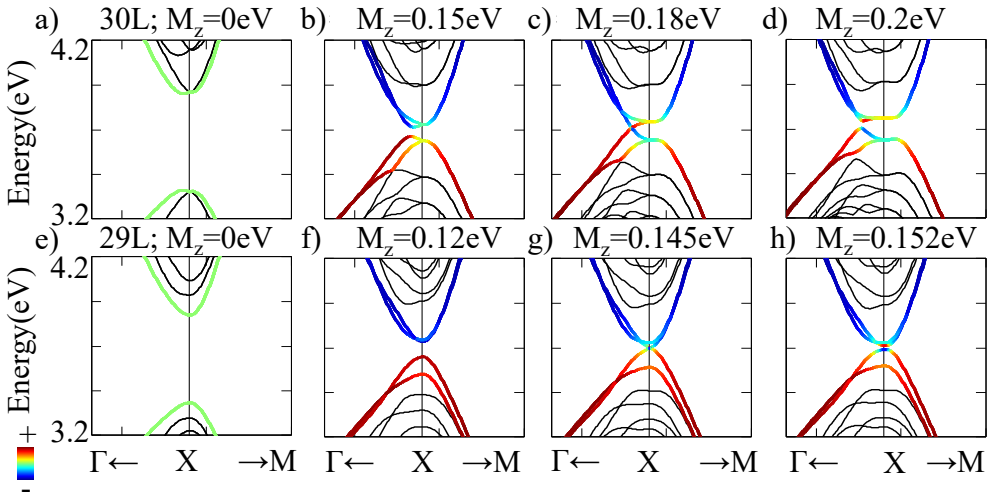

Figure 4.3: The band evolution of PbSe as a function of exchange field for even $L = 30$ (first row) and odd $L = 29$ (second row) number of layers. (a) 30L, $M_z = 0$eV (b) $M_z = 0.15$eV, (c) $M_z = 0.18$eV, (d) $M_z = 0.2$eV, (e) 29L $M_z = 0.0$eV, (f) $M_z = 0.12$eV, (g) $M_z = 0.145$eV, (h) $M_z = 0.152$eV. The color indicates the out of plane spin polarization.

band structure along high symmetry line for an even number of layers $L = 30$ in Figure 4.3(a–d)). As convention under zero exchange field all spins of the slab are in-plane with a trivial band topology, i.e the lowest conduction and highest valence bands are bulk states. However, a small exchange field can make the states inside the Brillouin zone non-degenerated with weak out-of-plane spin polarization at the vicinity of X point. However, even before phase transition the spin can change direction at the vicinity of X point due to the combination of exchange field and strong inter-orbital hopping energy (see Figure 4.3(c–d))). The critical spin state is very unconventional, exhibiting two spin channels along

high symmetry direction: one spin up, and one spin down mainly contributed by Pb and Se p-orbitals respectively (see Figure 4.3(c))), linear in the high symmetry direction. This spin-texture is common for all Sn doping concentration as a reflection of our initial model based on interacting Pb and Se p orbitals. Since there is no Z_2 symmetry in the system, the band gap is also shifted by exchange field in momentum space. The signal of QAH state is the band closes, and reopens with a mixed spin direction within one valence bands (spin down from X point until valence band maximum). As a result, the number of band inversion is 4, showing a QAH state with Chern number 4 (each low energy gap closes and reopen once, changing the QAH Chern number by one step). This is further supported by our Hall conductivity calculation by integrating the Berry curvature of all Bloch states in the momentum space.

As mentioned from the introduction of this section, the mechanism of phase transition could be quite different for odd number of layers $L = 29$. The material follows the TRS with zero out of plane spin-texture (there is still a even numbers of band). However, there is an absence of screw symmetric rotation of an odd number of layers. Hence, the states at X are no longer fourfold degenerated. Here, the results show the possibility that two states which are close in energy can have the same spin polarization direction (see Figure 4.3(f–g))). The critical magnetization shows a non-linear touch at X point ((see Figure 4.3(g)))). In the critical phase transition, the spin state in the vicinity of X point is completely in-plane which reminiscences the phase transition of Z_2 TI thin film. Each of the 4 X points stands for $1/2$ of a band inversion which is shown in Figure 4.3(h)). The band inversion is associated with the spin-inversion. Here, the QAH with a total Chern number 2 is predicted for magnetically doped PbSe with an odd number of layers. Three Dimensional (3D) view of the valence and conduction bands with three magnetization scales under different angles are presented in Fig 4.4–4.6. In the direction perpendicular to $\Gamma - X$, the band are parabolic like. By contrast with Z_2 QAHE, the QAH critical point of TCI can be achieved while

two parabolic band touch at a single point along $\Gamma - X$. Figs 4.4–4.6 suggest that the trivial thin film already has inverted orbital order under a sufficient exchange field when two bands still do not touch. The inverted regime is associated with a spin inversion which is not straightforwardly detectable due to the shift in momentum space of the low energy valley. The closing mechanism of trivial thin film is quite complicated compared to usual TCI surface state picture. However, the touching theorem presented in Fig 4.5(a) and Fig 4.6(a) is parabolic like in the direction perpendicular to high symmetry line. One more time here we emphasize that the mechanism is in sharp contrast with previous proposal [63] where a topological surface state was involved.

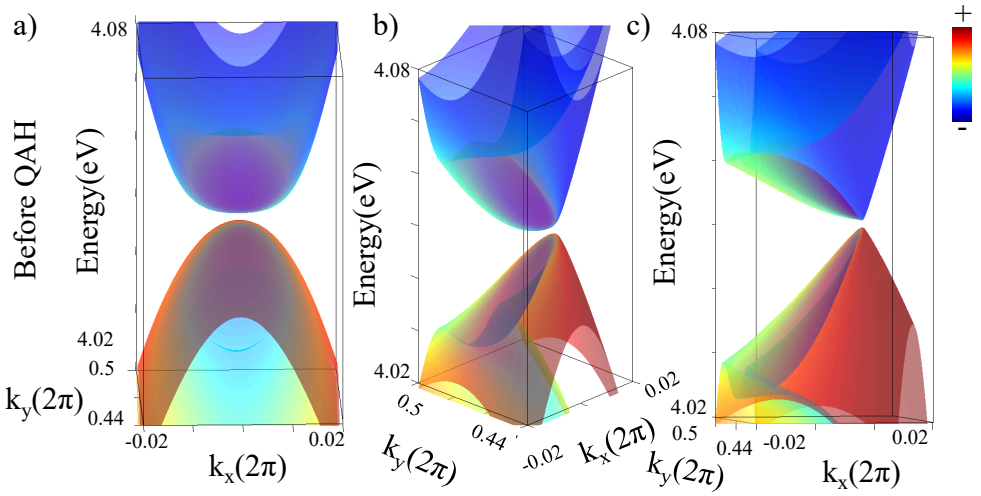

Figure 4.4: 3D view of the valence and conduction bands before phase transition in three different angles. The colour represents the total out of plane spin

4.4 Wave-function near the critical quantum anomalous Hall state

To understand the layer-dependence wave-function of the QAH state, we investigate the low energy wave function tunnelling properties over the slab. Specifically, we investigate the spacial wave-function of the lowest conduction bands near the Fermi level at the critical point of QAH (lowest conduction band – upper band). It is worth to mention that the surface state mainly contributes to

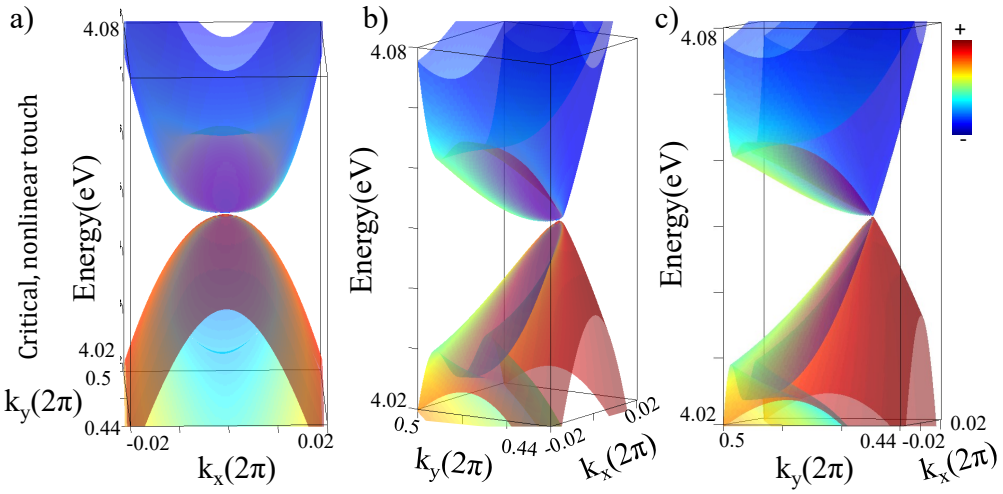

Figure 4.5: 3D view of the valence and conduction bands at QAH critical point with a parabolic like touch in three different angles

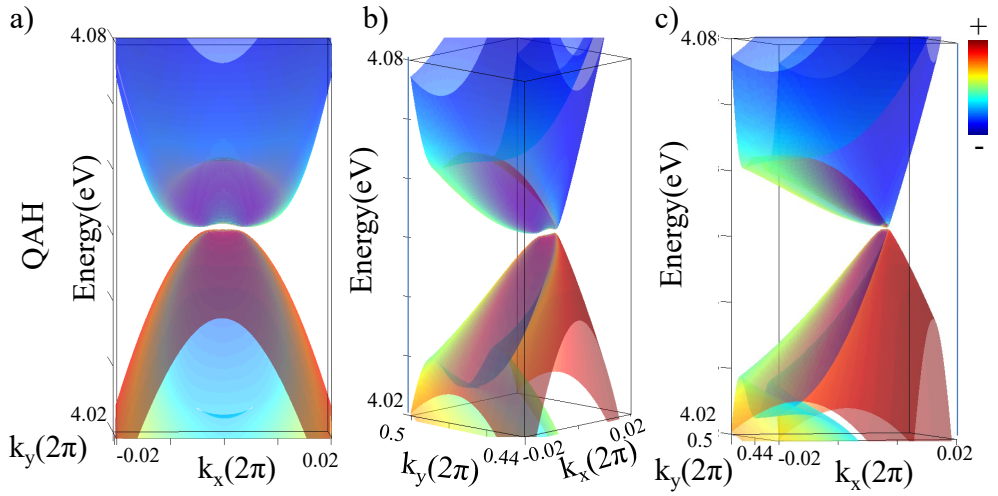

Figure 4.6: Unconventional band inversion which leads to the high Chern number quantized anomalous Hall state

higher energy with respect to the Fermi level. Meanwhile, the exchange energy shift the band gap away from the X points. Hence, it is possible to drive the low energy bulk states of trivial TCI thin film to the surface state. Figure 4.7 shows that the wave function distribution of lowest conduction band with magnetization for doping concentration $x = 0.1$ comes from bulk state, whereas the highest valence band is surface state like.

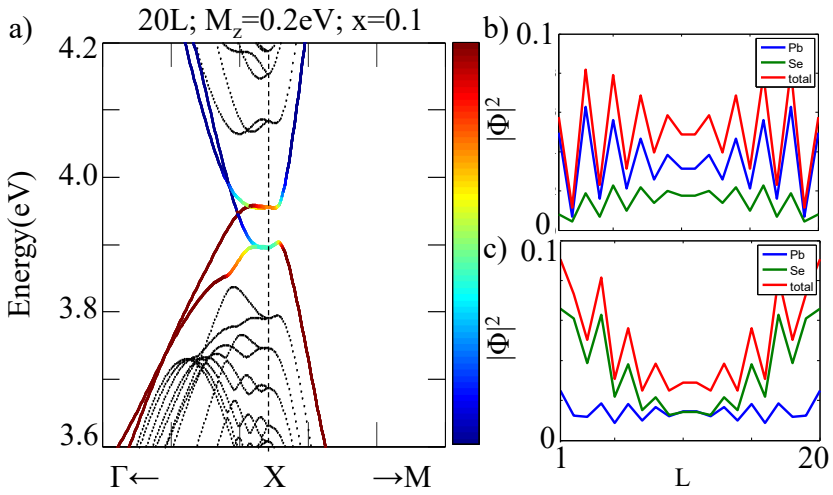

Figure 4.7: The critical QAH point bulk, surface character of the wave function. (a) The bandstructure of $Pb_{1-x}Sn_xSe$ for 20 layers, $M_z = 0.2$eV, $x = 0.1$ The layer dependence wave function with associating orbital contributions at single k-point are presented for (b) upper band and (c) lower band (minimum conduction and maximum valence bands).

4.4.1 High Chern number in $Pb_{1-x}Sn_xSe$ near a topological crystalline insulator critical point

At zero magnetization, the band-structure at critical point will exhibit bulk properties for both valence band and conduction band, irrespective of large number of layers (see Fig 4.8). However, as mentioned in the previous section, the magnetization will drive the band gap in the momentum space, far away from X point. Hence, at nearly QAH critical point, the initial high energy band close to Γ point will be shifted to low energy. In Fig 4.9, we choose a magnetization which is very close to QAH critical point and pick up two points in momentum space: highest conduction band and lowest valence band. It is quite possible that the gap is indirect because the two band edges move differently with magnetization. As can be noticed from Fig 4.9, the wave function of lowest conduction band is surface like, whereas the highest valence band is bulk like, oscillating with layer index. However, the layer-dependence wavefunction is still symmetric for homogeneous magnetic doping case (the inversion symmetry is not violated).

At the critical point, the difference between the gap, the quantum well states are negligible. Increasing the exchange field may lead to a second band inver-

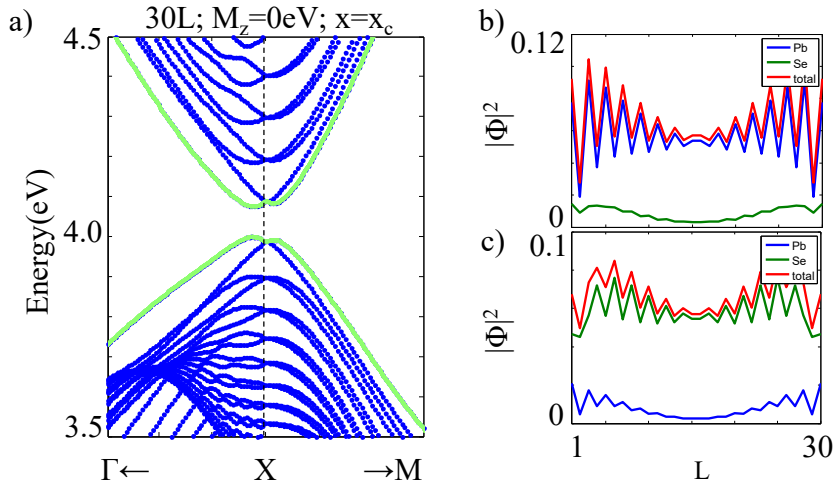

Figure 4.8: (a) The zero magnetization bandstructure with associating wave function distribution at critical doping and even number of layers $L = 30$ with associating orbital contributions for (b) upper band and (c) lower band.

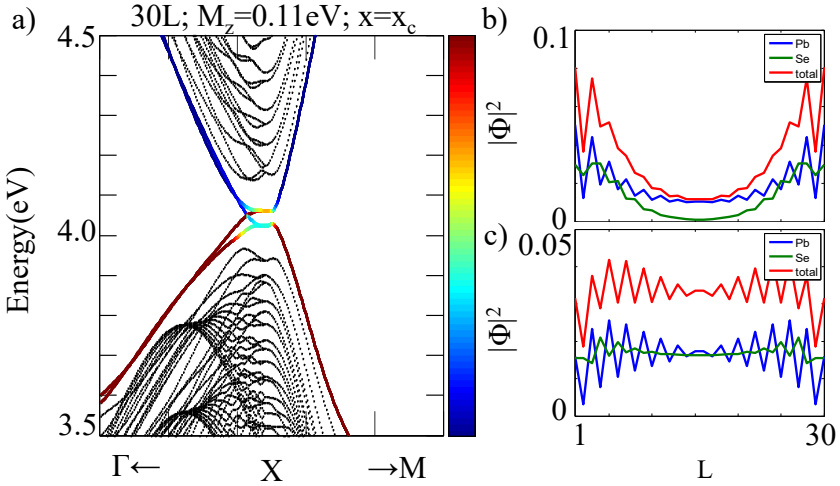

Figure 4.9: The QAH critical point bulk, surface character of the wave function. (a) The bandstructure of $Pb_{1-x}Sn_xSe$ for 30 layers, $M_z = 0.11$eV, $x = x_c$ The layer dependence wave function with associating orbital contributions are presented for (b) upper band and (c) lower band.

sion of all four local Dirac cones (see Fig 4.10). Interestingly, while the low energy of the first inversion carries both bulk and surface characters, the second band inversion is dominated by the surface states. This fact is a result of the initial quantum well bands which is dominantly contributed by surface layers. Fig 4.10 shows the QAH near second critical point $M_z = 0.35$eV when the Chern number becomes 8. As expected, the low energy bands are shifted far away from X point. Both of highest valence and lowest conduction band will have

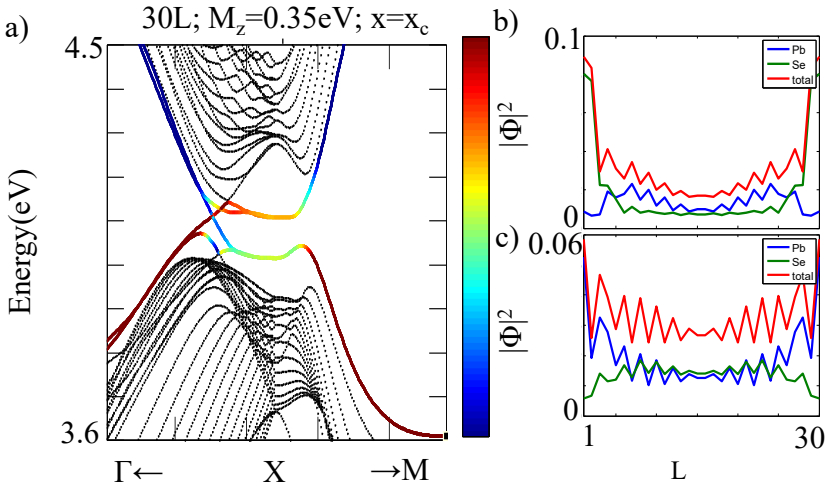

Figure 4.10: The second QAH critical point surface properties of the wave function. (a) The bandstructure of $Pb_{1-x}Sn_xSe$ for 30 layers, $M_z = 0.35$eV, $x = x_c$ The layer dependence wave function with associating orbital contributions are presented for (b) upper band and (c) lower band.

surface properties. It is worth mentioning that the second QAH band inversion will happen only at $x = x_c$ and with very large exchange field.

4.4.2 Quantum anomalous Hall effect induced by topological crystalline insulator surface state

A typical TCI thin film surface state band inversion is represented with the corresponding out of plane spin polarization. The TCI surface state can be observed within a thicker number of layer in the non-trivial side ($x = 0.5$). The model can be seen as exact two interacting Dirac cones based on $Pb_{0.5}Sn_{0.5}Se$ orbitals with the children Dirac cone induced by the tunnelling gap. We note that the massive Dirac fermion does not represent in thin film TCI surface state with magnetization, since the Dirac cone is not at time reversal invariance momentum. Instead the QAH surface state exhibit two Dirac cones with each of them having half spin up, and half spin down (see Fig 4.10(b)). This spintexture has never been predicted in previous study on QAH. The band inversion induced VHs is also not presented in highest conduction band like in previous theory for QAH of

trivial thin film. Here, we note that the existing accounts which use k·p theory fail to resolve the spin-texture of QAH in TCI surface state. Figure 4.12 presents

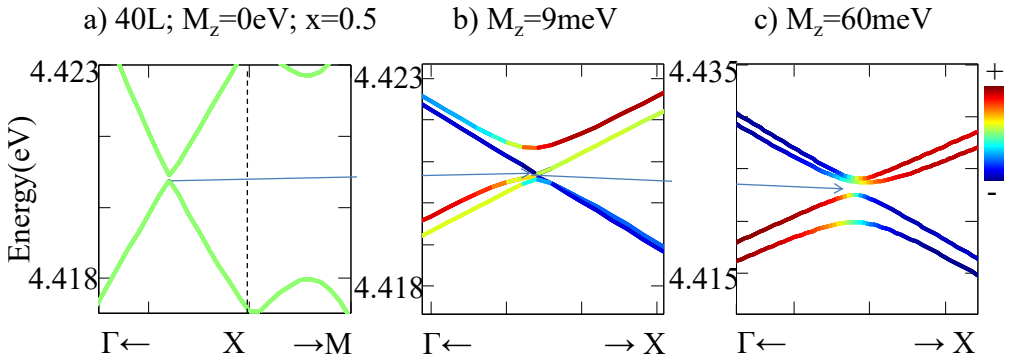

Figure 4.11: A typical surface band inversion mechanism for TCI without a VHs. (a) $M_z = 0$ (b) $M_z = M_c$ (c) $M_z > M_c$ QAH

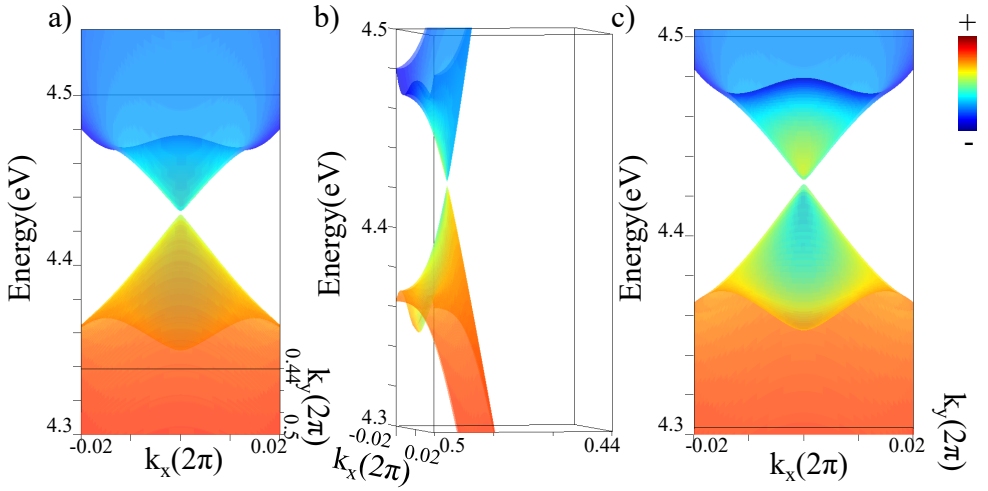

Figure 4.12: 3D view of the unconventional band inversion of TCI surface state without a Van-Hove singularity.

3D view of QAH for TCI thin film with corresponding out of plane spin polarization map. The QAH phase in TCI is distinguished with our unconventional band inversion with VHs. We note that the initial bands which are located at X point also move to low energy. At ultrahigh magnetization, the system can be easily driven to metallic state. We conclude that the TCI thin film is not a promising candidate to large gap Quantum Anomalous Hall Insulator (QAHI).

4.4.3 QAH Chern number for odd number of layers

In this subsection, the question how the Chern number can change from 2 to 4 for odd number of layers is addressed. As discussed above, the trivial side of TCI can close a band gap exactly at X point. However, the TCI side can have a similar surface state for very thick number of odd layers where the concept of children Dirac cone is acceptable. In this case, the parents gap could not dominate the tunnelling children Dirac gap to give a semi-metal. Hence, a Chern number 4 is expected for thick odd number of TCI layers. However, the QAH with odd number of layer and trivial thin film is not promising for high doping level $x \approx 0.1$. Fig 4.13 represents a mechanism where the gap closes and does not open for a reasonable high doping level. Here, the band inversion could not induce any gapped state.

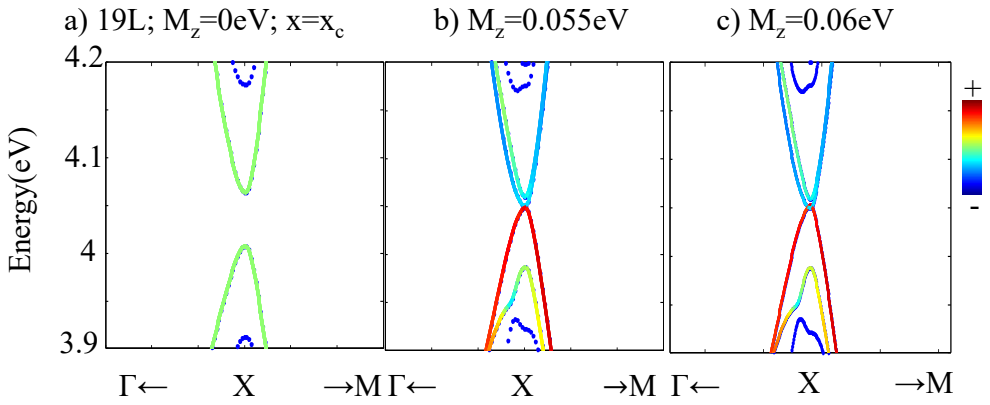

Figure 4.13: Odd number of layers (19) band evolution with a reasonable high doping level $x = x_c$. (a) $M_z = 0$eV, (b)$M_z = 0.055$eV, (b)$M_z = 0.06$eV

4.4.4 The critical momentum as a function of film thickness

From unconventional touching mechanism, we define position of the critical momentum at critical QAH point when two spin channels meet. It it realised that the with the same exchange energy scale, the band gap experiences a more considerable change when the thickness increases. Thus, the critical exchange

energy decreases as a function of thickness. However, from the previous section we concluded that the momentum shift in the band gap takes effect when the exchange energy is applied. The more magnetic exchange energy applied, the momentum shift increases. Out general conclusion is that as the slab becomes infinite, the critical momentum remains constant with respect to the X point. In other word, the critical momentum remains closer to X point for larger number of layers.

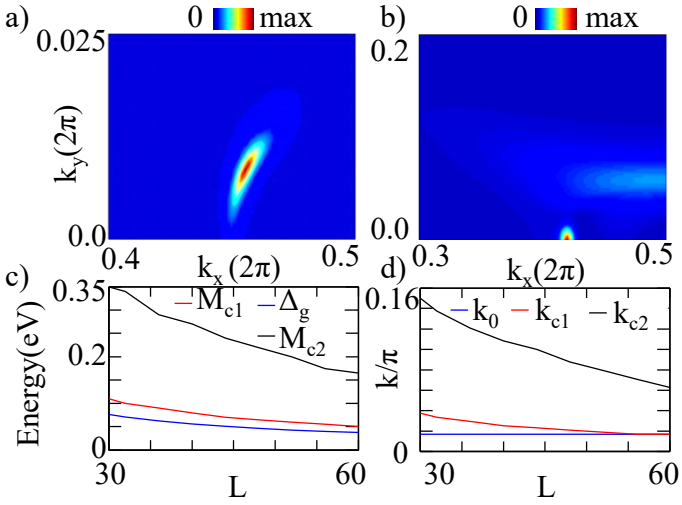

Figure 4.14: The Berry curvature calculated based on the Kubo formalism for two range of exchange field. (a) $M_{c1} < M_z < M_{c2}$ the QAH with C=4 having a VHs, the Berry curvature reflects the VHs, localized at low energy bands. (b) $M_z > M_{c2}$ the QAH with C=8. The Berry curvature contribution may come from higher energy band. (c) The layer dependence band gap and critical exchange field for first and second band inversions. (d) The layer dependence critical momentum for first and second band inversions

In Fig 4.14(a–b) we present our computed results of the momentum dependence Berry curvature for the two exchange energy range, when the Fermi level is located inside the magnetic gap. Moreover, from the linear response formalism the Berry curvature is inversely proportional to the square of momentum dependence energy gap. In the previous section, we reported on the existence of the VHs and two disconnected electron pockets. Here, the numerical results once again confirmed our initial proposal with peaks of the Berry curvature (see Fig 4.14(a)). The peak area occupies a small part in momentum space, shifted away from high symmetry line. The emergent Berry curvature is consistent with

the shape of two disconnected electron pockets, verifying the accuracy of our numerical results. The integration in momentum space gives an integer number, confirming that the slab is in QAH with C=4. The second phase transition (not presented here) is similar to the first phase transition but it is generated by higher energy quantum well states. As can be seen from Fig 4.14(b), the Berry curvature is destructive despite of the presence of second band inversion induced VHs (this VHs is similar to Fig 4.14(c)). The Berry curvature is distributed in a larger momentum window compared to the former case.

Figure 4.14(c) shows layer dependence band gap at the TCI critical point with the associating critical exchange energy for the first and second band inversions. We note that the number of layers is even, odd number of layers can show different behaviour. The trends clearly demonstrate that the band gap, the first and second critical exchange fields decrease as a function of layers. The band gap trend can be well explained through the interlayer tunnelling effect, whereas the critical exchange field should overcome the tunnelling band gap. For the critical thin film, the QAH with C=8 occurs if many factors can be overcome including the initial band gap, the quantum well gap and the shift in momentum space. However, we found that the critical thin film with exchange field is a promising candidate for QAH transport experiments. The layer dependence momenta of highest conduction band k_0 and the QAH critical momenta k_{c1}, k_{c2}, measured from Γ point to critical points are also shown in Fig 4.14(d). The layer effect does not change k_0, whereas it decreases the critical momenta k_{c1}, k_{c2}. All these features are consistent with the trend of M_{c1}, M_{c2}. Since smaller critical exchange fields with large number of layers can shift the conduction band minimum lesser compared to thinner films, the critical momenta also decrease when L increases. To a certain thick film limit, when the initial band gap is very small, the smaller critical momenta k_{c1} is comparable with k_{c0}. Thus, these prominent features might help ARPES to detect the band inversion of magnetic films.

4.5 Controlling quantum phases via a rotated exchange field or an electric field

In this section, we will define s new tuning principle from trivial non QAH state to QAH when the magnetization is not sufficient for the unconventional phase transition. One experimental challenge of the non QAH state is that if the exchange field is very close to the critical field, but it is not sufficient to open a magnetic gap, we consider number of perturbations which can drive the thin film (including trivial, critical and TCI films) to QAH state. Firstly, by rotating magnetization in the real space, we can design a switching device principle for TCI. Secondly, we adapt the electric field to tune the system at the TCI critical point.

4.5.1 The quantum control by in-plane magnetization.

While the out of plane magnetization does not break the C_{4v} symmetry, the in-plane magnetic rotation can give a shift in the parent Dirac cone of TCI surface state and a C_{4v} broken symmetry is expected. When the tunnelling gap of TCI surface state is small, an in-plane magnetization can break the rotation symmetry, transforming TCI to semi-metal. We remind the case mentioned in Chapter 2 for the magnetic Z_2 TI, an in-plane component of magnetization can shift the Dirac cone in momentum space. However, the picture is completely different for the trivial thin film which can only be analysed by our tight binding model. Due to a large gap of parent trivial bulk state between p orbitals of Pb and Te, we choose a magnetization close to QAH critical point, slowly rotate the magnetization with small angles θ, and ϕ.

Figure 4.15(a) describes a schematic diagram demonstrating how we can tune the magnetization direction or the substrate induced electric field. Indeed, in the experiment it is possible to control the magnetized slab by the nature

magnetic doping. Thus, the magnetization vector can be described in spherical coordinate $M = M(\theta, \phi)$. Moreover, our assumption that the potential gradient in each layer is realistic, since the crystal has planar slabs based on two types of atoms.

Figure 4.15(b) represents our results of magnetic rotation QAH, with a simple symmetry analysis. In the presence of both in-plane and out of plane magnetic components. The degeneracy in energy dispersion of the perpendicular direction to in-plane magnetization is destroyed by broken mirror symmetry. Meanwhile, the energy along Brillouin zone boundary of parallel direction is still doubly degenerated with mirror symmetry. Moreover, it is possible to transform the shape of energy dispersion by the magnetic rotation along ϕ when both the in-plane component at M_x and M_y are presented. In this case, all the degeneracies at zone boundary are broken.

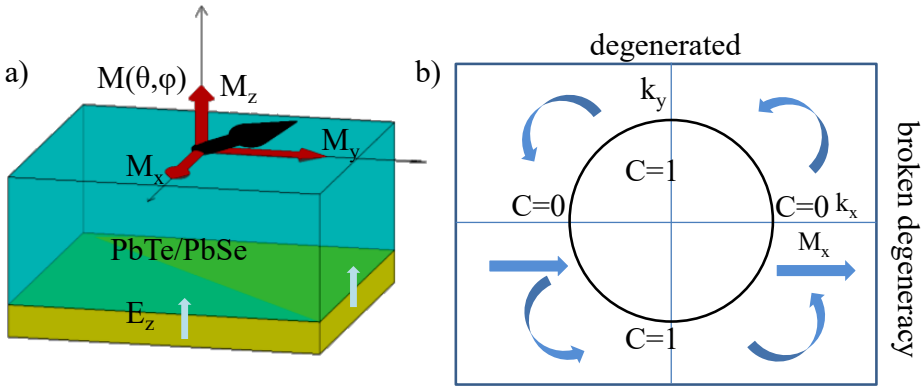

Figure 4.15: A schematic diagram of the external symmetry-broken perturbation which can drive the system into a new QAH phases. (a) Crystal of IV-VI based semiconductors with strong spin orbit coupling and mirror symmetry. Three components of magnetization $M = M(\theta, \phi)$ or $M = (M_x, M_y, M_z)$. E_z–a substrate induced electric field. b) Broken symmetry sub-band structure of local QAH band inversion occurs with magnetic rotation along $\Gamma - (\pi, 0) - (\pi, \pi)$. If there is only M_x component then only degeneracy at $(0, \pi) - (\pi, \pi)$ is broken.

The realistic bandstructure of PbTe near QAH critical point is represented in Fig 4.16 and Fig 4.17 in direction perpendicular and parallel to the in-plane magnetic component, respectively. Figs. 4.16–4.17 shows the changes in sub-band

structure evolution of non-QAH phase with magnetic rotation along direction perpendicular and parallel to the in-plane magnetic component, respectively. The total modulus of magnetization **M** remains constant, whereas the components change with respect to angle ϕ. As expected, the band gap in the direction perpendicular to M_x does not change to a non-trivial, instead it increases with the split of states along X–M. Thus, the in-plane magnetization can only increase the direct gap until the gap becomes indirect and a band inversion is hardly happens. By contrast, the gap in the parallel direction to M_x along $\Gamma - (0, \pi) - (\pi, \pi)$ closes and reopen, changing the topology at the local gap (see Figs. 4.17–4.18). The change in topology, however, is not robust where there might be indirect band gap and insulator–metal phase transition.

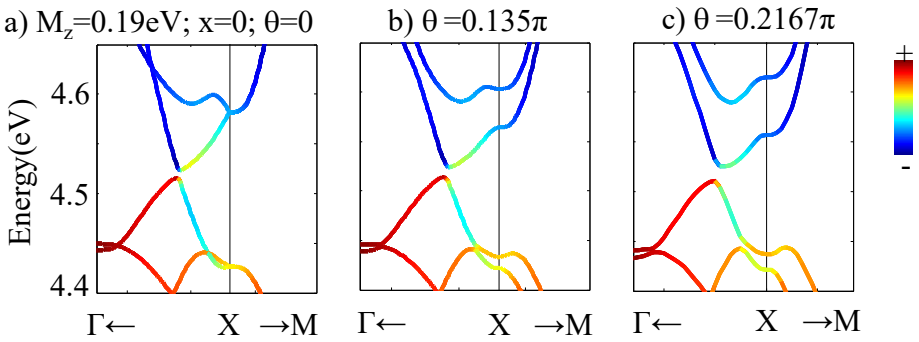

Figure 4.16: The band evolution of PbTe as a function magnetic rotation angle θ, 14 layers, $|M| = 0.19$eV, $\phi = 0$, in direction perpendicular to the in-plane magnetic component (a) $\theta = 0$, (b) $\theta = 0.135\pi$, (c) $\theta = 0.2167\pi$

However, a total Berry curvature integration is needed to confirm that along k_x where the band inversion does not happen and the total local Berry curvature is zero, along k_y the total Berry curvature is 2 (see Fig 4.19)(c–d). As discussed above, we have two band inversions along k_y, gapped bands along k_x thus the system exhibits Chern number 2. In the first non-inverted Dirac cone although the Berry curvature can have a small negative peak, a positive contribution around the peak makes the total Berry curvature to be zero. By contrast,

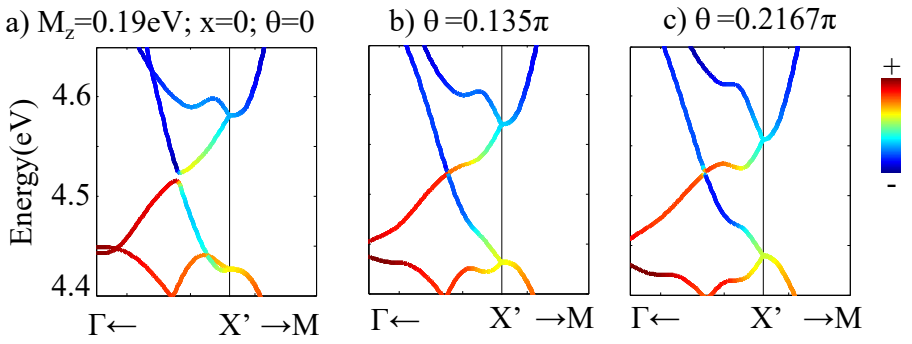

Figure 4.17: The band evolution of PbTe as a function magnetic rotation angle θ, 14 layers, $|M| = 0.19$eV, $\phi = 0$, in direction parallel to the in-plane magnetic component (a) $\theta = 0$, (b) $\theta = 0.135\pi$, (c) $\theta = 0.2167\pi$

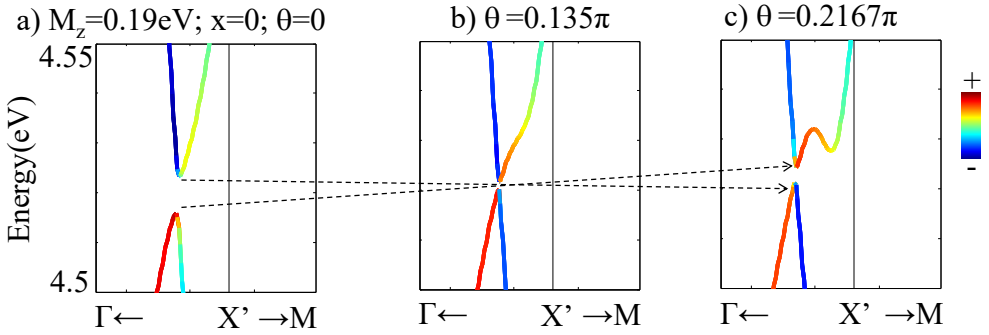

Figure 4.18: The phase transition mechanism near the QAH critical point, $|M| = 0.19$eV, $\phi = 0$, (a) $\theta = 0$, (b) $\theta = 0.135\pi$, (c) $\theta = 0.2167\pi$

a positive peak around the inverted Dirac state can give a non-zero quantized Chern number. Overall, this supports our proposal of phase transition induced by magnetic rotation for even number of layers. Thus, due to local band inversion and asymmetry, it is possible to drive the system to three phases. By applying topological band theory, we can design a device principle as follow: an out of plane magnetization which is smaller than critical magnetization can give an insulator with no edge state; rotating the magnetization with a small angle θ can drive the system to QAH state with C=2; keeping $\theta = const$, $\phi = 0 \rightarrow \pi/2$ can

change the local band inversion, increase θ more can give a semi-metal phase.

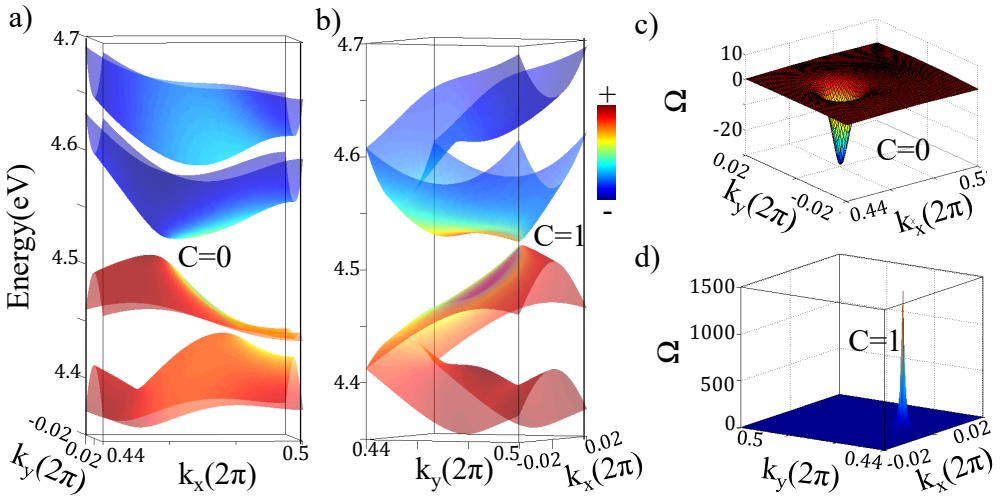

Figure 4.19: Two Dirac cones characterizations with their associating Berry curvature. The region close to low energy band Bery curvature is highlighted

4.5.2 The quantum control by electric field.

We next demonstrate an electric field-tunable QAH phase in a trivially insulating, even N_l, $Pb_{1-x}Sn_xSe$ thin film with $x \approx x_c$ under a nearly critical $\mathbf{M} = (0, 0, M_z)$. The necessary electric field can be either applied externally or effectively produced by a certain substrate which is usually present when preparing a thin film epitaxially. Any finite electric field "E_z" along z-axis breaks $z \to -z$ reflection symmetry for a thin film and destroys all screw rotation symmetries as well.

One straightforward way to show the tunability of E_z toward a QAH phase is to study the band gap evolution (around X) as a function of E_z. As shown in Fig. 4.20 (a) for a $N_l = 30$ thin film with $M_z = 0.11$ eV, the gap does decrease, close, and reopen, reflecting a typical process for a topological phase transition. A closer examination from the spin-resolved spectrum around X, as can be seen in Figs. 4.20 (b)-(d) [corresponding to three cross symbols respectively in Fig. 4.20 (a)], further confirms the occurrence of the magnetic band inversion. Such band inversion then indicates the phase transition from a $C = 0$ trivial phase to a $C = 4$ QAH phase.

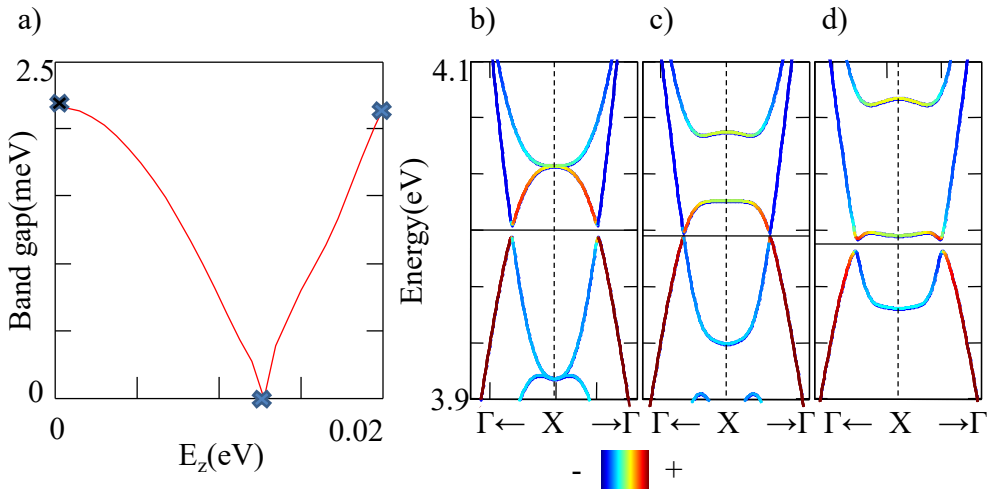

Figure 4.20: (a) The band gap as a function of electric field when $M \approx M_c$. (b-d) The electric field induced phase transition.

4.6 Conclusion

In summary, we have made a comprehensive prediction on realizing various QAH phases with high Chern number (See Table 4.1) in trivially insulating thin films, $Pb_{1-x}Sn_x$(Se,Te), upon increasing exchange field strength. Although the formation of any QAH phase we investigate here is based on a conventional mechanism, namely, a magnetic band inversion between conduction and valence bands (quantum well states), the band structure evolution is usually found to be "unconventional", compared to the previous scenario involving TCI surface states [63]. Such an "unconventional" process strongly depends on the chemical composition, number of layers, and exchange field strength.

Doping	M_z	θ	E_z	N_l	$\overline{XM}$ DEG	C
$x \leq 0.08$	$+$	$-$	$+/-$	odd	$-/+$	2
(X=Se)				even, $N_l \geq 19$	$+$	4
$x \approx 0.2$	$+$	$-$	$+/-$	odd	$-$	$-$
(X=Se)				even, $N_l \geq 30$	$-/+$	$4 \cdot n$
$x > 0.2$	$+$	$-$	$-$	odd	$-$	4
(X=Se)				even, $N_l \geq 30$	$+$	4
$x \approx 0$	$+$	$+$	$-$	even, $N_l \geq 14$	$-/+$	2
(X=Te)					C_4 breaking	

Table 4.1: Summary of QAH phases obtained in $Pb_{1-x}Sn_xX$ thin films (X= Se or Te). The formation of each ground state depends on various factors, such as chemical composition x, number of layers N_l, magnetic exchange field M_z, magnetic rotation angle θ, and effective electric field E_z. In addition, the spectrum can have twofold degeneracy along BZ boundary ($\overline{XM}$ DEG, in short) if screw rotation symmetry remains intact in the system. $+/-$ indicates the presence/absence of such factor.

In particular, we highlight: 1) There is a significant (N_l) even-odd effect. For instance, for a slightly Sn-doped PbSe, the odd N_l thin film and the even N_l one exhibit QAH effect with $C = 2$ and $C = 4$, respectively, when $M_z > M_c$. Moreover, the emergent VHSs after band inversion appear only in the latter case, not in the former one. These distinct behaviours basically originate from different symmetries they possess. 2) The best strategy to obtain an ultra-high Chern number ($C \geq 8$) phase is to consider $Pb_{1-x}Sn_x$(Se,Te) thin films with nearly critical doping $x \approx x_c$. The main reason is due to the decrease of the energy gap between adjacent quantum well states and hence reduces the necessary M_z. 3) Using a rotated exchange field (*i.e.*, producing finite in-plane magnetization) or an applied electric field can drive the system from a trivial insulator to a QAH insulator even though $M \lesssim M_c$. This provides a new design principle for applications, for example, an on/off switch device.

Chapter 5

Intrinsic spin Hall effect in topological insulator

5.1 Physics of intrinsic spin Hall effect

Recent developments in the field of Hall effects in Topological Insulator (TI) have heightened the need for realistic system in spintronics application. In parallel with Quantum Anomalous Hall Effect (QAHE) study, there has been renewed interest in intrinsic Spin Hall Effect (SHE) in TI and spin-orbit coupling system.

The SHE was originally predicted in Two Dimensional Electron Gas (2DEG) system with Rashba Spin–Orbit Coupling (SOC) under the electric field. In 2DEG system, the spin and angular momentum couple and form a circular spin-texture when the spin are completely in-plane, coexisting with orthogonal angular momenta. In an original work proposed by Hirsch [66], a tranverse charge current perturbs paramagnetic metal, causing a spin imbalance with a spin Hall voltage. Under in-plane electric field, the spin experience a torque, and all the spins precess in $\pm z$ direction (direction perpendicular to 2DEG) [15, 66]. The SHE can be seen as two copies of the anomalous Hall effect when the spin-up and spin down electrons can move in two opposite directions. The mechanism of SHE can be various and coexist in the same material. Treating the mate-

rial with coexisting SHE mechanism requires large effort since each effect can dominate in certain impurity limit. Different from the Quantum Anomalous Hall (QAH) effect described above when only the low energy spectra electron plays the main role, the SHE can be dependent on the whole electronic structure and can only be simplified in k·p picture within framework of few-bands involvement if the role of high energy bands is negligible. The skew scattering SHE is present when a electron scatters asymmetrically with impurity center and can be described by traditional Boltzmann transport equation [67]. When the inter-band effect is neglected. The side jump mechanism, however, arises due to the anomalous term in the spin-orbit coupled system which takes part in the Boltzmann equation (or in the Kubo formula) [67–69].

Several studies have been carried out to investigate the spin phenomenon in different materials (tramsition metals, spin Hall semiconductors) [56, 70, 71] and TI is emerging material class for experimental measurements. In our work, we consider intrinsic spin Hall effect which is originated from bandstructure, the extrinsic mechanisms can contribute to the spin Hall currents through interactions and impurities.

5.2 Intrinsic spin Hall effect in topological insulators

Traditionally, the spin current in TI corresponds to edge states with a linear Dirac dispersion [72] in a 2D system like HgTe/CdTe quantum well [73]. The QSHE is protected by the edge state and robust against weak perturbation, but the SHE is sensitive to the bandstructure, impurity and chemical potential. While the first prediction of SHE is on the paramagnetic metal, the intrinsic SHE can also exist in the semiconductor system with tunable characters where the spin Hall conductivity is sensitive to external stress, impurity and the gap [56]. In

the topological scenario, the spin-orbit coupling materials are the same for both semiconductors and insulator. However, due to the large gap the SHC current can be much smaller for insulators compared to semiconductors.

Hence, the topological materials with SOC become promising material class for SHE measurement. The measurement using optical technique such as Kerr rotation spectroscopy can detect the bulk signal of spin accumulation process. Recently, the spin Hall effect tunnelling spectroscopy experiment has been used to investigate the intrinsic SHE and detect the surface signal of spin Hall conductivity [74]. However, the bulk-surface combination, still remains unsolved. We ask an important question that if the SHC of thin film TI can be comparable with the bulk SHE. Moreover, at what energy range of the chemical potential, the SHE can reach a large value which promises a potential technological application.

In figs. 5.1(a–b) we propose our schematic physical picture for SHE in thin film TI when all the bands are discrete. A spin polarized bulk or surface states all can give a contribution to the total spin Hall current. An TI thin film with discrete bands is combination of many Quintuple Layer (QL) for Bi_2Se_3, each bands are interacting and the SOC is considered totally in-plane. Hence, in the accumulation the spin polarized electron can precess from bulk to surface states, surface to surfaces and bulk to bulk inside the material (indicated by red arrows in fig 5.1(b)). This chapter aims on the spin Hall conductivity for thin film of TI. Firstly, we consider chemical potential dependence SHE of bulk, treating the 3D bulk Bi_2Se_3 with different electric field and spin directions. We found that the spin direction a long z direction ([111]) under in-plane electric field possesses the largest value for SHC inside the bulk gap. However, if the chemical potential naturally shifted due to the impurity, the SHC can reach a large value if the chemical potential lies in-between two band crossing centres. We also focus on a layer dependence study which show that in the ultra thin film limit of 1-2QLs the SHC is almost zero inside the gap. However, the surface states suppress a large

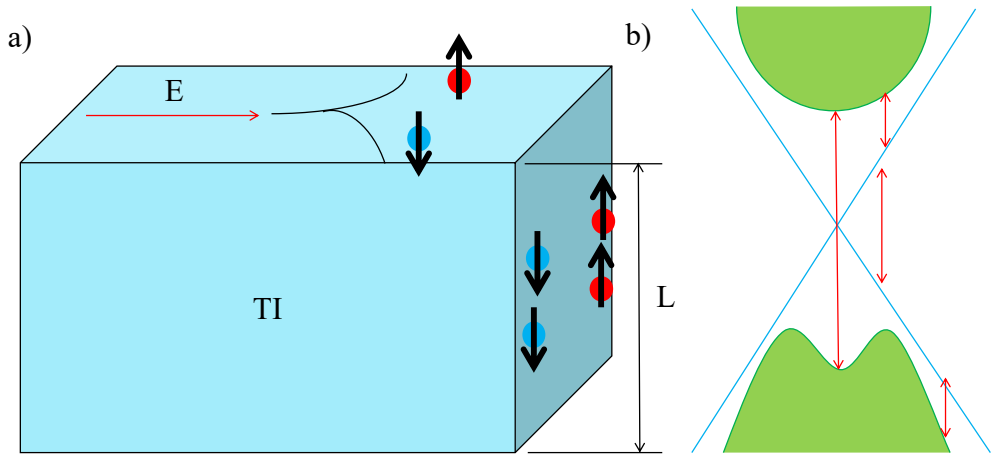

Figure 5.1: Physics for intrinsic spin Hall effect of Z_2 topological materials. (a) Electron spin is responded to an in-plane electric field E and the spin polarized electrons are separated to two opposite directions (perpendicular to the electric field). (b) The SHC of thin film TI is complex which involves bulk-bulk SHC, bulk-surface state, surface-surface scattering.

contribution of bulk states SHC. By analysing the SBC through k·p Hamiltonian with quadratic band dispersion, we explain an anisotropy of SBC for thin film TI and predict an asymmetric behaviour for momentum dependence of the Berry curvature. Meanwhile, in the energy limit away from the Dirac cone, the SHC for thin film can be enhanced due to the presence of nearly crossing bands.

5.3 Response formalism for spin Hall conductivity

The SHC can be calculated within the linear response formalism. In the context of band-structure dependence, each spin can be separated through a spin current operator when the spin couple with the velocity operator, the spin Hall conductivity is thus:

$$\sigma_{ij}^{k} = \frac{e}{V} \sum_{k,n} f_{n,k} \Omega_{n,k} \tag{5.1}$$

where the SBC

$$\Omega_{n,k} = \sum_{n} \frac{2.Im[\langle m|j_i^k|n\rangle\langle n|v_j|m\rangle]}{(E_m - E_n)^2}, \tag{5.2}$$

V is volume of the unit cell, $f_{n,k}$ is the Fermi Dirac distribution function. Velocity operator: $v_j = \frac{\partial H}{\hbar \partial k_j}$; the spin current operator: $j_i^k = \frac{1}{4}\{\sigma^k, v_i\}_+$ describes that the spin current can be separated for spin-up and spin down electron flowing in two opposite directions. This formula shows the k-spin Hall current along i direction, in response to electric field in j direction.

Different from the Hall conductivity which can describe a topological invariance and can be converged to an integer unit of $\frac{e^2}{h}$, the Kubo formula for spin Hall conductivity essentially depends on the spin polarization strength, spin-orbit coupling constant and energy dispersion. Moreover, even for an insulating state with no Fermi surface, the spin Hall effect still presents with the signals collected from all energy bands of the Fermi sea. Meanwhile, the spin dominant direction can be originated from the crystalline anisotropy. Moreover, the SHE can be enhanced by the band inversion induced by the spin orbit coupling where the SBC peaks, contributing to total SHC. The kpoints sampling methods: The model for bulk Bi_2Se_3 has b vectors [75]:

$$b_1 = (-1, -\frac{\sqrt{3}}{3}, b).g,$$
$$b_2 = (1, -\frac{\sqrt{3}}{3}, b).g,$$
$$b_3 = (-1, \frac{2\sqrt{3}}{3}, b).g,$$

for rhombohedral primitive translation vectors $g = \frac{2\pi}{a}$. The volume of the unit cell is thus: $V_{rhombo} = \frac{\sqrt{3}}{6}a^2c$ We transfer from the non-othorgonal velocity operators to orthogonal coordinate system: $v_{b_i} = \frac{\partial H}{\partial k_{b_i}}$ but $k_{x,y,z} = B.k_{b_1,b_2,b_3}$ and $k_{b_1,b_2,b_3} = B^{-1}k_{x,y,z}$ $v_j = \sum_j \frac{\partial H}{\partial k_{b_i}} \frac{\partial k_{b_i}}{\partial k_j}$ where $\partial k_{b_i}/\partial k_j$ are the matrix elements of B^{-1} having , the same dimension as the velocity operator. The dimension of SHC per unit cell volume is thus: $[\sigma_{ij}^k] = \frac{\hbar}{e}\Omega^{-1}\text{Å}^{-1}$ or $[\sigma_{ij}^k] = \frac{\hbar}{e}\Omega^{-1}\text{cm}^{-1}$

For rhombohedral TIs, the unit cell contains 5 atoms.

The finite thickness of thin film TI, however, can have only definite SHC with the average SHC for each QL: $\sigma_{xy-QL}^z = \frac{\sigma_{xy}^z}{L}$ where L is the thin film thickness.

Here the z direction is perpendicular to [111] surface of Bi_2Se_3. In principle, the bulk and thin film SHC should have the same dimension to be comparable. We consider SHC for the model with 20 bands of 5 atoms each QL, the same number of bands and orbitals for our rhombohedral unit cell.

5.4 Bulk spin Hall conductivity

As presented in Figure 5.2 the SHE calculation is carried out for a k-mesh of 61x61x61 and zero quasi-particle broadening. The velocity operator was defined from the tight-binding model projected into Cartesian coordinate, possessing both diagonal and off-diagonal terms. We found that the diagonal term of the velocity operator is important for SHC, especially inside the bulk gap, when the insulator state can have small SHC values.

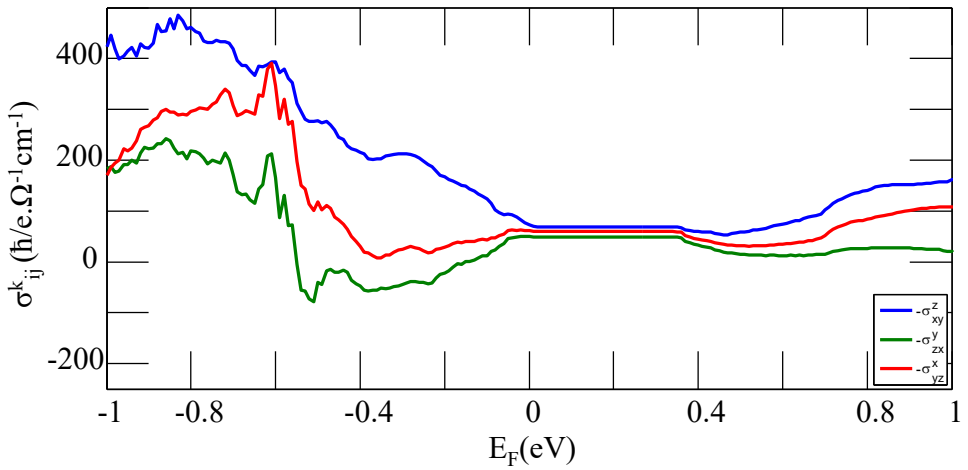

Figure 5.2: The intrinsic spin Hall conductivity in response to electric field in x,y,z directions respectively.

Outside the bulk gap when many bands involve, the Berry curvature peaks when two band crosses and a gap opened by the SOC and this gives a large contribution for the total SHC. Moreover, the SOC parameters also play a very important role in the SHC calculation when the off diagonal elements of the velocity operators proportional to the SOC energy. In next sub-section, we will

show that the SHC can also be controlled by the mass terms from the k·p Hamiltonian. From the results of SHE in Figure 5.2, the SHC is largest for the z-spin ([111 surface]) of the bulk Bi_2Se_3. This result comes from the large hopping energy within the quintuple layer of TI compared to the inter-QL tunnelling term. The momentum dependence SBC Ω^z_{xy} can partially explain the tendency of SHC. Firstly, in Figure 5.3–5.5 although the main feature of C_3 symmetry is broken, the hexagonal feature originated from the crystal lattice around the Γ point still survives. As can be noticed, for all three cases, the sign of Ω^k_{ij} is opposite for two pair of conduction and valence bands. For example, the valence band can carry negative contribution around the Γ point, whereas a positive SBC comes from the conduction band.

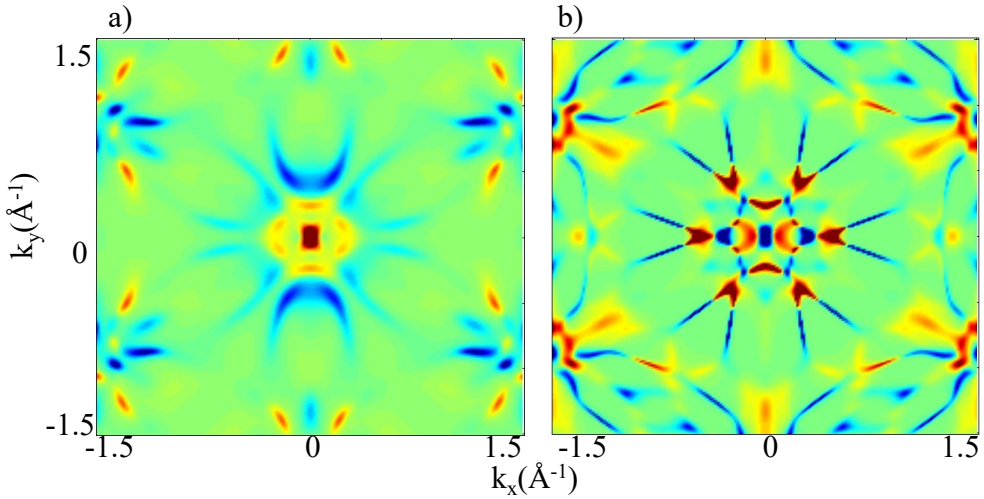

Figure 5.3: Momentum dependence spin Berry curvature for (a) lowest conduction bands and (b) highest valence band Ω^z_{xy} at $k_z = 0$

While the conductivity tensor is a 3×3 matrix of σ^k_{ij}, one need to consider only the three components $\sigma^z_{xy}, \sigma^y_{zx}, \sigma^x_{yz}$. The other components of the tensor can only get zero values or can be transformed from the three SHCs depicted above. Due to the symmetries including mirror symmetry and rotation symmetry of the crystal Bi_2Se_3 we have:

$$\sigma^x_{xy} = \sigma^x_{yx} = \sigma^x_{xz} = \sigma^x_{zx} = 0 \tag{5.3}$$

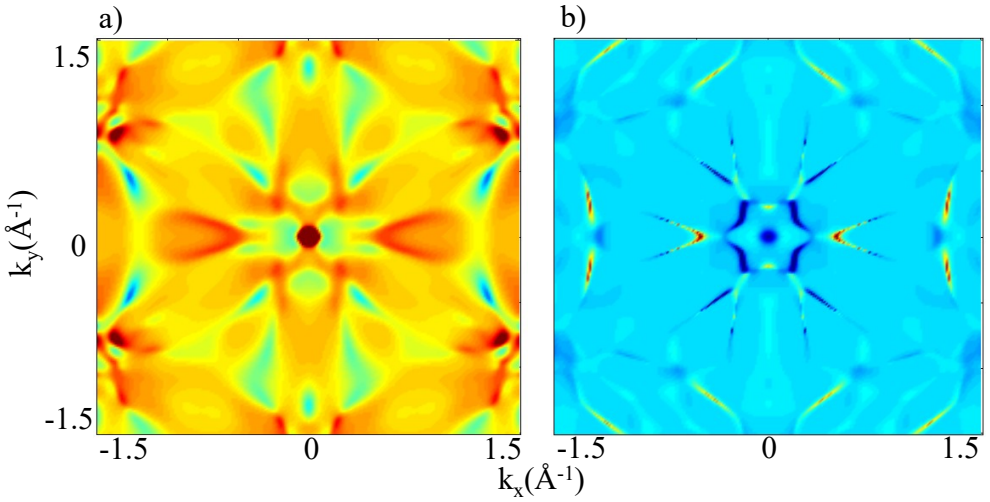

Figure 5.4: Momentum dependence spin Berry curvature for (a) lowest conduction bands and (b) highest valence band Ω^y_{zx} at $k_z = 0$

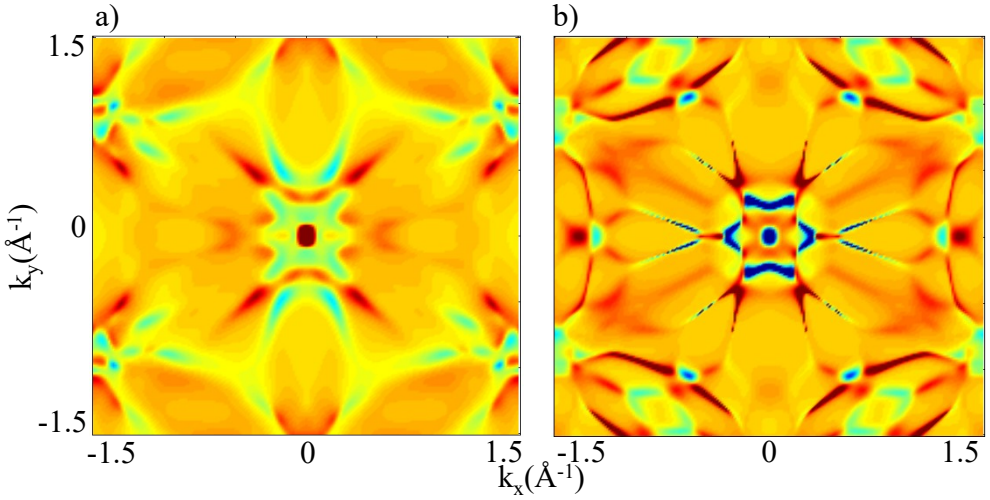

Figure 5.5: Momentum dependence spin Berry curvature for (a) lowest conduction bands and (b) highest valence band Ω^x_{yz} at $k_z = 0$

$$\sigma^y_{xx} = \sigma^y_{yy} = \sigma^y_{yz} = \sigma^y_{zy} = 0 \tag{5.4}$$

$$\sigma^z_{yx} = -\sigma^z_{xy} = 0 \tag{5.5}$$

To check the consistency of the source code, we confirm the results for $\sigma^z_{xy} = -\sigma^z_{yx}$ (shown in Figure 5.6).

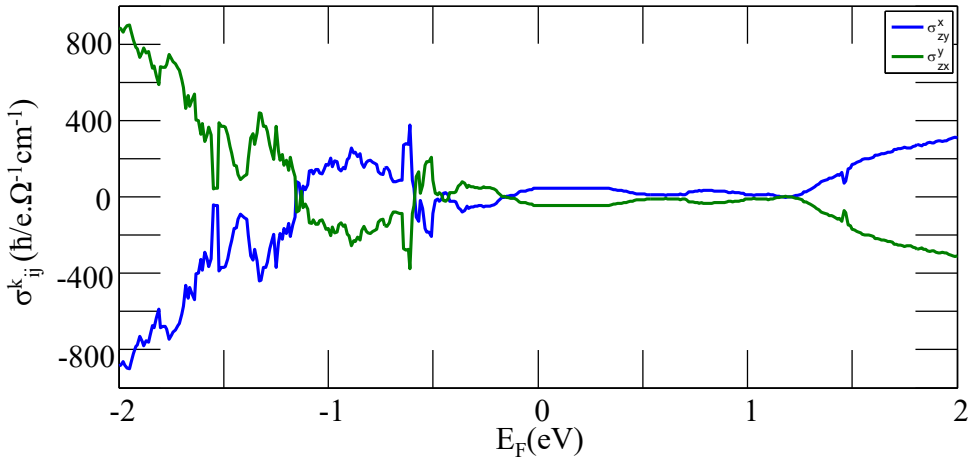

Figure 5.6: Symmetry of the spin Hall conductivity tensor $\sigma^z_{xy} = -\sigma^z_{yx}$.

5.5 Thin film spin Hall conductivity

While the bulk of Bi_2Se_3 has rhombohedral structure, the primitive unicell of thin-film TI is hexagonal . Here, we computed the layer dependence SHC for thin films with different thicknesses (2-10QLs). Since each QL contain the same number of electrons, the total number of electron orbitals should be $Norb.N$ (N– number of QLs), being finite. As can be seen from Figure 5.7 the Fermi level dependence average SHC per QL follow the same trend for all thin film thickness above 3QLs. For TI of thickness of 1-2QLs, the inter-surface interaction dominates and no strong signal presents. Hence, the SHC signal should be weaker compared to thick TI slabs. As can be noticed, the SHC in very low Fermi level can reach values as high as $\approx 2000\frac{\hbar}{e}\Omega^{-1}cm^{-1}$. This is the result of the extensive band crossing of the bulk and surface bands at low energy.

We now focus on the energy region where the bulk and surface states separate without a band crossing feature in Figure 5.8–5.9. As discussed above, the sign of SHC inside the bulk depends on the spin polarization (spintexture), but it is independent of the helicity (for surface state as an example). As can be seen from the figure, a finite film SHC around the Dirac cone region is a combination of bulk and surface. The total SHC values, however, is known only after bulk projection. A sudden "jump" in SHC can be seen when the Fermi level changes

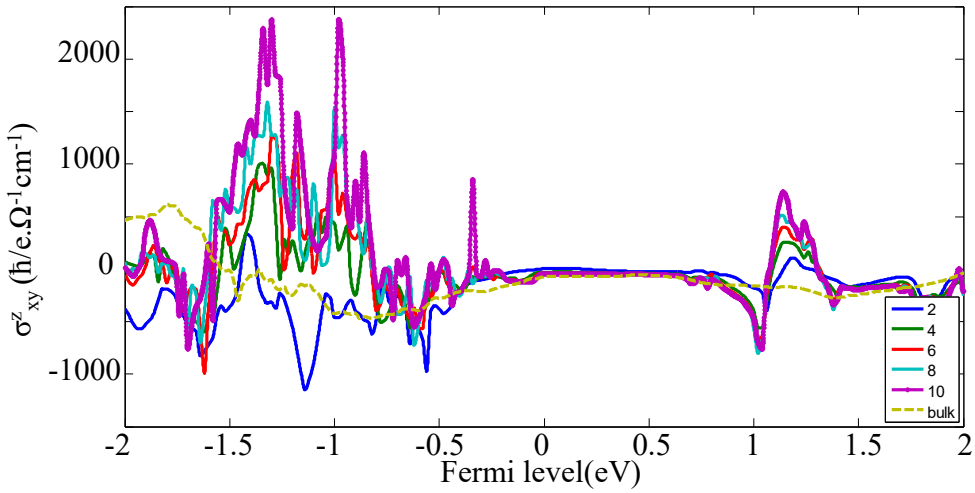

Figure 5.7: Layer dependence spin Hall conductivity divided by thin film thickness

from -0.06 to -0.04eV. This figure is smallest at the vicinity of the Dirac cone. As the thickness increases up to 21QLs, the SHC across the Dirac cone become flatter as expected, since the contribution from Dirac cone becomes smaller (due to thickness effect) and the number of bulk bands increase.

For the total SHC of thin film without thickness effect, the absolute values of SHC should be shifted by a constant value, having the same trend. Quantitatively, the tendency can be explained as the total SHC of thin film of N QLs with N-2 bulk QLs and 2 surface QLs.

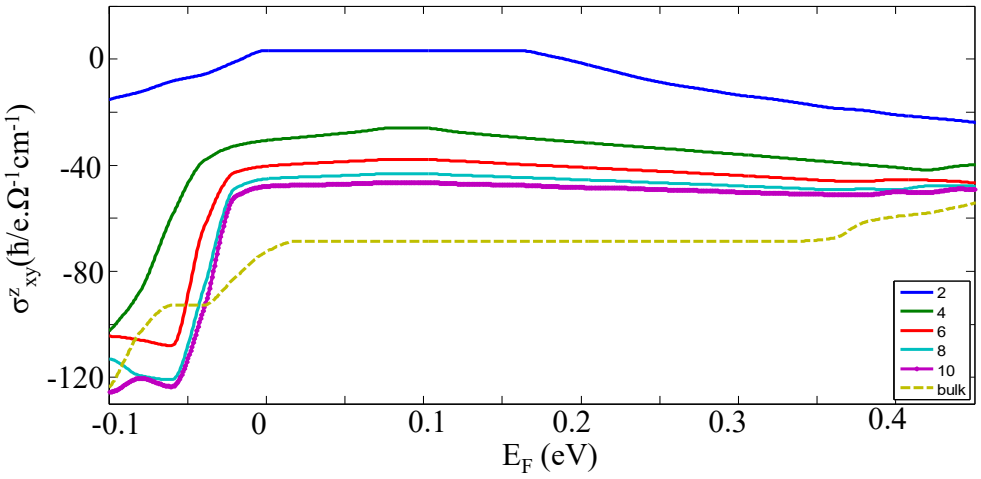

Figure 5.8: Layer dependence and bulk spin Hall conductivity near the Dirac cone.

Figure 5.9 shows a quantitative comparison between the energy dispersion of

10QLs film and the SHC values. It can be seen clearly that the variation of SHC inside the Dirac cone is small compared to the whole Fermi level dependence SHC picture. Since the thickness is finite, discrete quantum well states with surface state can be seen in energy range $E = -0.1 - 0.5$eV. It should be noted that once the thickness is sufficient to see parallel bands which are shifted by a constant value, the SBC of these band are similar to each other just like the case of first conduction quantum well states in Figure 5.9(a). As a result, there is no special change in the trend of SHC at E_F=0.35–0.5eV.

With a band crossing at low or high energy, the SHC of thin film becomes more complex and depends on the property of the band dispersion. At low energy, when the Dirac cone meet the discrete bulk bands, the change in SHC is more complex. Focusing in the energy region of conduction bands with a more complicated dispersion of crossing between surface and bulk states. At the crossing point, the SBC of the single Dirac state is surprisingly large compared to all bulk bands. A sharp jump is presented at E_F=-0.05eV when the SHC changes approximately 3 times.

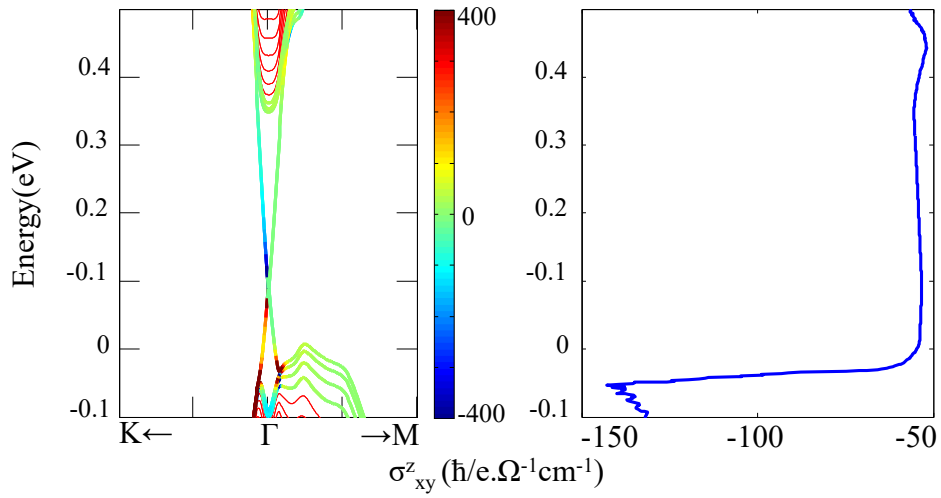

Figure 5.9: (a) Energy dispersion of 10QLs thin film with associated SBC (color map) (b) Averaged spin Hall conductivity.

To look for detailed understanding and check the consistency of calculation, Figure 5.10 shows a momentum dependence SBC for two surface bands for 3QLs cases. Interestingly, the hexagonal wrapping effect which apparently occurs in

TI surface state still survives in the SBC. This can be explained by the energy difference between upper and lower Dirac cones which evolved in the calculations. At the vicinity of Γ point, the Dirac states and bulk states are separated (the bulk band gap of Bi_2Se_3 is around 300meV) and the SBC of the Dirac cones are solely decided by particle-hole scattering within Dirac cone. Whereas the high energy SBC is more sensitive to the neighbouring bands (quantum well states). The signs of SBC for lower and upper DC is positive and negative, respectively in addition to a anisotropic feature (the SBC is stronger along k_x direction). For 3QLs case (figs. 5.10,5.11) an asymmetric feature of SBC intensity is not as clear as for 4QLs case (Figure 5.12).

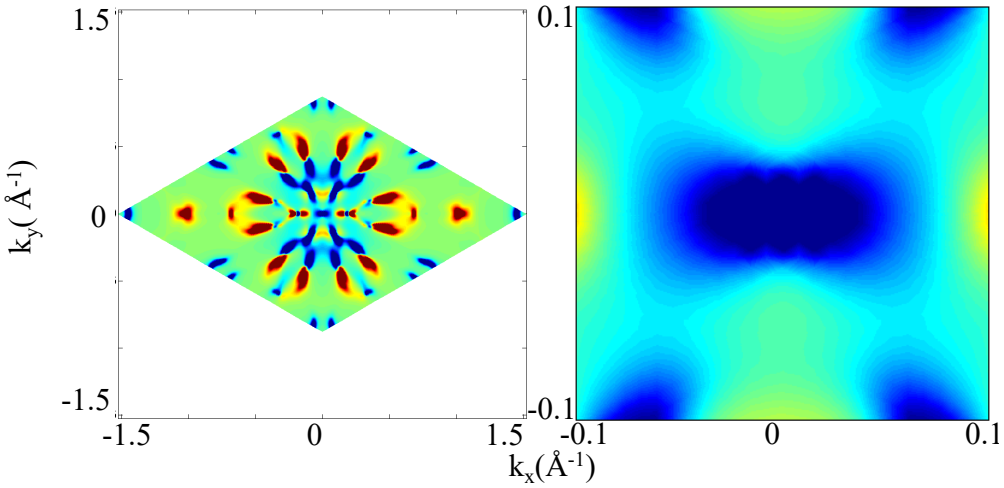

Figure 5.10: Ω^z_{xy} of the upper Dirac cone for 3QL

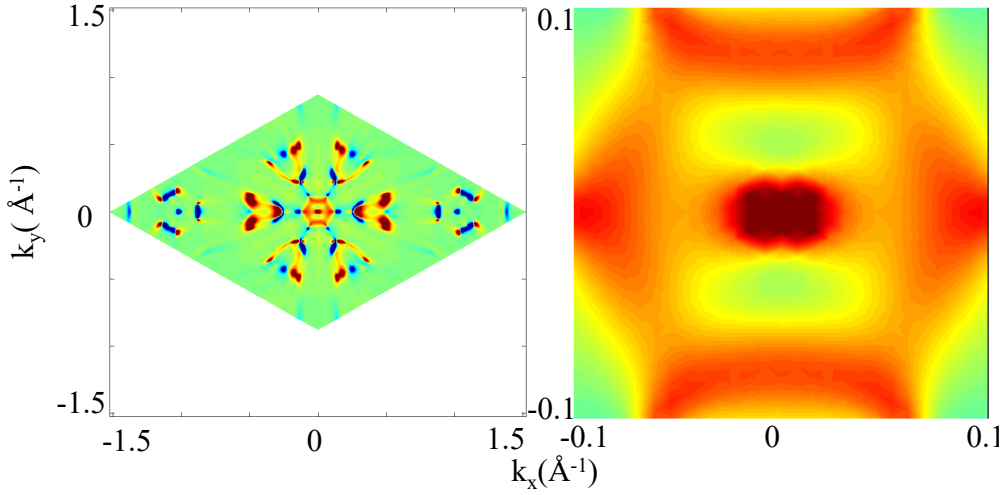

Figure 5.11: Ω^z_{xy} of the lower Dirac cone for 3QL

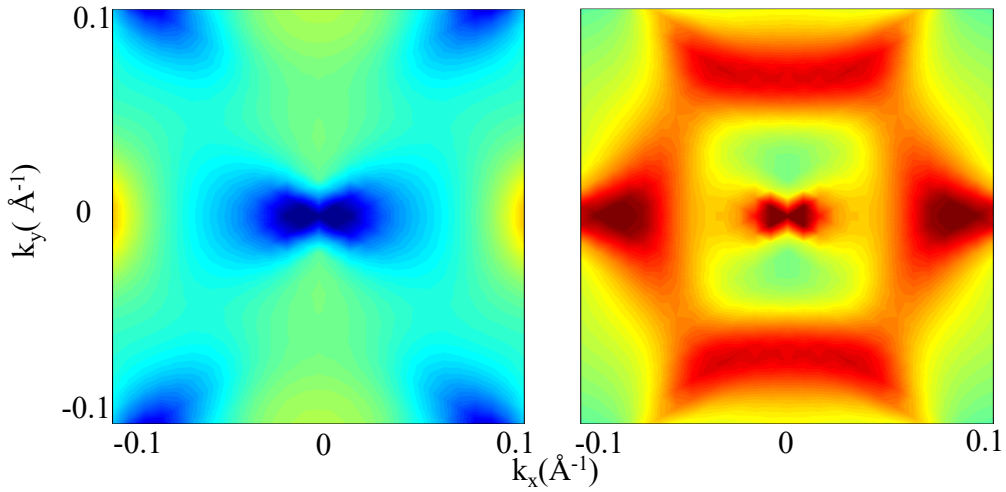

Figure 5.12: Ω^z_{xy} of the upper and lower Dirac cone for 4QL

5.5.1 Spin Hall conductivity from k·p Hamiltonian

We use the k·p model studied in chapter 1 to study the spin Hall conductivity of the Topological Surface State (TSS), comparing with our full tight-binding model. The spin current operator is also defined.

$$\sigma_z = \begin{pmatrix} 1 & 0 & 0 & 0 \\ 0 & 1 & 0 & 0 \\ 0 & 0 & -1 & 0 \\ 0 & 0 & 0 & -1 \end{pmatrix}; j^z_x = \begin{pmatrix} \frac{4k_x}{m_1} & \frac{4k_x}{m_2} & 0 & 0 \\ \frac{4k_x}{m_2} & \frac{4k_x}{m_1} & 0 & 0 \\ 0 & 0 & -\frac{4k_x}{m_1} & -\frac{4k_x}{m_2} \\ 0 & 0 & -\frac{4k_x}{m_2} & -\frac{4k_x}{m_1} \end{pmatrix}$$

The spin operator shows that the spin-up and spin down currents are separated in two opposite direction as well defined from intrinsic spin Hall effect. We define: $k_\pm = k_x \pm ik_y$ The energy dispersion of the Hamiltonian: $E_{1,2} = \frac{k^2 m_2 - m_1\sqrt{k^4 + m_2^2 v^2 k^2}}{m_1 m_2}$, For conduction bands with the corresponding wave functions

$$\Phi_1 = \left\{ -\frac{ik_-}{m_2 v}, \frac{ik_-\sqrt{k^2 + m_2^2 v^2}}{m_2 v k}, 0, 1 \right\}$$
$$\Phi_2 = \left\{ -\frac{ik_-\sqrt{k^2 + m_2^2 v^2}}{m_2 v k}, \frac{ik_-}{m_2 v}, 1, 0 \right\}$$
$$E_{3,4} = \frac{k^2 m_2 + m_1\sqrt{k^4 + m_2^2 v^2 k^2}}{m_1 m_2}$$

For valence bands

$$\Phi_3 = \left\{ -\frac{ik_-}{m_2 v}, -\frac{ik_-\sqrt{k^2+m_2^2v^2}}{m_2 vk}, 0, 1 \right\}; \Phi_4 = \left\{ -\frac{ik_-\sqrt{k^2+m_2^2v^2}}{m_2 vk}, \frac{ik_-}{m_2 v}, 1, 0 \right\}$$

We will show that σ_{xy}^z is positive and the momentum dependence SBC scales as k_x^2 where k_x is direction of the spin current.

$$\Omega_{1,3}^s = Im[< 3|j_x^z|1 >< 1|v_y|3 >]/(E_3 - E_1)^2 \tag{5.6}$$

We have $< 3|j_x^z|1 >= -\frac{8k_x}{m_1}$ a real number. Hence, we have to consider only imaginary part of

$$Im[< 1|v_y|3 >] = \frac{2.k_x}{m_2 k}\sqrt{k^2+m_2^2v^2} \tag{5.7}$$

$$\Omega_{1,3}^s = \frac{-4k_x^2}{k^2}.\frac{m_2}{m_1}.\frac{1}{\sqrt{k^2+m_2^2v^2}} \tag{5.8}$$

$$|\Phi_1| = \sqrt{2(k^2+m_2^2v^2)}/m_2 v, |\Phi_3| = \sqrt{2(k^2+m_2^2v^2)}/m_2 v, \tag{5.9}$$

The spin Berry curvature for valence band is always positive since $m_2 < 0$.

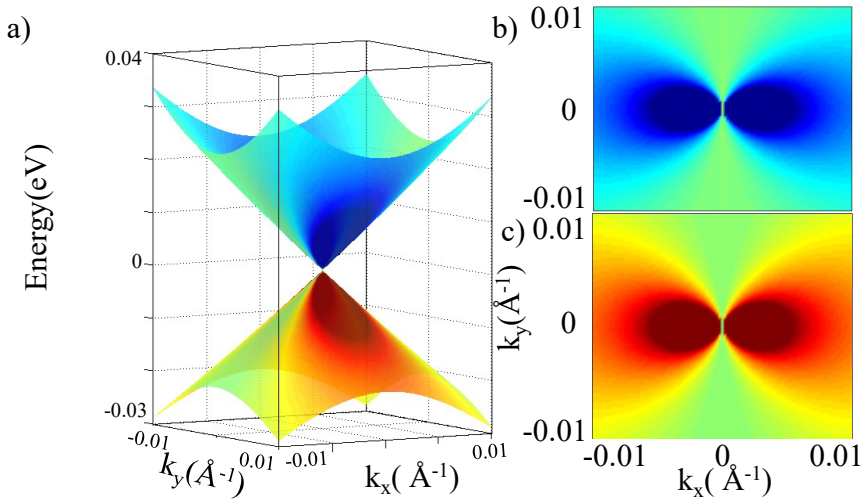

Figure 5.13: Spin Berry curvature from k·p model. (a) 3D view of Ω_{xy}^z, (b) Upper Dirac cone, (c) Lower Dirac cone.

Here, we argue that the SBC carries anisotropic property.

Figure 5.13 clearly shows that an anisotropic feature in the SBC density is due to the quadratic term in the Dirac cone dispersion. If the electric field is applied in k_y direction, the SBC density is concentrated in the k_x direction, giving rise

to the spin Hall current. For a perfectly linear Dirac cone, the two mass terms $m_1, m_2 \to \infty$. The spin current operator is identically zero: $j_x^z = v[\sigma_y, \sigma_z]_+ = 0$. Hence, the momentum dependence SBC of the Dirac cone in figs.5.11–5.12 can be simply explained in the context of our 4 bands k·p Hamiltonian.

5.6 Conclusion

We numerically compute spin Hall conductivity of Z_2 topological insulator. While the spin-orbit coupling in TI material is the driving force of the SHC complemented with the crystalline structure (layered structure), we conclude that the σ_{xy}^z SHC of the bulk Bi_2Se_3 possesses the largest value. Moreover, the concept of spin Hall insulator still works for Bi_2Se_3, since the SHC values is non-zero inside the bulk gap. The SHC for thin film TI possesses interesting features while the interplay between bulk states and surface states become important when the surface states meet bulk. The SHC of surface states can suppress the discrete bulk state for a finite number of layers. Thus, the values of SHC for thin film inside the Dirac state is less negative compared to the bulk. Secondly, with the extensive band-crossing features in the thin film bulk bands, the SHC values can be enhanced to a significant value of. We also found that the angle resolved SBC of Dirac states possesses an antisymmetric feature where the SBC is concentrated in direction perpendicular to the applied electric field. Complemented with numerical results for the surface state SBC, we proved that this feature is due to the quadratic term in the energy dispersion. Moreover, the SHC can also be controlled by the mass terms of the band-structure.

This page was intentionally left blank.

Chapter 6

Conclusion

This thesis provided a comprehensive study of realistic models for magnetically doped thin films in different phases. It is applied to solve long standing problems in the field of quantum anomalous Hall insulators possessing various symmetry properties. All the studies reviewed so far, however, suffer from the fact that the low energy spectra may have more bands than the existing theories possess. In our theory, we consider multiband models constructed from layer-by-layer approach. A key finding of the works is the proposal of a class of QAHI without surface state involved which make the experimental measurements less sensitive to the dielectric substrate. Moreover, the bulk-boundary correspondence is of particular importance for our Hall conductivity results. Particularly, the intrinsic spin Hall effect for thin film TI could be very different from the bulk signals.

Firstly, from a standard multilayer model based on 2DEG we developed the magnetic multiband k·p model, including many experimentally realized perturbations. We confirmed that the stacked quintuple model successfully captures the electronic properties of magnetic TI and trivial thin film compared compared to conventional ARPES measurement. Remarkably, first main theoretical finding is the QAHE without surface state involved, making the system less sensitive to the substrate. Hene, this is an approach to avoid surfaces which are always experimental problem. We have answered a long standing question

of how to get a high Chern number QAHE. Second finding of this thesis is the topological phase transition mechanism driven by magnetic impurities for three experimental realizable magnetic structure mentioned in chaper 2 (FM-TI, FM-TI-FM, magnetically doped TI). The key issue is that the interaction between two surfaces of TI never vanishes unless the slab is semi-infinite. Moreover, the critical phase transition exchange field is found to balance the inter-surfaces tunnelling energy in the TI phase. Meanwhile, this research extends our knowledge of the high Chern number in the Z_2 magnetic thin film of critical phase. The topological phase transition is a result of band exchange and confirmed by the Thouless-Kohmoto-Nightigale-Nijs (TKNN) invariance or the first Chern number. In addition, one key contribution of the study is that the skyrmion spin flip pattern is firstly predicted for FM-TI structure when the inversion symmetry is broken. Even in another magnetic structures, when the inversion symmetry is not broken, the spin up, in plane to spin down transition is of significant results. The previous experimental work has confirmed a hedgehog spin pattern of the valence bands of magnetically doped TI. However, the skyrmion spin-texture should also be a driving force of experimental study.

Regarding Topological Crystalline Insulator (TCI), our prediction of nonlinear touching mechanism and unconventional QAHE is of particular interest to motivate experimental works. The presence of new Van-Hove singularity, broken symmetry order, difference between odd and even number of layers are the driving force for different phases.

Our fundamental conclusion for intrinsic spin Hall effect comes from the presence of surface states in 2D electronic structure models. A full tight binding model can give a prediction for intrinsic spin Hall conductivity. However, the effect of layer thickness is also very important ingredient for experimental measurement.

As an extension of this field, our study suggests that the spin-ARPES measurement can examine higher energy bands to observe the spin-flip pattern in

momentum space. However, in experimental condition the Hall conductivity is no longer quantized in unit of e^2/h due to the effect of temperature fluctuation. Moreover, the non-quantized Hall conductivity with Fermi level being gating modulated. Our proposal simplified the computational complexity of magnetically doped crystal Bi_2Se_3, thus novel broken symmetry topological phases can be tuned on more straightforwardly. In addition, we also showed our prediction on spin Hall conductivity in topological insulator when the number of layers approach infinite. For intrinsic spin Hall effect, the interplay between surface and bulk states becomes an important ingredient to supress the spin Hall conductivity at low energy and enhance that figure at high energy.

We investigated ultrathin TI/trivial/TCI slab with various thicknesses which requires a computational approach, complemented by an analytical result. Hence, the analytical work which was done for a four-band model with magnetic exchange field nicely explains all the calculation results of momentum dependence Berry curvature evolution, spin-flip pattern and critical momentum. A higher order analytical calculation for thin film of higher thickness could be a possible way to explain the transition mechanism of Z_2 TI. However, we could not perform the analytical derivation for larger Hamiltonian. We expect that the topological phase transition point or the momentum resolved spin Berry curvature is almost identical for other layered models with different thicknesses. Moreover, one shortcoming is that the layered k·p model is not able to capture the orbital coupling between d orbitals of transition metal and p orbitals of Se. Another possible improvement of the study could have been adding a term expressing the d orbital coupling through a tight binding model. This method could indicate more exact critical exchange energy for phase transition.

This page was intentionally left blank.

Bibliography

[1] H. Spanier Edwin. *Algebraic Topology*. URL: http://www.springer.com/us/book/9780387944265 (visited on 12/07/2015) (cit. on p. 1).

[2] E. L. Starostin and G. H. M. van der Heijden. "The shape of a Möbius strip". In: *Nature Materials* 6.8 (Aug. 2007), pp. 563–567. DOI: 10.1038/nmat1929 (cit. on p. 1).

[3] Mikio Nakahara. *Geometry, Topology and Physics, Second Edition*. CRC Press, June 4, 2003. 598 pp. (cit. on p. 1).

[4] Isaac Chavel. *Riemannian Geometry: A Modern Introduction*. Cambridge England ; New York: Cambridge University Press, Jan. 27, 1995. 400 pp. (cit. on p. 1).

[5] Bertram Schwarzschild. "Physics Nobel Prize Goes to Tsui, Stormer and Laughlin for the Fractional Quantum Hall Effect". In: *Physics Today* 51.12 (Jan. 11, 2008), pp. 17–19. DOI: 10.1063/1.882480 (cit. on pp. 2, 3).

[6] B. Andrei Bernevig, Taylor L. Hughes, and Shou-Cheng Zhang. "Quantum Spin Hall Effect and Topological Phase Transition in HgTe Quantum Wells". en. In: *Science* 314.5806 (Dec. 2006), pp. 1757–1761. DOI: 10.1126/science.1133734 (cit. on pp. 2, 5).

[7] C. L. Kane and E. J. Mele. "${Z}_{2}$ Topological Order and the Quantum Spin Hall Effect". In: *Physical Review Letters* 95.14 (Sept. 28, 2005), p. 146802. DOI: 10.1103/PhysRevLett.95.146802 (cit. on p. 2).

[8] M. O. Goerbig. *Quantum Hall Effects*. arXiv e-print 0909.1998. Sept. 2009 (cit. on pp. 2, 5, 8).

[9] Shiing-shen Chern. "Characteristic Classes of Hermitian Manifolds". In: *Annals of Mathematics* 47.1 (1946), pp. 85–121. DOI: 10.2307/1969037 (cit. on pp. 2, 3).

[10] R. B. Laughlin. "Quantized Hall conductivity in two dimensions". In: *Physical Review B* 23.10 (May 15, 1981), pp. 5632–5633. DOI: 10.1103/PhysRevB.23.5632 (cit. on p. 3).

[11] Zyun Francis Ezawa. *Quantum Hall Effects: Recent Theoretical and Experimental Developments*. 3rd ed. WORLD SCIENTIFIC, May 2013 (cit. on p. 3).

[12] Yuanbo Zhang et al. "Experimental observation of the quantum Hall effect and Berry's phase in graphene". In: *Nature* 438.7065 (Nov. 10, 2005), pp. 201–204. DOI: 10.1038/nature04235 (cit. on p. 3).

[13] A. H. MacDonald, G. C. Aers, and M. W. C. Dharma-wardana. "Hierarchy of plasmas for fractional quantum Hall states". In: *Physical Review B* 31.8 (Apr. 15, 1985), pp. 5529–5532. DOI: 10.1103/PhysRevB.31.5529 (cit. on p. 3).

[14] Martin Greiter. "Microscopic formulation of the hierarchy of quantized Hall states". In: *Physics Letters B* 336.1 (Sept. 15, 1994), pp. 48–53. DOI: 10.1016/0370-2693(94)00957-0 (cit. on p. 3).

[15] Jairo Sinova et al. "Universal Intrinsic Spin Hall Effect". In: *Physical Review Letters* 92.12 (Mar. 2004), p. 126603. DOI: 10.1103/PhysRevLett.92.126603 (cit. on pp. 3, 87).

[16] M. Z. Hasan. "Topological insulators". In: *Rev. Mod. Phys.* 82 (2010), pp. 3045–3067. DOI: 10.1103/RevModPhys.82.3045 (cit. on pp. 3, 4, 7).

[17] Yoichi Ando. "Topological Insulator Materials". In: *Journal of the Physical Society of Japan* 82.10 (Oct. 2013). arXiv: 1304.5693, p. 102001. DOI: 10.7566/JPSJ.82.102001 (cit. on pp. 4, 31).

[18] Chao-Xing Liu et al. "Quantum Anomalous Hall Effect in Hg_{1-y}Mn_{y}Te Quantum Wells". In: *Physical Review Letters* 101.14 (Oct. 2008), p. 146802. DOI: 10.1103/PhysRevLett.101.146802 (cit. on p. 4).

[19] Huichao Li et al. "Chern number of thin films of the topological insulator Bi_{2}Se_{3}". In: *Physical Review B* 82.16 (Oct. 2010), p. 165104. DOI: 10.1103/PhysRevB.82.165104 (cit. on p. 4).

[20] Markus Koenig et al. *The Quantum Spin Hall Effect: Theory and Experiment*. arXiv e-print 0801.0901. Jan. 2008 (cit. on pp. 4, 5, 8).

[21] Y. L. Chen et al. "Massive Dirac Fermion on the Surface of a Magnetically Doped Topological Insulator". en. In: *Science* 329.5992 (Aug. 2010), pp. 659–662. DOI: 10.1126/science.1189924 (cit. on p. 5).

[22] Hai-Jun Zhang, Xiao Zhang, and Shou-Cheng Zhang. *Quantum Anomalous Hall Effect in Magnetic Topological Insulator GdBiTe3*. arXiv e-print 1108.4857. Aug. 2011 (cit. on p. 5).

[23] Haijun Zhang et al. *Topological States in Ferromagnetic CdO/EuO Quantum Well*. arXiv e-print 1308.0349. Aug. 2013 (cit. on p. 5).

[24] Jing Wang et al. "Quantum Anomalous Hall Effect with Higher Plateaus". In: *Physical Review Letters* 111.13 (Sept. 2013), p. 136801. DOI: 10.1103/PhysRevLett.111.136801 (cit. on pp. 5, 46, 47, 53, 55).

[25] Naoto Nagaosa et al. "Anomalous Hall effect". In: *Reviews of Modern Physics* 82.2 (May 2010), pp. 1539–1592. DOI: 10.1103/RevModPhys.82.1539 (cit. on p. 5).

[26] Cui-Zu Chang. "Experimental Observation of the Quantum Anomalous Hall Effect in a Magnetic Topological Insulator". English. In: *Science* Vol. 340 no. 6129 (Apr. 2013), pp. 167–170. DOI: DOI:10.1126/science.1234414 (cit. on pp. 5, 8).

[27] Hua Jiang et al. "Quantum anomalous Hall effect with tunable Chern number in magnetic topological insulator film". In: *Physical Review B* 85.4 (Jan. 2012), p. 045445. DOI: 10.1103/PhysRevB.85.045445 (cit. on pp. 5, 9, 45–47, 53, 55).

[28] Liang Fu. "Topological Crystalline Insulators". In: *Physical Review Letters* 106.10 (Mar. 2011), p. 106802. DOI: 10.1103/PhysRevLett.106.106802 (cit. on pp. 5, 62, 63).

[29] Timothy H. Hsieh et al. "Topological crystalline insulators in the SnTe material class". en. In: *Nature Communications* 3 (July 2012), p. 982. DOI: 10.1038/ncomms1969 (cit. on pp. 5, 62–64, 66).

[30] Y. Tanaka et al. "Experimental realization of a topological crystalline insulator in SnTe". en. In: *Nature Physics* 8.11 (Nov. 2012), pp. 800–803. DOI: 10.1038/nphys2442 (cit. on pp. 5, 6).

[31] Shiva Safaei et al. "Quantum Spin Hall Effect in IV-VI Topological Crystalline Insulators". In: *arXiv:1501.04728 [cond-mat]* (Jan. 2015). arXiv: 1501.04728 (cit. on p. 6).

[32] Madhab Neupane et al. "Saddle point singularity and topological phase diagram in a tunable topological crystalline insulator (TCI)". In: *arXiv:1403.1560 [cond-mat]* (Mar. 2014) (cit. on pp. 6, 62, 63).

[33] Jeffrey C. Y. Teo, Liang Fu, and C. L. Kane. "Surface States of the Topological Insulator Bi_{1-x}Sb_x". In: *Physical Review B* 78.4 (July 2008). arXiv:0804.2664 [cond-mat]. DOI: 10.1103/PhysRevB.78.045426 (cit. on p. 7).

[34] J. E. Moore. "The birth of topological insulators". In: *Nature* 464 (2010), pp. 194–198. DOI: 10.1038/nature08916 (cit. on p. 7).

[35] Xiao-Liang Qi, Taylor L. Hughes, and Shou-Cheng Zhang. "Topological field theory of time-reversal invariant insulators". In: *Physical Review B* 78.19 (Nov. 2008), p. 195424. DOI: 10.1103/PhysRevB.78.195424 (cit. on p. 7).

[36] Su-Yang Xu et al. "Hedgehog spin texture and Berry/'s phase tuning in a magnetic topological insulator". en. In: *Nature Physics* 8.8 (Aug. 2012), pp. 616–622. DOI: 10.1038/nphys2351 (cit. on p. 8).

[37] H. Li et al. "Carrier density dependence of the magnetic properties in iron-doped Bi2Se3 topological insulator". In: (Feb. 2013). J. Appl. Phys. 113, 043926 (2013) (cit. on p. 8).

[38] Jian-Min Zhang et al. *Tailoring Magnetic Doping in the Topological Insulator Bi2Se3*. arXiv e-print 1205.3936. Phys. Rev. Lett. 109, 266405 (2012). May 2012 (cit. on p. 8).

[39] Yunyou Yang et al. "Time-Reversal-Symmetry-Broken Quantum Spin Hall Effect". In: *Physical Review Letters* 107.6 (Aug. 2, 2011), p. 066602. DOI: 10.1103/PhysRevLett.107.066602 (cit. on p. 8).

[40] Chao-Xing Liu et al. “Model Hamiltonian for Topological Insulators”. In: (May 2010). Phys. Rev. B 82, 045122 (2010) (cit. on p. 9).

[41] D. J. Thouless et al. “Quantized Hall Conductance in a Two-Dimensional Periodic Potential”. In: *Physical Review Letters* 49.6 (Aug. 1982), pp. 405–408. DOI: 10.1103/PhysRevLett.49.405 (cit. on p. 9).

[42] Le Quy Duong et al. “Quantum anomalous Hall effect and a nontrivial spin-texture in ultra-thin films of magnetic topological insulators”. In: *Journal of Applied Physics* 117.17, 17 (2015) (cit. on p. 10).

[43] Gaurav Gupta et al. “Role of acoustic phonons in Bi2Se3 topological insulator slabs: A quantum transport investigation”. In: *Physical Review B* 89.24 (June 2014), p. 245419. DOI: 10.1103/PhysRevB.89.245419 (cit. on pp. 12, 48).

[44] Yi Zhang et al. “Crossover of the three-dimensional topological insulator Bi2Se3 to the two-dimensional limit”. en. In: *Nature Physics* 6.8 (Aug. 2010), pp. 584–588. DOI: 10.1038/nphys1689 (cit. on pp. 21, 35, 50, 56).

[45] S-Y. Xu. “Topological phase transition and texture inversion in a tunable topological insulator”. In: *Science* 332 (2011), pp. 560–564. DOI: 10.1126/science.1201607 (cit. on pp. 45, 46).

[46] Jing Wang et al. “Anomalous Edge Transport in the Quantum Anomalous Hall State”. In: *Phys. Rev. Lett.* 111, 086803 (June 2013). DOI: 10.1103/PhysRevLett.111.086803 (cit. on p. 46).

[47] J. G. Checkelsky et al. “Trajectory of the anomalous Hall effect towards the quantized state in a ferromagnetic topological insulator”. en. In: *Nature Physics* (2014). DOI: 10.1038/nphys3053 (cit. on p. 46).

[48] Le Quy Duong et al. “Quantum anomalous Hall effect with field-tunable Chern number near Z_2 topological critical point”. In: *Phys. Rev. B* 92 (11 2015), p. 115205. DOI: 10.1103/PhysRevB.92.115205 (cit. on p. 46).

[49] Zhenhua Qiao et al. “Microscopic theory of quantum anomalous Hall effect in graphene”. In: *Physical Review B* 85.11 (Mar. 2012), p. 115439. DOI: 10.1103/PhysRevB.85.115439 (cit. on pp. 47, 53, 55).

[50] Pallab Goswami and Sudip Chakravarty. "Quantum Criticality between Topological and Band Insulators in 3+1 Dimensions". In: *Physical Review Letters* 107.19 (Nov. 2011), p. 196803. DOI: 10.1103/PhysRevLett.107.196803 (cit. on p. 47).

[51] Su-Yang Xu et al. "Topological Phase Transition and Texture Inversion in a Tunable Topological Insulator". en. In: *Science* 332.6029 (Apr. 2011), pp. 560–564. DOI: 10.1126/science.1201607 (cit. on p. 47).

[52] Su-Yang Xu et al. "Unconventional transformation of spin Dirac phase across a topological quantum phase transition". en. In: *Nature Communications* 6 (Apr. 2015), p. 6870. DOI: 10.1038/ncomms7870 (cit. on p. 48).

[53] Liang Fu and C. L. Kane. "Superconducting Proximity Effect and Majorana Fermions at the Surface of a Topological Insulator". In: *Physical Review Letters* 100.9 (Mar. 2008), p. 096407. DOI: 10.1103/PhysRevLett.100.096407 (cit. on p. 54).

[54] Dung-Hai Lee. "Surface States of Topological Insulators: The Dirac Fermion in Curved Two-Dimensional Spaces". In: *Physical Review Letters* 103.19 (Nov. 2009), p. 196804. DOI: 10.1103/PhysRevLett.103.196804 (cit. on p. 54).

[55] Rui Yu et al. "Quantized Anomalous Hall Effect in Magnetic Topological Insulators". In: (Feb. 2010). SCIENCE 329, 61 (2010) (cit. on p. 55).

[56] Shuichi Murakami, Naoto Nagaosa, and Shou-Cheng Zhang. "Spin-Hall Insulator". In: *Physical Review Letters* 93.15 (Oct. 2004), p. 156804. DOI: 10.1103/PhysRevLett.93.156804 (cit. on pp. 61, 88).

[57] J. S. Melvin and D. C. Hendry. "Self-consistent relativistic energy bands for tin telluride". en. In: *Journal of Physics C: Solid State Physics* 12.15 (Aug. 1979), p. 3003. DOI: 10.1088/0022-3719/12/15/009 (cit. on p. 61).

[58] Duming Zhang et al. "Quasiparticle scattering from topological crystalline insulator SnTe (001) surface states". In: *arXiv:1405.1073 [cond-mat]* (May 2014) (cit. on p. 62).

[59] Yung Jui Wang et al. "Nontrivial spin texture of the coaxial Dirac cones on the surface of topological crystalline insulator SnTe". In: *Physical Review B* 87.23 (June 2013), p. 235317. DOI: 10.1103/PhysRevB.87.235317 (cit. on p. 62).

[60] Y. Tanaka et al. "Experimental realization of a topological crystalline insulator in SnTe". en. In: *Nature Physics* 8.11 (Nov. 2012), pp. 800–803. DOI: 10.1038/nphys2442 (cit. on p. 63).

[61] Junwei Liu et al. "Spin-filtered edge states with an electrically tunable gap in a two-dimensional topological crystalline insulator". en. In: *Nature Materials* 13.2 (Feb. 2014), pp. 178–183. DOI: 10.1038/nmat3828 (cit. on p. 63).

[62] P. Dziawa et al. "Topological crystalline insulator states in Pb1xSnxSe". en. In: *Nature Materials* 11.12 (Dec. 2012), pp. 1023–1027. DOI: 10.1038/nmat3449 (cit. on p. 63).

[63] Chen Fang, Matthew J. Gilbert, and B Andrei Bernevig. "Large-Chern-Number Quantum Anomalous Hall Effect in Thin-Film Topological Crystalline Insulators". In: *Physical Review Letters* 112.4 (Jan. 2014), p. 046801. DOI: 10.1103/PhysRevLett.112.046801 (cit. on pp. 63, 69, 71, 85).

[64] Le Quy Duong et al. "Quantum anomalous Hall effect in (001) thin films of topological crystalline insulators". In: (2016) (cit. on p. 64).

[65] Xiaofeng Qian, Liang Fu, and Ju Li. "Topological crystalline insulator nanomembrane with strain-tunable band gap". en. In: *Nano Research* 8.3 (Oct. 2014), pp. 967–979. DOI: 10.1007/s12274-014-0578-9 (cit. on p. 65).

[66] J. E. Hirsch. "Spin Hall Effect". In: *Physical Review Letters* 83.9 (Aug. 1999), pp. 1834–1837. DOI: 10.1103/PhysRevLett.83.1834 (cit. on p. 87).

[67] Jairo Sinova et al. "Spin Hall effect". In: *arXiv:1411.3249 [cond-mat]* (Nov. 2014). arXiv: 1411.3249 (cit. on p. 88).

[68] G. Y. Guo, Yugui Yao, and Qian Niu. "Ab~initio Calculation of the Intrinsic Spin Hall Effect in Semiconductors". In: *Physical Review Letters* 94.22 (June 2005), p. 226601. DOI: 10.1103/PhysRevLett.94.226601 (cit. on p. 88).

[69] G. Y. Guo et al. "Intrinsic Spin Hall Effect in Platinum: First-Principles Calculations". In: *Physical Review Letters* 100.9 (Mar. 2008), p. 096401. DOI: 10.1103/PhysRevLett.100.096401 (cit. on p. 88).

[70] H. Kontani et al. "Giant Intrinsic Spin and Orbital Hall Effects in Sr2MO4 (M=Ru,Rh,Mo)". In: *Physical Review Letters* 100.9 (Mar. 2008). arXiv: cond-mat/0702447. DOI: 10.1103/PhysRevLett.100.096601 (cit. on p. 88).

[71] T. Tanaka et al. "Study of Intrinsic Spin Hall Effect and Orbital Hall Effect in 4d- and 5d- Transition Metals". In: *Physical Review B* 77.16 (Apr. 2008). arXiv: 0711.1263. DOI: 10.1103/PhysRevB.77.165117 (cit. on p. 88).

[72] Xiao-Liang Qi and Shou-Cheng Zhang. "Topological insulators and superconductors". In: *Reviews of Modern Physics* 83.4 (Oct. 2011), pp. 1057–1110. DOI: 10.1103/RevModPhys.83.1057 (cit. on p. 88).

[73] Markus König et al. "Quantum Spin Hall Insulator State in HgTe Quantum Wells". en. In: *Science* 318.5851 (Nov. 2007), pp. 766–770. DOI: 10.1126/science.1148047 (cit. on p. 88).

[74] Luqiao Liu et al. "Spin-polarized tunneling study of spin-momentum locking in topological insulators". In: *Physical Review B* 91.23 (June 2015), p. 235437. DOI: 10.1103/PhysRevB.91.235437 (cit. on p. 89).

[75] Yi Liu and Roland E. Allen. "Electronic structure of the semimetals Bi and Sb". In: *Physical Review B* 52.3 (July 1995), pp. 1566–1577. DOI: 10.1103/PhysRevB.52.1566 (cit. on p. 91).

[76] *Phys. Rev. 95, 1154 (1954) - Hall Effect in Ferromagnetics*. URL: http://journals.aps.org/pr/abstract/10.1103/PhysRev.95.1154 (visited on 05/25/2016) (cit. on p. 117).

[77] J. M. Luttinger. "Theory of the Hall Effect in Ferromagnetic Substances". In: *Physical Review* 112.3 (Nov. 1, 1958), pp. 739–751. DOI: 10.1103/PhysRev.112.739 (cit. on p. 117).

[78] L. Smrcka and P. Streda. "Transport coefficients in strong magnetic fields". In: *Journal of Physics C: Solid State Physics* 10.12 (1977), p. 2153. DOI: 10.1088/0022-3719/10/12/021 (cit. on pp. 123, 127).

[79] A. Crépieux and P. Bruno. "Theory of the anomalous Hall effect from the Kubo formula and the Dirac equation". In: *Physical Review B* 64.1 (June 13, 2001), p. 014416. DOI: 10.1103/PhysRevB.64.014416 (cit. on p. 123).

[80] Masaru Onoda and Naoto Nagaosa. "Topological Nature of Anomalous Hall Effect in Ferromagnets". In: *Journal of the Physical Society of Japan* 71.1 (Jan. 15, 2002), pp. 19–22. DOI: 10.1143/JPSJ.71.19 (cit. on p. 123).

This page was intentionally left blank.

Appendix A

Karplus and Luttinger's theory

This section shows the theoretical summary for Hall conductivities based on nothing else but linear response theory. The proof of initial paper of Karplus and Luttinger on the anomalous Hall effect in ferromagnetic metal is summarized [76, 77]. Presumably an internal magnetic moment exists in crystal, a traverse Hall conductance arises due to an interplay between crystal field energy, spin orbit coupling and small electric field perturbation. The total Hamiltonian can be written as

$$H_T = H_0 + H_{SO} + H_E, \tag{A.1}$$

$$H_0 = \frac{p^2}{2m} + V(r), \tag{A.2}$$

$$H_{SO} = [\sigma \times \nabla V(r)].p, \tag{A.3}$$

spin orbit coupling potential when an electron spin couples with orbital degree of freedom. When magnetic field is applied, all electrons are spin polarized through exchange forces. In relativistic representation, the spin orbit coupling energy can also be expressed as: $H = \frac{1}{m^2c^2}\frac{[M\times\nabla V(r)]}{M_s}$, with M_s being maximum magnetic moment when an electrons are lined up in the same direction. $H_E = -e.E.r$ is electron potential under the electric field. Only the electron total Hamiltonian can have Bloch wave function type of solution, since the crystal field and spin-orbit coupling Hamiltonians are periodic whereas the electric

potential is not.

$$(H_0 + H_{SO})\phi_{n,k} = E_{n,k}\phi_{n,k}, \tag{A.4}$$

All electron wave functions are normalized:

$$\langle \phi_{n,k}, \phi_{n',k'} \rangle = \int_\Omega \phi_{n,k}(r)\phi_{n'k'}(r)dx^3 = \delta_{n,n'}\delta_{k,k'}, \tag{A.5}$$

where the integration takes place all over the crystal volume Ω. Here, the importance comes to calculating matrix element of the electron potential Hamiltonian H_E in the Bloch wave function representation. Presumably, an electron is experienced the potential E_y applying in the y direction. The velocity operator is connected with position operator through equation of motion:

$$\frac{\partial R_y}{\partial t} = v_y = i[H, R_y] = i[H_0 + H_{SO}, R_y] = 2\frac{p_y}{m} + \frac{1}{m^2c^2}\frac{[M \times \nabla V]_y}{M_s}, \tag{A.6}$$

We have: $H_k\phi_{n,k} = E_{n,k}\phi_{n,k}$, we neglect the k index in the equation $\frac{\partial H}{\partial k_y} + H\frac{\partial \phi_n}{\partial k} = E_n\frac{\partial \phi_n}{\partial k_y}$, we multiply by $\phi_{n'}$ and integrate over the crystal volume

$$\int \phi_{n'}\frac{\partial H}{\partial k}\phi_n d^3x + \int \phi_{n'}H\frac{\partial \phi_n}{\partial k_y}d^3x = E_n\int \phi_{n'}\frac{\partial \phi_n}{\partial k_y}d^3x$$

$$\langle \phi_{n'}|v_y|\phi_n\rangle + \langle \phi_{n'}|H|\frac{\partial \phi_n}{\partial k_y}\rangle = E_n\langle \phi_{n'}|\frac{\partial \phi_n}{\partial k_y}\rangle,$$

$$\langle \phi_{n'}|v_y|\phi_n\rangle = (E_n - E_{n'})\langle \phi_{n'}|\frac{\partial \phi_n}{\partial k_y}\rangle = i\omega_{n,n'}\langle n|R_b|n'\rangle, \tag{A.7}$$

We would like to express the off diagonal matrix element of velocity operator in a more general way for different k, from the Bloch wave function we have $\phi_{n,k} = e^{i.k.r}\omega_{n,k}$:

$$\langle n,k|R_y|n',k'\rangle = \int_\Omega e^{-i.k.r}\omega^*_{n,k}R_y e^{i.k'.r}\omega_{n',k}d^3x = \int_\Omega e^{-i.k.r}\omega^*_{n,k}\frac{1}{i}\frac{\partial e^{i.k'.r}}{\partial k_b}\omega_{n',k'}d^3x,$$

$$= \frac{1}{i}\frac{\partial}{\partial k_y}\int_\Omega \phi^*_{n,k}\phi_{n',k'}d^3x + i\int e^{i.(k-k').r}\omega_{n,k}\frac{\partial\omega_{n',k'}}{\partial k'_y}d^3x =$$
$$= -i\frac{\partial}{\partial k'_y}(\delta_{n,n'}.\delta_{k,k'}) + i\int e^{i.(k'-k).r}.\omega^*_{n,k}\frac{\partial\omega_{n',k'}}{\partial k'_y}d^3x,$$

Since only ω is orthogonal and periodic, the factor is only non-vanished if $k = k'$. Hence

$$\langle n,k|R_y|n',k'\rangle = i\delta_{n,n'}\frac{\partial}{\partial}\delta_{k,k'} + i.J_y^{nn'}(k), \tag{A.8}$$

with $J_y^{n,n'} = \int_\Omega \omega^*_{n,k}(r)\frac{\partial}{\partial k_y}\omega_{n',k}(r)d^3x$,

$$\langle n,k|H_E|n',k'\rangle = -e.E_y\{i\delta_{n,n'}\frac{\partial}{\partial k_y}\delta_{k,k'} + i.\delta_{k,k'}J_y^{n,n'}(k)\}, \tag{A.9}$$

Thus, the second term comes entirely from off diagonal matrix element, and it contributes to total conductivity problem. The electric field potential can be considered as two term, one periodic and one non-periodic. $H_E = H_1 + H_2$, where H_1 is periodic perturbation with matrix element $-i.e.\delta_{k,k'}E_yJ_y^{n,n'}(k)$, and H_2 representation is unique. We thus can get a periodic Hamiltonian: $H_p = H + H_1$, with the eigenfunctions are stationary one electron states. In addition, the electron distribution can by described by density matrices with two terms namely stationary at constant lattice temperature, and lattice vibration term. $\rho = \rho_0(H_p)+\rho_1$, where $\rho_0(H_0) = \{exp[(H_p-E_F)/kT]+1\}^{-1}$, and ρ_1 is combination of deviation from thermal equibrium, H_2 implemented with the collisions with the lattice. The average velocity operator of the Hall effect is thus: $\langle v_x\rangle = Tr\{\rho_0 v_x\}$. Here the velocity operator v_x can be described as $v_x = i[H,R_x] = i[H_p,R_x] - i[H_1,R_x]$,. The first term gives zero, we only need to calculate the second term:

$$\begin{aligned}\langle v_x\rangle = -i.Tr\{\rho_0(H)[H_1,R_x]\} = -iTr\{[R_x,\rho_0(H)]H_1\} = \\ -i\sum_{n,k}\langle n,k|[R_x,\rho_0(H)]|n,k\rangle\langle n,k|H_1|n,k\rangle \\ -i\sum_{n,k}\sum_{n'\neq n}\langle n,k|[R_x,\rho_0(H)]|n',k\rangle\langle n',k|H_1|n,k\rangle,\end{aligned} \tag{A.10}$$

The operator contains both diagonal and off diagonal terms. We will show that if there exists a Bloch wave function of an eigein-energy $e_n(k)$: $\phi_{n,k} = e^{i.k.r}u_{n,k}$, and an operator $f(H)$, the differentiation of f with respect to momentum:

$$\frac{\partial f(e_n(k))}{\partial k_x} = i[f(H), R_x], \tag{A.11}$$

We have if: $H(p,r)\phi_{n,k} = e_n(k)\phi_{n,k}$ then:

$$H(p+k)u_{n,k} = e_n(k)u(n,k), \tag{A.12}$$

We now have to compute the matrix element of right hand side in (1.10)

$$\begin{aligned}
\langle [f(H), R_x]\rangle_{nk} &= \int d^3x u^*_{nk} e^{-i.k.r}[f(H(p,r)).R_x - R_x f(H(p,r))]e^{i.k.r}u_{nk} \\
&= \int d^3x u^*_{nk} e^{-i.k.r}[f(H(p,r)).i.\frac{\partial}{\partial k_x} - i.\frac{\partial}{\partial k_x}f(H(p,r))]e^{i.k.r}u_{nk} \\
&= -i\int d^3x u^*_{nk}\frac{\partial}{\partial k_x}[e^{-i.k.r}f(H(p,r))e^{i.k.r}]u_{nk} \\
&= -i\int d^3x u^*_{nk}\frac{\partial}{\partial k_x}[f(H(p+k,r))]u_{nk} = -i\frac{\partial}{\partial k_x}\int u^*_{nk}u_{nk}d^3x f(H(p+k,r)),
\end{aligned}$$

Implemented with results from (A.12) we proved (A.11). Applying (A.10) for the case $f(H) = H$, $f(e_n) = e_n$, $\frac{\partial e_n(k)}{\partial k_x} = i\langle [H, R_x]\rangle_{nk} = \langle \dot{R}_x\rangle_{nk} = \langle v_x\rangle_{nk}$, Coming back to Eq.A.10, we have to simplify the equation in term of the velocity operators, thus:

$$\begin{aligned}
-i\sum_{n,k}\langle n,k|[R_x, \rho_0(H)]|n,k\rangle\langle n,k|H_1|n,k\rangle = \\
= -i\sum_{n,k}\frac{\partial\rho(e_n(k))}{\partial k_x}\langle v_x\rangle_{nk}.e.E_b.J^{nn}_b(k) = \\
= -ieE_b\sum_{n,k}\rho'.\langle v_x\rangle_{nk}J^{nn}_b(k),
\end{aligned} \tag{A.13}$$

The off diagonal part in (A.10) then becomes (note that the sum takes over even off diagonal part)

$$-i\sum_{n,k}\sum_{n'\neq n}\langle n,k|[R_x,\rho_0(H)]|n',k\rangle\langle n',k|H_1|n,k\rangle$$
$$=i.e.E_b\sum_{n,k}\rho_0'(e_{n,k})\sum_{n'}\{J_x^{nn'}(k)J_y^{n'n}(k)-J_y^{n,n'}(k)J_x^{n'n}(k)\}, \tag{A.14}$$

After inserting the wave-function, the off diagonal part becomes:

$$-i.e.E_b\sum_{n,k}\rho_0'(e_{n,k})[v_y(n,k)J_x(n,k)-v_x(n,k)J_y(n,k)],$$

, implementing with 1.13: we get the anomalous velocity:

$$\langle v_x\rangle=-i.e.E_y\sum_{n,k}\rho_0'(e_{n,k})v_y(n,k)J_x(n,k), \tag{A.15}$$

This velocity operator gives rise to anomalous velocity, and conductivity. Here we have to express the $J_x(n,k)$ operator in term of the wave function and eigenvalues. We adapt first order perturbation theory of electron unperturbed by spin-orbit coupling with modified wave function. The new wave function is thus:

$$w_{n,k}=u_{n,k}+\sum_{n'\neq n}u_{n',k}(r)\langle n',k|H_{SO}|n,k\rangle_0/(e_{n,k}-e_{n',k})$$

$$J_x(n,k)=2\sum_{n'\neq n}I_x^{nn'}\langle n'|H'|n\rangle/\omega_{n,n'},$$

But $I_x^{nn'}=\int_\Omega u_n^*\frac{\partial u_{n'}}{\partial u_n}d^3x=-\langle n|p_x|n'\rangle_0/m\omega_{nn'}$. Thus, the final transverse velocity operator becomes:

$$\langle v_x\rangle=-2.i.e.E_y\sum_{n,k}\rho_0'(e_{n,k})\sum_{n'\neq n}v_x(n,k)\langle n|p_y|n'\rangle\langle n'|H_{SO}|n\rangle/\omega_{nn'}^2, \tag{A.16}$$

Thus Karplus and Luttinger was the first who studied and related the anomalous Hall effect with the spin-orbit coupling.

This page was intentionally left blank.

Appendix B

Kubo Formalism and relation with Berry curvature

This section shows the Kubo formalism based on the theory for the transport coefficients [78–80]. It mostly summaries the proof by Luttinger when a system in equilibrium and slowly tuned by in-plane electric field. Due to the lengthy proof of the initial Kubo formalism, only mean features are covered. That is, the time dependent wave function gradually changed:

$$\phi^e(r,t) = \phi^e(r)e^{st}, \tag{B.1}$$

The total Hamiltonian is also modified by an time dependence exponential term:

$$H_t = H + Fe^{st}, \tag{B.2}$$

with $F = \int \rho(r)\phi^e(r)dr$, ρ being charge density operator. According to Kubo and later Luttinger, the current density then will take the form of two current correlation function.

$$\langle J\gamma(r)\rangle = \int dr' \int_0^\infty dt e^{-st} \int_0^\beta d\lambda \sum_{\gamma'} \langle j_{\gamma'}(r')j_\gamma(r,t+i\hbar\lambda)\rangle_{eq.} E^e_{\gamma'}(r'), \tag{B.3}$$

After Fourier transforming the wave function, confining ourselves to a single component we obtain: $\phi^e(r) = \frac{1}{V}\phi^e_q e^{iq.r}$, and define: $j_q = \int dr e^{-iq.r} j(r)$ Hence, the q dependence current:

$$\langle J_{q,\gamma}\rangle = \frac{1}{V}\sum_{\gamma'}\int_0^\infty dt e^{-st}\int_0^\beta d\lambda \langle j_{-q,\gamma'} j_{q,\gamma}(t+i\hbar\lambda)\rangle_{eq.} E^e_{q,\gamma'},$$

Here $E^e_q = -iq\phi^e_q$. Note that we already assume $\hbar = 1$, getting back Planck constant in the Hamiltonian. If we assumed the applied field takes the wavevector dependence form, that is: $H' = F.e^{it/\hbar(-\hbar\omega+is)}$ The Hall conductivity is thus can be obtained:

$$\sigma_{\gamma\gamma'}(\omega) = \Omega lim_{s\to 0^+}\int_0^\beta d\lambda \int_0^{+\infty} dt e^{it/\hbar(-\hbar\omega+is)}.Tr\langle\rho_0 J_{\gamma'}(0) J_\gamma(t+i\hbar\lambda)\rangle, \quad \text{(B.4)}$$

We write the current operator matrix elements in the independence electron approximation $H = \sum_n \epsilon_n a^\dagger_n a_n$. That is:

$$\langle n|J_\gamma(i+i\lambda\hbar)|m\rangle = e^{i(t+i\lambda\hbar)/\hbar\epsilon_n} e^{-i(t+i\lambda\hbar)/\hbar\epsilon_m}\langle n|I_\gamma|m\rangle = e^{i(t+i\lambda\hbar)/\hbar(\epsilon_n-\epsilon_m)}\langle n|I_\gamma|m\rangle,$$

Where the I_γ is time independence current operator. Thus, the correlation between two current operators:

$$\langle n|J_{\gamma'}(0)J_\gamma(t+i\hbar\lambda)|m\rangle = \sum_p e^{i(t+i\lambda\hbar)/\hbar(\epsilon_p-\epsilon_n)}\langle m|I_{\gamma'}|p\rangle\langle p|I_\gamma|n\rangle$$

$$Tr(\langle n|J_{\gamma'}(0)J_\gamma(t+i\hbar\lambda)|m\rangle) = \sum_p e^{i(t+i\lambda\hbar)/\hbar(\epsilon_p-\epsilon_n)}\langle m|I_{\gamma'}|p\rangle\langle p|I_\gamma|n\rangle,$$

We also rewrite the charge density operator in new space, with $Tr(\rho_0 a^\dagger_n a_m a^\dagger_p a_q) = \delta_{mp}\delta_{mq} f(\epsilon_m).(1-f(\epsilon_n))$, Plug in the equation, we get:

$$\sigma_{\gamma\gamma'}(\omega) = \Omega lim_{s\to 0^+}\sum_{m,n}\int_0^\beta d\lambda e^{-\lambda(\epsilon_n-\epsilon_m)} f(\epsilon_m)$$
$$*(1-f(\epsilon_n))\int_0^{+\infty} dt e^{it/\hbar(-\hbar\omega+is+\epsilon_n-\epsilon_m)}\langle m|I_{\gamma'}|n\rangle\langle n|I_\gamma|m\rangle,$$

We take integration of each part in this Eq:

$$\int_0^\beta d\lambda e^{-\lambda(\epsilon_n-\epsilon_m)} f(\epsilon_m)(1-f(\epsilon_n)) = \frac{1-e^{-\beta(\epsilon_n-\epsilon_m)}}{(\epsilon_n-\epsilon_m)} \frac{1}{1+e^{\beta\epsilon_m}} \frac{e^{\beta\epsilon_n}}{1+e^{\beta\epsilon_n}} = \frac{f(\epsilon_m)-f(\epsilon_n)}{\epsilon_n-\epsilon_m}$$

$$\int_0^{+\infty} e^{it/\hbar(-\hbar\omega+is+\epsilon_n-\epsilon_m)} dt = \frac{lim_{t\to+\infty} e^{it/\hbar(-\hbar\omega+is+\epsilon_n-\epsilon_m)} - 1}{\frac{i}{\hbar}(-\hbar\omega+is+\epsilon_n-\epsilon_m)} = i\hbar/(-\hbar\omega+is+\epsilon_n-\epsilon_m),$$

Here we can obtain a general Kubo formula

$$\sigma_{\gamma\gamma'}(\omega) = i\hbar\Omega lim_{s\to 0^+} \sum_{n,m} (\frac{f(\epsilon_m)-f(\epsilon_n)}{(\epsilon_n-\epsilon_m)(-\hbar\omega+is+\epsilon_n-\epsilon_m)} \langle m|I_{\gamma'}|n\rangle\langle n|I_\gamma|m\rangle), \tag{B.5}$$

That is, the Kubo formula is a very general version with a finite quasi-particle broaderning s and the current density operators. In momentum space, the operators can be expressed in relation with the velocity operator in momentum space. $I_\gamma = -e.v_\gamma = -e\frac{\partial H}{\hbar\partial k_\gamma}$, thus the Kubo formula in zero broadening limit:

$$\sigma_{\gamma\gamma'} = \frac{e^2}{\hbar} \sum_k Im[\sum_{n,m} (\frac{f(\epsilon_m)-f(\epsilon_n)}{(\epsilon_n-\epsilon_m)^2} \langle m|\frac{\partial H}{\partial k_{\gamma'}}|n\rangle\langle n|\frac{\partial H}{\partial k_\gamma}|m\rangle)], \tag{B.6}$$

For a zero temperature regime, the sum should give contribution for only particle hole scattering process, i.e one band is above and one band is below the Fermi level. Hence, we can write each momentum dependence term as:

$$\sigma_k = \frac{1}{i} \frac{\langle\phi_{mk}|\partial H_{k_{\gamma'}}|\phi_{nk}\rangle\langle\phi_{nk}|\partial H_{k_\gamma}|\phi_{mk}\rangle - \langle\phi_{nk}|\partial H_{k_\gamma}|\phi_{mk}\rangle\langle\phi_{mk}|\partial H_{k_{\gamma'}}|\phi_{nk}\rangle}{(\epsilon_n-\epsilon_m)^2},$$

However, as we proved above: $\langle\phi_{mk}|\partial H_{k_\gamma}|\phi_{nk}\rangle = (\epsilon_m-\epsilon_n)\langle\phi_{mk}|\frac{\partial\phi_{nk}}{\partial k_\gamma}\rangle = (\epsilon_n-\epsilon_m)\langle\frac{\partial\phi_{nk}}{\partial k_\gamma}|\phi_{mk}\rangle$, we can simplify the above equation as:

$$\sigma_k = \frac{1}{i}(\langle\frac{\partial\phi_{nk}}{\partial k_\gamma}|\phi_{mk}\rangle\langle\phi_{mk}|\frac{\partial\phi_{nk}}{\partial k_{\gamma'}}\rangle - \langle\frac{\partial\phi_{mk}}{\partial k_{\gamma'}}|\phi_{nk}\rangle\langle\phi_{nk}|\frac{\partial\phi_{mk}}{\partial k_\gamma}\rangle), \tag{B.7}$$

Reminding that $\sum_{\epsilon_n<E_F<\epsilon_m} |\phi_{nk}\rangle\langle\phi_{nk}| + |\phi_{mk}\rangle\langle\phi_{mk}| = 1$,. Using this relation, plug (B.8) into (B.7) we get:

$$\begin{aligned}
\sigma_{\gamma\gamma'} &= \frac{e^2}{i\hbar} \sum_{\epsilon_n<E_F<\epsilon_m} (\langle \frac{\partial\phi_{nk}}{\partial k_\gamma}|\phi_{mk}\rangle\langle\phi_{mk}|\frac{\partial\phi_{nk}}{\partial k_{\gamma'}}\rangle - \langle \frac{\partial\phi_{mk}}{\partial k_{\gamma'}}|\phi_{nk}\rangle\langle\phi_{nk}|\frac{\partial\phi_{mk}}{\partial k_\gamma}\rangle) = \\
&= \frac{e^2}{i\hbar} \sum_{m,n,k} (\langle \frac{\partial\phi_{nk}}{\partial k_\gamma}|\frac{\partial\phi_{mk}}{\partial k_{\gamma'}}\rangle - \langle \frac{\partial\phi_{mk}}{\partial k_{\gamma'}}|\frac{\partial\phi_{nk}}{\partial k_\gamma}\rangle) = \\
&= \frac{e^2}{2\pi i h} \int d^2k \int d^2r (\frac{\partial\phi^*}{\partial k_{\gamma'}}\frac{\partial\phi}{\partial k_\gamma} - \frac{\partial\phi^*}{\partial k_\gamma}\frac{\partial\phi}{\partial k_{\gamma'}}) = \\
&= \frac{e^2}{h}\frac{1}{2\pi i} \int d^2k [\nabla_k \times \hat{A}(k_\gamma, k_{\gamma'})]_z,
\end{aligned}$$

Where $\hat{A}(k_\gamma, k_{\gamma'}) = \int d^2r (\frac{\partial\phi^*}{\partial k_{\gamma'}}\frac{\partial\phi}{\partial k_\gamma} - \frac{\partial\phi^*}{\partial k_\gamma}\frac{\partial\phi}{\partial k_{\gamma'}})$,. This is the phase factor, the integration of which gives rise to a topological invariance which was obtained by many authors. The above described formulation is a fundamental reason for Hall conducvity quantization and the generalization of quantum anomalous Hall effect in magnetic topological insulators.

Appendix C

Smrcka and Středa theory

Furthermore, we also tried to make a quantitative difference between Hall conductivities in low and high impurity regime for TI by reproducing the calculation based on Smrcka and Středa's formalism [78]. It is also shown that the Fermi surface term, and Fermi sea term. The Kubo formalism has been applied to study not only anomalous Hall effect, quantum anomalous Hall effect but also intrinsic spin Hall effect, and orbital Hall effects. Here we give a brief summary of the Hall conductivity in the Green function approach. Different from zero impurity limit, there are two terms contributing to total spin/anomalous/orbital Hall conductivity with a certain modification for Green function.

Depending on the impurity distribution, the impurity dressed Green function can have a new form: $\hat{G}^{-1}_{imp}(k,\omega) = \hat{G}^{-1}_{0}(k,\omega) - \sum_{imp}$. For a simplest case, the impurity is band-independence and take part as a quasi-particle broadening constant. For a single particle, the Green function: $\hat{G}^{R/A}(k,\omega) = \frac{1}{\omega - \epsilon_k \pm i\delta}$. Based on equation of motion for charge density, the original charge/spin Hall conductivity can be divided by two contributions: the Fermi sea term and Fermi surface term.

$\sigma_{\gamma\gamma'} = \sigma^{I}_{\gamma\gamma'} + \sigma^{II}_{\gamma\gamma'}$, where $\sigma^{I}_{\gamma\gamma'} = \frac{1}{2\pi N}\sum_k Tr[I_\gamma \hat{G}^R I_{\gamma'} \hat{G}^A]_{\omega=0}$, is the Fermi sur-

face term. The Fermi sea term can be expressed as:

$$\sigma^{II}_{\gamma\gamma'} = -\frac{1}{4\pi N}\sum_k \int_{-\infty}^{0} d\omega Tr[I_\gamma \frac{\partial \hat{G}^R}{\partial \omega} I_{\gamma'} \hat{G}^R - I_\gamma \hat{G}^R I_{\gamma'} \frac{\partial \hat{G}^R}{\partial \omega} - (R \leftrightarrow A)],$$

Generally, we tested the numerical results for spin Hall conductivity at certain impurity limit. When the impurity induced broadening is small compared to the energy gap between two nearly crossing bands or the gapped Dirac cone, the Fermi surface term is negligible compared to the Fermi sea term. The Fermi sea term, can also expressed in the Kubo formalism with spin/orbital Berry curvature terms. However, similar to the results for transition metals, the spin/orbital Hall conductivity of topological insulators is largely affected by large number of impurity site. When the impurity induced self-energy term is too large, the Fermi surface term can be a main contribution of the total Hall conductivity.